THE APPLICATION OF THE FINITE ELEMENT METHOD TO FRACTURE MECHANICS PROBLEMS

BY

BAHIR B. SABIR, B.Sc., M.Sc.

Thesis submitted to the CNAA, London, in candidature for the degree of Doctor of Philosophy,

January, 1980.

Department of Civil Engineering and Building,
The Polytechnic of Wales,
Treforest,
Mid. Glamorgan,
U.K.

CERTIFICATE OF RESEARCH

This is to certify that, except where specific reference is made, the work described in this thesis is the result of the investigation of the candidate.

B. B. Sahni
.....
Candidate

Ben Ram
.....
Director of studies

DECLARATION

This is to certify that neither this thesis, nor any part of it, has been presented or is being concurrently submitted in candidature for any degree at any other university.

.....
Candidate

ACKNOWLEDGMENTS

The work presented in this thesis was carried out under the supervision of Dr. B.I.G. Barr and Dr. J. Coughlan, to whome I would like to express my gratitude for their encouragement and advice throughout the course of the investigation.

The author wishes to show his appreciation to Mr. J.T. Williams, the head of department of building, S.G.I.H.E., for his understanding attitude.

Thanks are also due to the computing staff of both, the S.G.I.H.E. (Llandaff) and the Polytechnic of Wales, for their co-operation in the running of the programmes.

Thanks are finally due to Miss. A. Sullivan for her assistance in the typing of the thesis.

SUMMARY

A new finite element which adequately represents the character of the strains near the crack-tip is presented. The element is based on displacement functions, derived from assumed simple strain functions, by integrating the strain - displacement equations. The resulting displacement functions contain terms associated with the rigid body modes. The element is 'trapezoidal' in shape with two straight and two circular boundaries. A 'triangular' crack-tip element based on assumed simple displacement functions is also presented. This element has two of its boundaries straight, meeting at the tip of the crack, and the other circular.

When employed in the singular region of the crack-tip, using as few as 312 degrees of freedom, these elements give results for displacements and stresses whose accuracies are within 1.5% and 3% , respectively, of 'exact' solutions. The elements are combined with Constant Strain Triangular elements to analyse practical geometries used in fracture toughness testing. Relatively coarse meshes are sufficient to obtain accurate estimates of stress intensity factors by a direct displacement method not requiring an extrapolation process.

CONTENTS

NOTATIONS

A	cross-section area
a	crack length
$a_1, a_2, a_3, \ldots$	constants
B	thickness of split cube specimens
$b_1, b_2, b_3, \ldots$	constants
d	cube size
E	elasticity modulus
e	load eccentricity
f_1, f_2, f_3	functions of θ
$f_r, f_\theta, f_{r\theta}$	functions of r and θ
G	rigidity modulus
g	non-dimensional co-ordinate
J	line integral defined in reference 36
k_1, k_2, k_3	stress intensity factors in modes 1, 2 and 3 conditions respectively
k_{1c}, k_{2c}	critical values of stress intensity factors k_1 and k_2 respectively
k_{1B}, k_{1T}	components of stress intensity factors in bending and axial loading respectively
L	line contour surrounding crack-tip
P	applied point or uniform load
R	energy release rate
R_1, R_2, R_3	energy release rates in modes 1,2 and 3 respectively

R_S	radius of the singular region measured from the crack-tip
R_T	radius of tip elements II measured from the crack-tip
S	stress concentration factor defined in reference 46
δS	element of an arc length on contour L
r	radial distance measured from the crack-tip
T	traction vector
t	thickness
U	generalised displacement
U_x, U_y	middle surface displacements in the x and y directions respectively
u,v	middle surface radial and circumferential displacements in the polar co-ordinates system.
V	total strain energy
w	normal displacement in the z-direction
W	specimen width or depth/strain energy density
x,y,z	mutually perpendicular axes
Y	non-dimensional parameter
Z	complex function in the Westergaard system
z	complex number
$( )'$	first derivative
$(\bar{})$, $(\bar{\bar{}})$	first and second integrals respectively

Matrix Notation

$\underset{\sim}{a}$	column vector containing the 'a' constants
$\underset{\sim}{B}$	strain matrix
$\underset{\sim}{C}$	transformation matrix
$\underset{\sim}{D}$	rigidity matrix
$\underset{\sim}{F}$	vector containing structure nodal forces
$\underset{\sim}{H}$	matrix product $(= \underset{\sim}{B}^T \underset{\sim}{D} \underset{\sim}{B})$
$\underset{\sim}{K}$	structure stiffness matrix
$\underset{\sim}{K}_e$	element stiffness matrix
$\underset{\sim}{S}_e$	element stress matrix
$\underset{\sim}{U}$	vector containing structure nodal displacements
$\underset{\sim}{U}_e$	vector containing element nodal displacements
$\underset{\sim}{\epsilon}_e$	element strain vector
$\underset{\sim}{\sigma}_e$	element stress vector
$(\underset{\sim}{\ })^{-1}$	inverse of a matrix
$(\underset{\sim}{\ })^T$	transpose of a matrix

Greek Symbols

ϵ_x, ϵ_y	middle surface strains in the directions of x and y respectively
γ_{xy}	middle surface shear strain
σ	applied stress
σ_m	maximum stress at notch root
τ	nominal in-plane shear stress acting on crack-line
τ_m	maximum in-plane shear stress
$\sigma_x, \sigma_y, \sigma_z$	direct stresses in the directions of x, y and z respectively
$\tau_{xy}, \tau_{xz}, \tau_{yz}$	shear stresses in the three mutually perpendicular planes
$\sigma_r, \sigma_\theta, \tau_{r\theta}$	radial, circumferential and shear stresses in the polar co-ordinates system
Φ	airy stress function
ν	poisson's ratio
μ	function of poisson's ratio
δ	general deflection
ρ	radius of curvature of notch root
λ	influence coefficient
α	angle subtended at the tip in crack-tip element II
θ	angular co-ordinate in the polar co-ordinates system measured from the positive x-direction

CHAPTER 1 INTRODUCTION

Linear fracture mechanics has been widely used by practicing engineers for the prediction of strength and life of cracked structures. For given geometry and loading conditions, an estimate of the stress intensity factor is obtained from the basic laws of elasticity. Experimental analyses are then carried out to determine critical values of this factor under the same loading conditions as those used in calculating the theoretical value. Design stress intensity factors are then obtained by employing a factor of safety in order to avoid failure and excessive crack growth. Although this approach generally leads to acceptable results for simple problems, a more accurate determination of stress intensity factors for complex geometries and loading conditions is essential. Exact solutions to the elasticity problems of cracked structures are very difficult, or nearly impossible, to obtain. The need for a general numerical technique such as the finite element method is, therefore, apparent.

The finite element method of analysis was originally proposed by Turner et al[1] for plane stress problems and a triangular plate element was developed. This was the first utilization of the discrete element approach in the in-plane analysis of two-dimensional continua. The method was then applied to the bending of plates by Zienkiewicz and Cheung[2], Melosh[3] and others. In each of these two classes of problems, the plate is divided into a number of small elements. A deflected form or a stress distribution is assumed for the element and a stiffness matrix relating forces applied at the corners of the element to the corresponding displacements is obtained using the principle of minimum potential energy. The elements are then assembled together so that a relationship between

the external forces acting at the nodes of the complete structure and the corresponding displacements is obtained. Compatibility of displacements is thus satisfied resulting in the overall stiffness matrix for the complete structure. The resulting large number of simultaneous algebraic equations are then solved with the aid of a digital computer.

When constructing an element stiffness matrix, the principal challenge is met in the choice of a displacement field that satisfies certain 'completeness' requirements[4] to ensure convergence to the exact solution. Firstly, the chosen displacement function should be such that it does not permit straining of an element to occur when the nodal displacements are caused by rigid body translation. Secondly, although continuity of displacements is automatically satisfied at the nodes, it is also desirable that such continuity is preserved across the interfaces of adjacent elements. These conditions present difficulties in many formulations and may lead to rather sophisticated displacement fields. It is pointed out[4], for example, that when analysing plates in bending, the normal displacement has to be expressed by more than one polynomial expression throughout an element, in order that full compatibility of displacements and slopes is achieved. In certain cases these difficulties may be overcome by introducing higher derivatives of the basic in-plane and out-of-plane displacements as additional degrees of freedom prescribed at the nodes.

The finite element procedure may be regarded as a process of approximating to a minimum of the potential energy of the structure and loads. In seeking this minimum we must ensure continuity of displacements

and rotations at the nodes because inter-element nodal forces do work on these quantities, but imposition of continuity of other higher order (internal) quantities hinders the approach to the energy minimum and is likely to impair the accuracy of the solution. Bogner et al[5], for example, state that nodal continuity of the first derivatives of the in-plane displacements should not be imposed when using their (48 x 48) element stiffness matrix, based on the well-known conforming 16 term polynomial expansion. Furthermore, the inclusion of such additional degrees of freedom will lead to larger element stiffness matrices which may be very difficult to obtain explicitly. Although this poses no special analytical problems, since the integration involved is customarily performed numerically, it will generally lead to exra computer storage requirements and longer solution time. An advantage of elements not containing these higher order degrees of freedom is to avoid the need to consider the corresponding generalised forces when expressing the boundary conditions for the problem.

The difficulties encountered when seeking fully compatible displacement functions led to several attempts in which some of the continuity requirements were ignored, while still observing other necessary criteria[4]. This approach is founded on the assumption that if continuity is imposed at the nodes, then in the limit, as the mesh is refined, continuity across inter-element boundaries is achieved. However, under certain circumstances, these lead to some errors in the convergence limits. In these cases, it is essential to carry out detailed studies on the effect of mesh size on the results and to ensure, whenever possible, that convergence is to the correct solution.

The first significant contribution to the concept of rigid body displacements was made by Cantin and Clough[6]. They pointed out that polynomial forms of displacement functions were not capable of allowing rigid body displacements for their cylindrical element. They removed this limitation by introducing terms containing trigonometrical functions. Later, Ashwell, Sabir and Roberts[7] demonstrated how a satisfactory displacement function, which includes terms representing the rigid body modes, can be derived from simple assumed strain functions by integrating the strain-displacement equations.

The analysis of fracture mechanics problems by the finite element method has been one of the most active branches of numerical methods in structural mechanics. Initial efforts[11,13-16] using conventional elements demonstrated clearly that hundreds, or sometimes thousands, of elements are required to achieve a solution accuracy within 5%. The number of elements required in a specific circumstance is dependent on the complexity of the problem and the procedure employed in the interpretation of the results.

From the very outset, the most appealing approach to finite element fracture mechanics analysis is that which takes explicit account of the singular character of the stresses at the tip of the crack. A large number of such formulations employing rather sophisticated displacement or stress functions have been developed in the last decade. These generally lead to very difficult integration of the stiffness equations and in some cases result in the elements requiring many nodal points with additional degrees

of freedom.

The main aim of the present investigation is to develop new, simple and efficient finite elements which adequately represent the character of the strains near the crack-tip. These would then be combined with existing more conventional elements to analyse and provide numerical solutions for practical geometries used in fracture toughness testing.

CHAPTER 2 ANALYTICAL CONSIDERATIONS

In this chapter the classical equations for the stresses and displacements near the crack-tip are established in terms of the polar co-ordinates system extensively used in the present study. Brief outlines of the Westergaard method of stress analysis leading to these equations, and the boundary collocation method used in deriving stress intensity factors for basic geometries and loading conditions are given.

2.1 Stress and Displacement Fields near the Crack-Tip

If a crack in a structure is a straight through cut perpendicular to the plane of the material, then crack extension can take place in one of three basic forms depending on the nature of the load. Referring to figure 2.1 and as pointed out by Irwin[8], these basic modes of extension are :-

Mode 1

The opening mode which is associated with symmetric extension or bending of cracked surfaces with displacement discontinuity taking place perpendicular to the plane of the crack.

Mode 2

The sliding mode encountered in skew-symmetric plane loading of cracked surfaces. Displacement discontinuity is in the plane and parallel to the direction of the crack.

Mode 3

The tearing mode which is associated with skew-symmetric bending or twisting of cracked plates where displacement discontinuity is parallel to the leading edge of the crack.

The first two modes can be regarded as plane extensional problems of the theory of elasticity, while the third is a case of pure shear or torsion. The superposition of these three modes is sufficient to describe the most general case of crack-tip deformation and stress fields.

The stress free crack surfaces have a dominating influence on the distribution of stresses in the vicinity of the crack-tip. Other remote

boundaries and loads affect only the intensity of the local stress field.

Starting with the equilibrium equations for plane extension and following the Westergaard method of stress analysis of cracks, briefly outlined in the following sections, the stress and displacement fields associated with each mode are obtained. In accordance with the notation shown in figure 2.2 these are :-

Mode 1

$$
\begin{aligned}
\sigma_x &= \frac{k_1}{(2\pi r)^{\frac{1}{2}}} \cos\frac{\theta}{2}\left(1 - \sin\frac{\theta}{2}\sin\frac{3\theta}{2}\right) \\
\sigma_y &= \frac{k_1}{(2\pi r)^{\frac{1}{2}}} \cos\frac{\theta}{2}\left(1 + \sin\frac{\theta}{2}\sin\frac{3\theta}{2}\right) \\
\tau_{xy} &= \frac{k_1}{(2\pi r)^{\frac{1}{2}}} \cos\frac{\theta}{2}\sin\frac{\theta}{2}\cos\frac{3\theta}{2} \\
U_x &= \frac{k_1}{2G}\left(\frac{r}{2\pi}\right)^{\frac{1}{2}} \cos\frac{\theta}{2}\left(\mu - 1 + 2\sin^2\frac{\theta}{2}\right) \\
U_y &= \frac{k_1}{2G}\left(\frac{r}{2\pi}\right)^{\frac{1}{2}} \sin\frac{\theta}{2}\left(\mu + 1 - 2\cos^2\frac{\theta}{2}\right) \\
w &= 0
\end{aligned}
\qquad (2.1)
$$

Mode 2

$$\sigma_x = -\frac{k_2}{(2\pi r)^{\frac{1}{2}}} \sin\frac{\theta}{2}\left(2 + \cos\frac{\theta}{2}\cos\frac{3\theta}{2}\right)$$

$$\sigma_y = \frac{k_2}{(2\pi r)^{\frac{1}{2}}} \sin\frac{\theta}{2}\cos\frac{\theta}{2}\cos\frac{3\theta}{2}$$

$$\tau_{xy} = \frac{k_2}{(2\pi r)^{\frac{1}{2}}} \cos\frac{\theta}{2}\left(1 - \sin\frac{\theta}{2}\sin\frac{3\theta}{2}\right) \qquad (2.2)$$

$$U_x = \frac{k_2}{2G}\left(\frac{r}{2\pi}\right)^{\frac{1}{2}} \sin\frac{\theta}{2}\left(\mu + 1 + \cos^2\frac{\theta}{2}\right)$$

$$U_y = \frac{k_2}{2G}\left(\frac{r}{2\pi}\right)^{\frac{1}{2}} \cos\frac{\theta}{2}\left(1 - \mu + \sin^2\frac{\theta}{2}\right)$$

$$w = 0$$

Mode 3

$$\tau_{xz} = -\frac{k_3}{(2\pi r)^{\frac{1}{2}}} \sin\frac{\theta}{2}$$

$$\tau_{yz} = \frac{k_3}{(2\pi r)^{\frac{1}{2}}} \cos\frac{\theta}{2}$$

$$\sigma_x = \sigma_z = \tau_{xy} = 0 \qquad (2.3)$$

$$w = \frac{k_3}{G}\left(\frac{2r}{\pi}\right)^{\frac{1}{2}} \sin\frac{\theta}{2}$$

$$U_x = U_y = 0$$

In the preceding equations, G is the modulus of rigidity given by

$$G = \frac{E}{2(1+\nu)}$$

The parameters k_1, k_2 and k_3 are stress intensity factors associated with the three forementioned types of displacement and stress fields. It is important to note that the stress intensity factors are independent of the co-ordinates r and θ and that they control the intensity of these fields but not their distributions. Dimentional considerations of equations 2.1, 2.2 and 2.3 will show that the stress intensity factors must contain the magnitude of the loading forces and must also depend on the configuration of the body including the crack size. Such observations may help in obtaining a physical interpretation of the stress intensity factors as parameters which control the stress redistribution in a body, in the vicinity of the crack-tip due to the introduction of a crack.

In equations 2.1 and 2.2, μ is a function of Poisson's ratio ν depending on whether plane strain or plane stress solutions are considered. For plane strain

$$\mu = 3 - 4\nu \qquad (2.4)$$

and for plane stress

$$\mu = \frac{3-\nu}{1+\nu} \qquad (2.5)$$

Equations 2.1, 2.2 and 2.3 are obtained by neglecting higher order terms in r . They can be regarded as good approximations in the region where r is small compared with other planar dimentions of the body such as crack length and exact in the limit as r approaches zero.

Equations 2.1 and 2.2 for plane extension can be rewritten in terms of the polar co-ordinate system shown in figure 2.4 . The polar stress components σ_r , σ_θ and $\tau_{r\theta}$ can be obtained from σ_x , σ_y and τ_{xy} using the following relationships[10] :-

$$\sigma_r = \sigma_x \cos^2\theta + \sigma_y \sin^2\theta + 2\tau_{xy} \sin\theta \cos\theta$$

$$\sigma_\theta = \sigma_x \sin^2\theta + \sigma_y \cos^2\theta - 2\tau_{xy} \sin\theta \cos\theta \qquad (2.6)$$

$$\tau_{r\theta} = (\sigma_y - \sigma_x) \sin\theta \cos\theta + \tau_{xy} (\cos^2\theta - \sin^2\theta)$$

Referring to figure 2.5 , the radial and tangential displacements u and v are related to U_x and U_y by the following :-

$$u = U_x \cos\theta + U_y \sin\theta$$

$$v = U_x \sin\theta - U_y \cos\theta \qquad (2.7)$$

Using the relationships 2.6 and 2.7 , the systems of equations 2.1 and 2.2 for two dimensional problems become :-

Mode 1

$$\sigma_r = \frac{k_1}{(2\pi r)^{\frac{1}{2}}} \cos\frac{\theta}{2} \left(1 + \sin^2\frac{\theta}{2}\right)$$

$$\sigma_\theta = \frac{k_1}{(2\pi r)^{\frac{1}{2}}} \cos^3\frac{\theta}{2} \tag{2.8}$$

$$\tau_{r\theta} = \frac{k_1}{(2\pi r)^{\frac{1}{2}}} \frac{1}{2} \sin\theta \cos\frac{\theta}{2}$$

$$u = \frac{k_1}{2G} \left(\frac{r}{2\pi}\right)^{\frac{1}{2}} \cos\frac{\theta}{2} \left(\mu + 1 - 2\cos^2\frac{\theta}{2}\right)$$

$$v = \frac{k_1}{2G} \left(\frac{r}{2\pi}\right)^{\frac{1}{2}} \sin\frac{\theta}{2} \left(\mu - 1 + 2\sin^2\frac{\theta}{2}\right) \tag{2.9}$$

Mode 2

$$\sigma_r = \frac{k_2}{(2\pi r)^{\frac{1}{2}}} \cos\frac{\theta}{2} \left(1.5\sin\theta - 2\tan\frac{\theta}{2}\right)$$

$$\sigma_\theta = -1.5 \frac{k_2}{(2\pi r)^{\frac{1}{2}}} \cos\frac{\theta}{2} \sin\theta \tag{2.10}$$

$$\tau_{r\theta} = \frac{1}{2} \frac{k_2}{(2\pi r)^{\frac{1}{2}}} \cos\frac{\theta}{2} \left(3\cos\theta - 1\right)$$

$$u = \frac{k_2}{2G} \left(\frac{r}{2\pi}\right)^{\frac{1}{2}} \sin\frac{\theta}{2} \left(-\mu - 1 + 6\cos^2\frac{\theta}{2}\right)$$

$$v = \frac{k_2}{2G} \left(\frac{r}{2\pi}\right)^{\frac{1}{2}} \cos\frac{\theta}{2} \left(\mu - 1 + 6\sin^2\frac{\theta}{2}\right) \tag{2.11}$$

2.2 Elementary Dimentional Considerations

In the engineering application of linear fracture mechanics a knowledge of the crack-tip stress intensity factor as a function of the applied load and geometry of the cracked structure is necessary for the prediction of strength and life of such structures. Consider, for example, an infinite plate containing a central crack of length 2a subjected to a uniform remote tensile stress σ as shown in figure 2.6 . As a two dimensional problem of the theory of elasticity, only two characteristic dimensions are present, namely σ and a . Since the crack is central and the loading is symmetric with respect to the crack plane, it follows that only the mode 1 stress and displacement fields are present. We, therefore, have

$$k_1 = C \sigma a^{\frac{1}{2}} \qquad (2.12)$$

where C is undeterminable by such considerations. In plane strain fracture toughness testing, however, the critical fracture event is characterised by a single-valued stress intensity (toughness) factor k_{1c} . It follows, therefore, as k_1 approaches k_{1c} then

$$\sigma a^{\frac{1}{2}} = \text{constant} \qquad (2.13)$$

Similar considerations may lead to corresponding expressions for mode 2 and mode 3 situations[9] . Although these are relatively interesting examples, complicated configurations of more practical significance will need more powerful analytical approaches.

2.3 Westergaard System of Stress Analysis

The extensional theory of elasticity is based on two main principles. The first is that forces actiny on the body will be in equilibrium and the second ensures that the resulting deformations are such that elastic continuity is preserved throught the body. For two dimensional analysis, ignoring body forces, the equilibrium equations are[10] :-

$$\frac{\partial \sigma_x}{\partial x} + \frac{\partial \tau_{xy}}{\partial y} = 0$$

$$\frac{\partial \tau_{xy}}{\partial x} + \frac{\partial \sigma_y}{\partial y} = 0 \qquad (2.14)$$

The strain-displacement relationships and Hooke's law lead to the compatibility equation

$$\nabla^2 (\sigma_x + \sigma_y) = 0 \qquad (2.15)$$

where

$$\nabla^2 = \frac{\partial^2}{\partial x^2} + \frac{\partial^2}{\partial y^2}$$

For an elasticity solution, expressions must be found for the stresses which satisfy both equilibrium, equations 2.14, and compatibility, equation 2.15, and give the boundary condition for the problem considered. In general an Airy stress function ϕ is

assumed such that

$$\sigma_x = \frac{\partial^2 \bar{\Phi}}{\partial y^2}$$

$$\sigma_y = \frac{\partial^2 \bar{\Phi}}{\partial x^2} \qquad (2.16)$$

$$\tau_{xy} = -\frac{\partial^2 \bar{\Phi}}{\partial x \partial y}$$

It can be seen that equations 2.16 readily satisfy the equilibrium equations. In order to satisfy the compatibility equations we substitute for the stresses in terms of $\bar{\Phi}$ in equations 2.15 to obtain the following condition :-

$$\nabla^4 \bar{\Phi} = \nabla^2 (\nabla^2 \bar{\Phi}) = 0 \qquad (2.17)$$

where

$$\nabla^4 = \frac{\partial^4}{\partial x^4} + \frac{\partial^4}{\partial x^2 \partial y^2} + \frac{\partial^4}{\partial y^4}$$

It follows that if $\bar{\Phi}$ is chosen such that equation 2.17 is satisfied, the stresses can be determined directly using equations 2.16 provided that the boundary conditions for the problem are observed.

For the solution of stresses near a sharp crack, Westergaard assumes a stress function of the form

$$\bar{\Phi} = \mathrm{Re}\, \bar{\bar{Z}} + y \ \mathrm{Im}\, \bar{Z} \qquad (2.18)$$

Where Z is a complex function and $\bar{(\ )}$ and $\bar{\bar{(\ )}}$ indicate the first and second integrals respectively. Making use of the Cauchy-Riemann equations:-

$$\frac{\partial}{\partial x}\ \mathrm{Re}\ \bar{Z} = \frac{\partial}{\partial y}\ \mathrm{Im}\ \bar{Z} = \mathrm{Re}\ Z$$

$$\frac{\partial}{\partial x}\ \mathrm{Im}\ \bar{Z} = -\frac{\partial}{\partial y}\ \mathrm{Re}\ \bar{Z} = \mathrm{Im}\ Z \qquad (2.19)$$

it can be shown that

$$\sigma_x = \frac{\partial^2 \bar{\bar{\phi}}}{\partial y^2} = \mathrm{Re}\ Z - y\ \mathrm{Im}\ Z'$$

$$\sigma_y = \frac{\partial^2 \bar{\bar{\phi}}}{\partial x^2} = \mathrm{Re}\ Z + y\ \mathrm{Im}\ Z' \qquad (2.20)$$

$$\tau_{xy} = -\frac{\partial^2 \bar{\bar{\phi}}}{\partial x \partial y} = -y\ \mathrm{Re}\ Z'$$

Where $(\ )'$ indicates the first derivative with respect to Z .

Having obtained the solution for the stresses, the in-plane displacements are solved for using the stress-strain relationships, i.e. Hooke's law.

2.4 Crack in an Infinite Plate Under Tension

As an example of the application of the Westergaard method of stress analysis, consider an infinite plate subjected to uniform biaxial tension $\sigma_x = \sigma_y = \sigma$ as shown in figure 2.7 . To investigate the stress redistribution due to the introduction of a crack of length 2a at the centre, Westergaard assumes a stress function such that :-

(i) the crack exerts a stress concentration effect so that $\sigma_y > \sigma$ in the vicinity of the crack-tip

(ii) $\sigma_y = \sigma$ as $x \longrightarrow \pm \infty$

(iii) the crack surface will be stress free i.e.

$\sigma_y = 0$ at $y = 0$ for $x \leqslant \pm a$

The Westergaard stress function for this problem takes the general form

$$Z = \frac{\sigma}{(1 - a^2/z^2)^{\frac{1}{2}}} \qquad (2.21)$$

where z is a complex variable defined by

$$z = x + i\,y$$

Using this function, the solution for the stress in the y-direction, as reported by Paris and Sih[9] , takes the form

$$\sigma_y = \frac{\sigma}{(1 - a^2/x^2)^{\frac{1}{2}}} \qquad (2.22)$$

It can be seen that this solution satisfies the three conditions listed above.

If equation 2.22 is written in terms of the distance ahead of the crack-tip, i.e. $r = x - a$, we have

$$\sigma_y = \frac{\sigma(a + r)}{(2ar)^{\frac{1}{2}}} \left(1 - \frac{r}{2a}\right)^{\frac{1}{2}}$$

or

$$\sigma_y = \frac{\sigma(a + r)}{(2ar)^{\frac{1}{2}}} \left(1 - \frac{r}{4a} + \frac{3}{32}\frac{r^2}{a^2} + \ldots\ldots\right) \qquad (2.23)$$

For the stress close to the crack-tip, i.e. for $r \ll a$, we have

$$\sigma_y = \sigma (a/2r)^{\frac{1}{2}} \qquad (2.24)$$

Equation 2.24 is more commonly expressed in terms of the stress intensity factor k_1 defined by

$$k_1 = \sigma (\pi a)^{\frac{1}{2}} \qquad (2.25)$$

so that

$$\sigma_y = \frac{k_1}{(2\pi r)^{\frac{1}{2}}} \qquad (2.26)$$

It is possible to obtain the full expression for the stress in terms of r and θ, i.e. the second of equations 2.1 , by considering the general solution given by equation 2.21 and the complex distance $(z - a)$ ahead of the crack-tip.

This general procedure may be followed to obtain similar expressions for the stresses under mode 2 and mode 3 conditions.

It is emphasised that equations 2.1 , 2.2 and 2.3 are only approximate and the full expressions may be obtained by considering the full expansion in equation 2.23 . However, they are regarded as good approximations in the region of the crack-tip. Kobayashi et al[11] define this local region as that within $r < a/20$, where a is half the length of the crack.

2.5 The Stress Intensity Factor

It has been customary to express the stresses near the crack-tip in terms of the parameter k which contains the magnitude of the loading and the size of the crack. In this way it is possible to observe the $1/r^{\frac{1}{2}}$ dependency whatever the applied stress system. Combinations of applied loads such as tension, shear, point loads, etc., each give rise to their own contributions to the stress components and the resulting stress intensity is obtained by adding the individual contributions.

Consider, for example, the cracked plate shown in figure 2.8 in which the applied loading consists of uniform tension σ and a point load P at $x = 0$, $y = 0$. If σ and P independently give rise to the stress intensity factors k_σ and k_p respectively, then the total stress intensity factor k will be given by

$$k = k_\sigma + k_p \qquad (2.27)$$

and the stress σ_y in the vicinity of the crack-tip by

$$\sigma_y = (k_\sigma + k_p) / (2\pi r)^{\frac{1}{2}} \qquad (2.28)$$

Westergaard give

$$k_p = P / (\pi a)^{\frac{1}{2}}$$

and hence

$$\sigma_y = (\sigma + P) / (\pi a)^{\frac{1}{2}} \qquad (2.29)$$

Expressions for k have been established for a number of loading configurations[9]. For bodies of finite dimensions, the usual practice is to modify the solution for an infinite body under the same loading conditions by an algebraic or trigonometrical function which is chosen to make the appropriate crack surface forces zero. The general methods of modifying stress functions in this way are referred to as 'boundary collocation' methods.

The stress intensity factor for a plate of width W with central crack is given by Irwin[12] as

$$k = \sigma \left[W \tan (\pi a/W) \right]^{\frac{1}{2}} \qquad (2.30)$$

This may be rewritten in expansion form as

$$k = \sigma W^{\frac{1}{2}} \left(\frac{\pi a}{W} + \frac{\pi^3 a^3}{3 W^3} + \ldots\ldots\ldots \right)^{\frac{1}{2}}$$

or

$$k = \sigma (\pi a)^{\frac{1}{2}} \left(1 + \frac{\pi^2 a^2}{6 W^2} + \ldots\ldots \right)$$

For an infinite plate, $a/W \longrightarrow 0$ and hence

$$k = \sigma (\pi a)^{\frac{1}{2}}$$

which is the same as that obtained in equation 2.25.

The analytical approach, briefly outlined in this chapter, generally lead to acceptable results for simple problems. For complex geometries and loading conditions, a general numerical approach is required. Such an approach is the finite element method which was first suggested for fracture mechanics analysis by Chan et al[13].

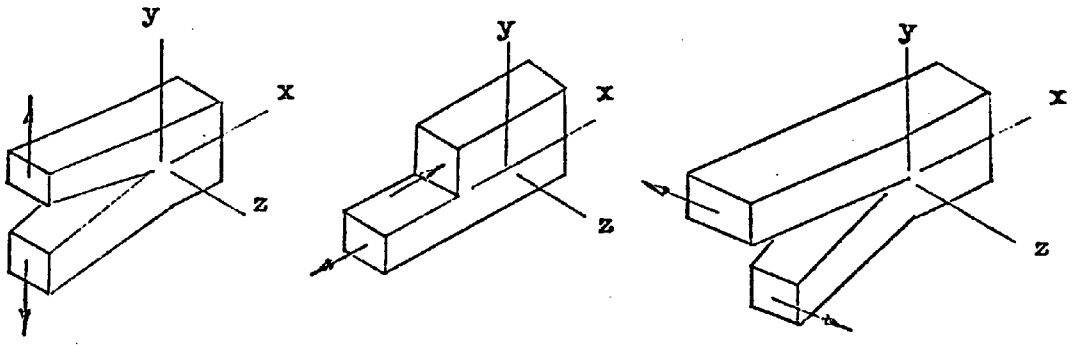

Mode 1 Mode 2 Mode 3

Figure 2.1 Basic modes of crack-surface displacements

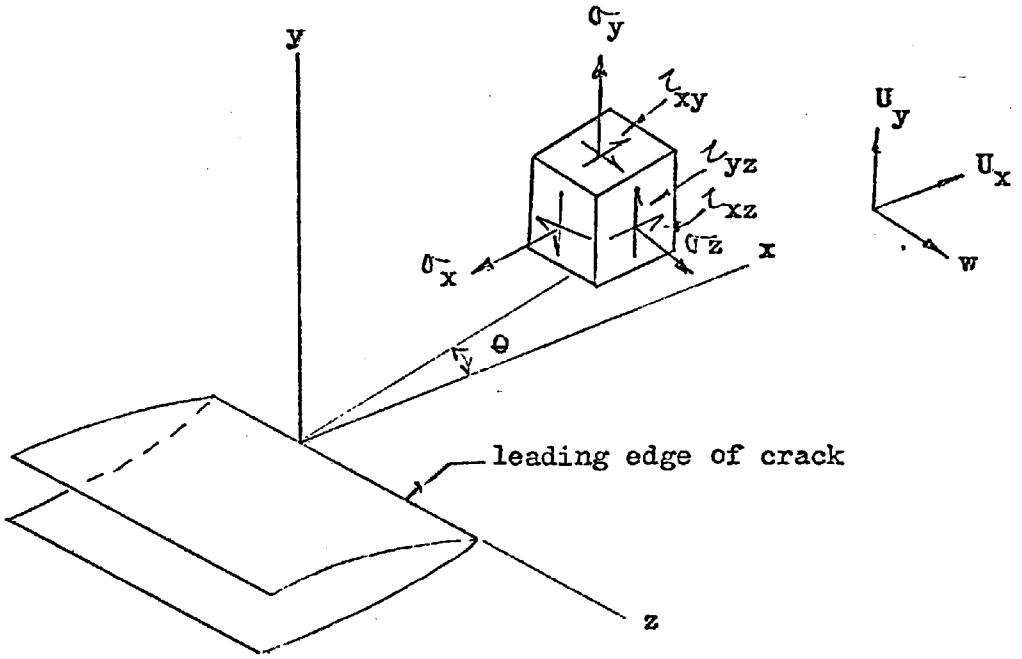

Figure 2.2 Displacements and stress components - co-ordinates measured from leading edge of crack

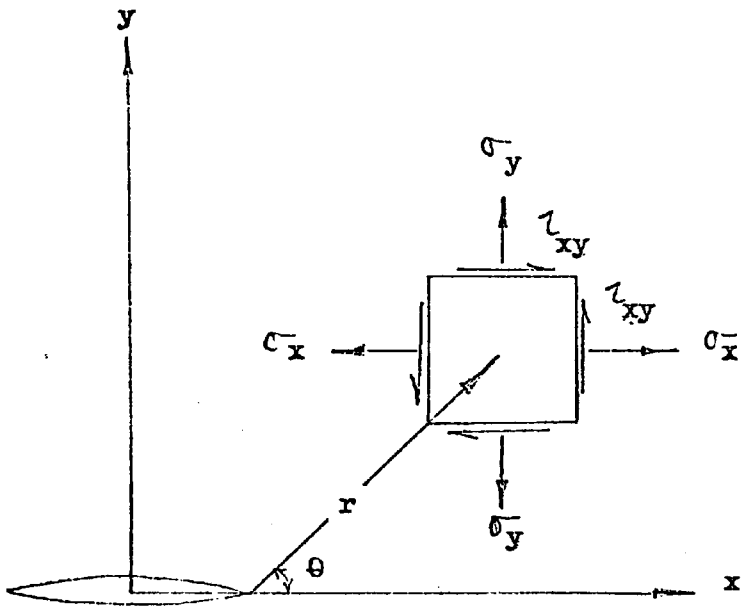

Figure 2.3 Notation for rectangular stress components

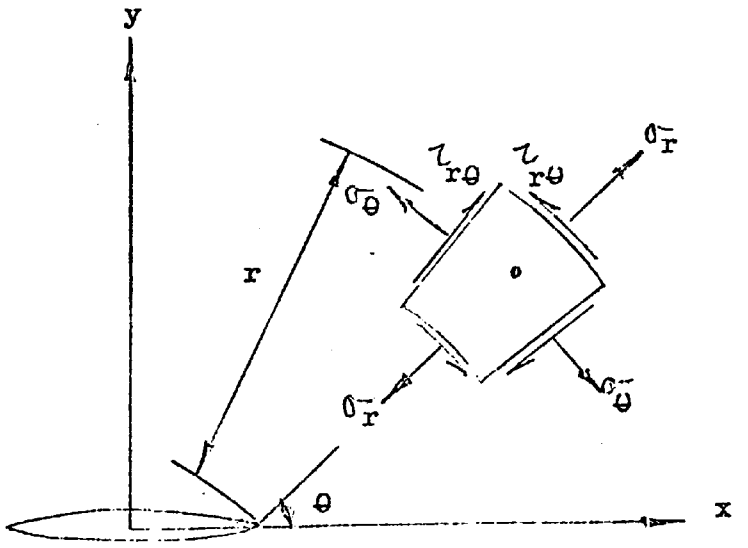

Figure 2.4 Notation for polar stress components

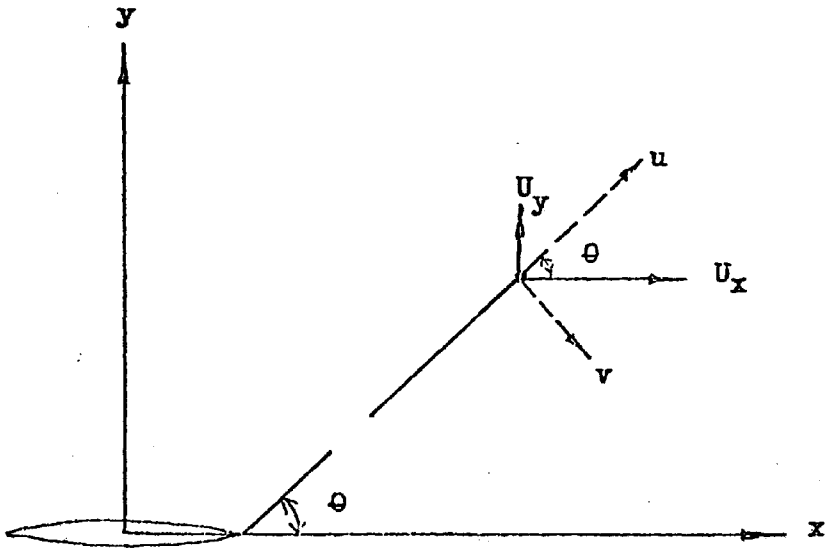

Figure 2.5 Relationship between polar and rectangular displacements

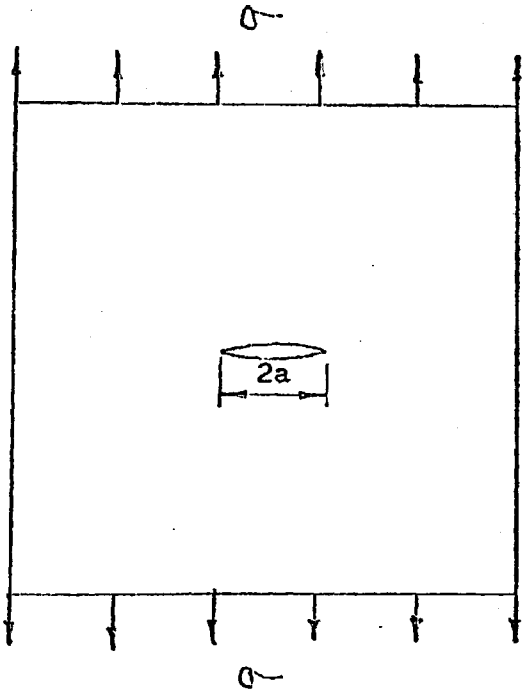

Figure 2.6 An infinite cracked plate subjected to remote uniform stress

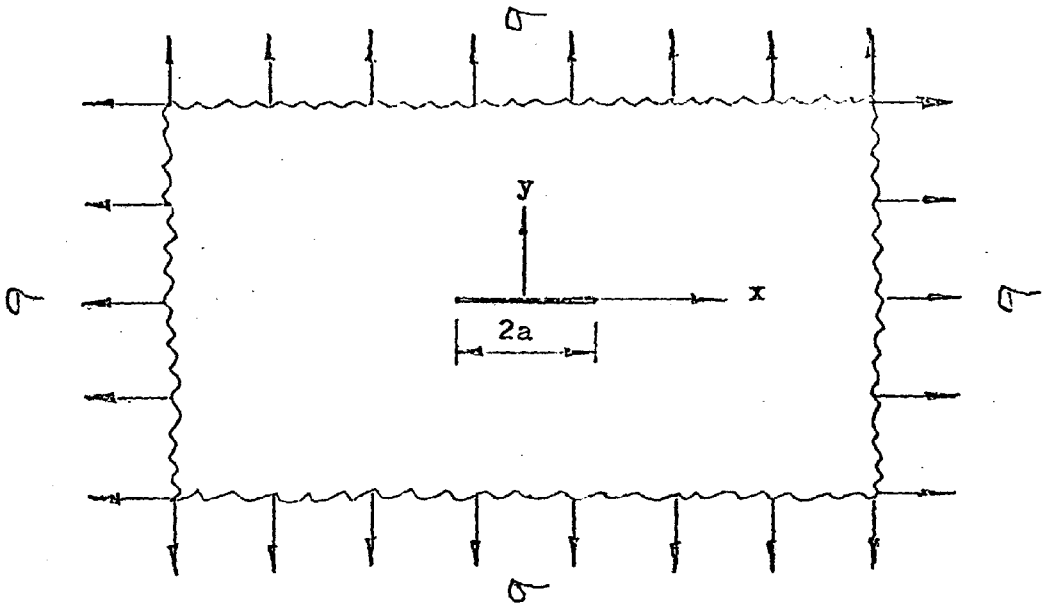

Figure 2.7 An infinite sheet with a central crack under biaxial tension

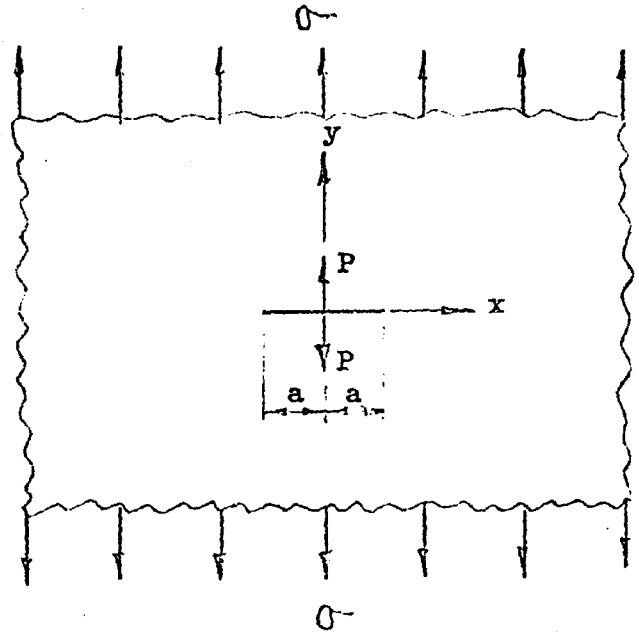

Figure 2.8 An infinite plate under uniform tension and a point load

CHAPTER 3 LINEAR FRACTURE MECHANICS BY FINITE ELEMENTS

Considerable developments have been made in the application of the finite element method to fracture mechanics problems. This chapter gives a critical review of the various approaches used and summarises the methods for calculating stress intensity factors from the finite element results.

3.1 Review of Previous Work

The finite element method has been used in many investigations for the solution of linear fracture mechanics problems. Early papers[11,13-16] in this field used conventional elements to estimate stress intensity factors near the crack-tip. In these works the cracked structure is represented by constant strain triangular finite elements[4]. Although acceptable solutions have been obtained for simple geometries, it was found necessary to use a large number of elements around the crack-tip. For example Chan et al[13] extrapolated the solution away from the crack-tip to estimate k_1 , since the near tip solutions were not reasonable. About 2,000 degrees of freedom were used in analysing an edge-cracked plate under eccentric loads in order to gain accuracy within 5% of a collocation solution they had obtained.

An obvious and attractive approach to finite element fracture mechanics analysis is that based on displacement functions which take account of the singular stresses at the tip of the crack. The expressions for the stresses in the local region of the crack-tip are given in equations 2.1, 2.2 and 2.3 . It is pointed out that these equations are approximate and contain only the first term that predominates at the tip and gives rise to the singularity. The full series forms include terms proportional to $r^{\frac{1}{2}}$, $r^{3/2}$, etc. The additional terms appearing in the corresponding displacement expressions together with the first term can therefore be employed as the assumed displacement functions for the finite element model.

Byskov[17] appears to have been the first to formulate a finite

element based on classical displacement functions using the singular stress fields established by Muskhelishvili[18]. The element is triangular in shape, see figure 3.1, with the crack-tip at the interior of the triangle. In his analysis, all elements surrounding this special element are conventional constant strain triangles. Although continuity of displacements across the element interfaces was not achieved, except at the nodes, it is interesting to note that the special crack element contained terms representing the rigid body modes.

A high order circular crack-tip element, similar in many respects to that of Byskov, was presented by Wilson[19]. The author's general formulation for the crack-tip element is in terms of a stress function, due to Williams[20], which is equivalent to that of Muskhelishvili .

The primary difference between the two approaches of references 17 and 19 are element shape and coupling technique with the surrounding constant strain triangular elements. The circular shape of Wilson's element allowed the stiffness matrix to be expressed explicitly, whereas the stiffness matrix of Byskov's element is determined numerically. To maintain the approximate circular shape of the outer boundary, Wilson found it necessary to surround the tip element by a large number of conventional elements. It was argued, however, that a sufficient number of conventional elements is required in order to reduce the effect of non-compatibility of displacements at the interfaces of the two types of elements. Byskov's element can be surrounded by only three conventional elements and hence no effective control is maintained over the influence of non-compatibility of displacements.

Polynomial type shape functions, rather than classical solution functions, have also been used to produce element stiffness matrices which contain singularities. These usually lead to simpler forms of elements and easier integration of the stiffness equations. Tracey[21] introduced an element for an elastic medium which embodies the singularity conditions at the crack-tip. The displacement field, in either direction, in terms of element 'natural' co-ordinates $(\bar{x},\bar{y})$ take the general form :-

$$U = a_1 + a_2\sqrt{\bar{x}} + a_3\sqrt{\bar{x}}\,\bar{y} + a_4\bar{y} \qquad (3.1)$$

The 'natural' element is transformed into the physical x-y plane in the form of a quadrilateral or a triangle as shown in figure 3.2 using special mapping functions. In order to obtain a triangular element with one vertix at the crack-tip, two distinct nodes on the 'natural' element are mapped onto one node of the physical triangle by imposing special conditions at these nodes. The near tip elements based on equation 3.1 were surrounded by trapezoidal isoparametric elements[4] with displacement functions :-

$$U = a_1 + a_2\bar{x} + a_3\bar{y} + a_4\bar{x}\bar{y} \qquad (3.2)$$

The author[21] points out that the isoparametric elements have a singular stress variation admissible within the element as well as a

constant stress state, thus reducing the effects of displacement non-compatibility. In analysing a rectangular bar with symmetrical edge cracks, it was found that stress intensity factors within 4% of an accepted value were obtained using 548 degrees of freedom.

A stiffness matrix for the triangular crack-tip element shown in figure 3.3 was presented by Wilson[19]. The crack-tip region is enclosed by a series of these wedge-shaped isosceles triangular elements, all having a common nodal point at the tip. The displacement patterns for this element may be simplified and written in a general form as :-

$$U_x = (a_1 + a_2\,\theta)\; r^{\frac{1}{2}}$$

$$U_y = (a_3 + a_4\,\theta)\; r^{\frac{1}{2}} \qquad (3.3)$$

Where U_x and U_y are the in-plane displacements of any point near the crack-tip in the directions of x and y respectively. The four discrete parameters a_1 , a_2 , a_3 and a_4 , which characterise the element, are associated with the two degrees of freedom (U_x and U_y) at the two nodes of the element away from the tip. It is clear that the element resulting from these assumed displacement functions will contain the singularity associated with the crack-tip region.

In the examples considered by Wilson, the singular strain triangular elements were surrounded by conventional constant strain triangular elements[4]. It is pointed out that displacements in these elements vary

linearly with the x-y co-ordinates, whereas displacements on the outer boundary of the singular element vary approximately linearly with the angular polar co-ordinate θ . Although displacements are continuous only at the two common nodal points of the two types of elements, the author[19] suggests that as the wedge angles of the tip elements decrease indefinitely, continuity at the common interface will be approached in the limit.

One of the examples considered by Wilson was that of the circular body shown in figure 3.4 containing a radial crack projecting from its centre to its outer edge. The outer boundary of the body was subjected to the forces obtained from the classical singular stress corresponding to the mode 1 conditions. The body was represented by singular elements of radii equal to one half of the radius of the body surrounded by constant strain elements. It was shown that when 18 singular elements are used, the displacements at the outer boundary of the tip elements had a maximum error of about 3% . However, when the whole body was represented by conventional constant strain elements, these errors were shown to be 20 - 30% .

It was pointed out[19] that the imposed displacement functions for the triangular tip element used by Tracey[21] may take the general form :-

$$U = \left[b_1 (\cos \theta)^{\frac{1}{2}} + b_2 (\cos \theta)^{\frac{1}{2}} \tan \theta \right] r^{\frac{1}{2}} \qquad (3.4)$$

As the included angle at the crack-tip nodal point decreases, the

displacement pattern approaches

$$U = (b_1 + b_2\theta)r^{\frac{1}{2}} \qquad (3.5)$$

which is the same pattern as that assumed by Wilson. Wilson reported that when 24 elements are used at the crack-tip, displacement patterns for the two elements differed by about 0.1% . Furthermore, Wilson's simple element can be expressed in a closed form whereas that of Tracey is determined by numerical integration.

It has been shown that singular transformations from physical to isoparametric co-ordinates can be made if node points along the sides of the element are positioned in a certain way. Henshell and Shaw[22] used the standard 8-noded isoparametric element with mid-side nodes displaced to the quarter points to produce singularity at the tip of the crack as shown in figure 3.5 . Barsoum[23] pointed out that while producing singularity, as other special crack-tip elements, the modified isoparametric element retained the advantage of producing constant strain and rigid body motion modes. The author[23] reports a solution for the same problem analysed by Tracey[21] with similar accuracy using 700 degrees of freedom. In a subsequent paper[24] , Barsoum extended the approach to obtain an element for fracture analysis of shells based on a 20-noded solid isoparametric element. Isoparametric elements have also been used successfully in non-linear analysis of fracture problems[25-28].

Hibbitt[29] pointed out that a variety of strain singularities can be produced using isoparametric elements based on higher order polynomial

functions. In a recent review, Gallagher[30] demonstrates this by defining both the displacement function u and the physical co-ordinate x in terms of a non-dimensional co-ordinate g as follows :-

$$x = a_0 + a_1 g + a_2 g^2 + \ldots\ldots\ldots + a_n g^n \qquad (3.6)$$

$$u = b_0 + b_1 g + b_2 g^2 + \ldots\ldots\ldots + b_n g^n \qquad (3.7)$$

The node points in the distance $g = 0$ to $g = 1$ can be so arranged that all the (a) constants except a_0 and a_n are made zero. In this way equation 3.6 becomes

$$x = a_0 + a_n g^n \qquad (3.8)$$

If the origin is so chosen that $a_0 = 0$, we have

$$g = \left(\frac{x}{a_n} \right)^{1/n} \qquad (3.9)$$

The strain is given by

$$\epsilon_x = \frac{du}{dx} = \frac{du}{dg} \cdot \frac{dg}{dx} \qquad (3.10)$$

Differentiating equations 3.7 and 3.8 we have

$$\frac{du}{dg} = b_1 + 2\,b_2\,g + 3\,b_3\,g^2 + \ldots\ldots + n\,b_n\,g^{n-1}$$

$$\frac{dx}{dg} = n\,a_n\,g^{n-1} \qquad (3.11)$$

The strain , equation 3.10, then becomes :-

$$\epsilon_x = \frac{1}{n\,a_n}\,(b_1\,g^{1-n} + 2\,b_2\,g^{2-n} + 3\,b_3\,g^{3-n} + \ldots. + n\,b_n) \qquad (3.12)$$

Substituting for g from equation 3.9 , we have

$$\epsilon_x = \frac{1}{n\,a_n}\left[b_1\left(\frac{x}{a_n}\right)^{\frac{1-n}{n}} + 2\,b_2\left(\frac{x}{a_n}\right)^{\frac{2-n}{n}} + \ldots. + n\,b_n\right] \qquad (3.13)$$

The leading term in this expression is of the order $x^{\frac{1-n}{n}}$ and this gives a singularity of order $x^{-\frac{1}{2}}$ for n = 2 , $x^{-2/3}$ for n = 3 , etc. The range of singularity as n varies from 2 to ∞ being $x^{-\frac{1}{2}}$ to x^{-1} .

Barsoum[27] pointed out that when using isoparametric elements as shown in figure 3.5, the singularity condition prevails only along the edges of the elements. The author[27] overcomes this by collapsing a pair of nodes to form a triangular element as shown in figure 3.6 in which singularity prevails on all lines eminating from the vertix at the tip of the crack.

The use of the singularity isoparametric elements is clearly confined to the elements enclosing the tip of the crack, the elements surrounding them being of the conventional type. In reference 31 it was shown that if a layer of 'transitional' elements surround the tip elements, a significant improvement in the accuracy of the solution is obtained without increasing the number of degrees of freedom. In these elements the side nodes are positioned between the quarter and mid-side points.

Another approach in producing finite elements for fracture analysis is that based on mixed 'hybrid' formulation. This method involves prescribing two or more stress or displacement fields within the element, employing available singular stress fields from classical fracture mechanics analysis together with simple polynomial expansions. An advantage of this approach[32] is that the assumed functions contain the stress intensity factors which are regarded as the unknowns and hence solved for directly.

The above review shows that considerable developments have been made in the application of the finite element method to fracture mechanics analysis. Although there is still new work employing conventional elements[33,34], most of the recent efforts have been aimed at incorporating the singular stress fields directly into the finite element formulation. This is usually done for a single element embedding the crack-tip[19], a cluster of elements enclosing the crack-tip[19-21] or a cluster around the the tip supplemented by another ring of elements[21,31]. The resulting special elements are capable of

representing the stresses at the crack-tip with considerable accuracy, while conventional elements are used to represent the remaining part of the structure. However to achieve over-all accuracy further conditions should hold. There must be adequate displacement compatibility between the special tip elements and the surrounding conventional elements. Furthermore, these surrounding elements must be small enough to give a close representation of the stresses adjacent to the special elements. This situation can lead to some difficulty in the choice of the size of the tip elements. They should be large enough to cover the region of large stress gradients, yet small enough to interface with a sufficiently fine exterior mesh.

3.2 Calculation of Stress Intensity Factors from the Finite Element Results

Once the numerical solution has been obtained for a particular finite element representation, crack-tip stress intensity factors can be estimated using one of two basic approaches. In the first approach, stress intensity factors are obtained by direct substitution of the results for displacements or stresses in the well-known crack-tip equations. These methods will be referred to as the direct methods.

The equilibrium and stability of cracks from an energy viewpoint was first discussed by Griffith[35] . Later Irwin[12] presented a more detailed study of the energy analysis and its relationship to the crack-tip stress field approach. Since then a number of somewhat different energy analyses for the calculation of stress intensity factors have been developed by many authors[9,13-15,36] . These form the basis of the second approach and will be referred to as the energy methods.

3.2.1 The Direct Methods

The results of the finite element analysis are compared with the exact theoretical values obtained from the established relationships 2.1, 2.2 and 2.3 at the crack-tip. This may be based on the displacements or the stresses.

3.2.1.1 The Displacement Method

This method involves a correlation of the finite element nodal point displacements near the crack-tip with the well-known tip displacement equations. For mode 1 conditions and in terms of polar co-ordinates, these may be written as follows :-

$$u_i = \frac{k_1}{2G} \left(\frac{r}{2\pi} \right)^{\frac{1}{2}} f_i(r,\theta) \qquad (3.14)$$

Where,

$$u_1 = u \ , \quad u_2 = v$$

and

$$f_1(\mu,\theta) = \cos\frac{\theta}{2}\left(\mu + 1 - 2\cos^2\frac{\theta}{2}\right)$$

$$f_2(\mu,\theta) = \sin\frac{\theta}{2}\left(\mu - 1 + 2\sin^2\frac{\theta}{2}\right)$$

An appropriate choice of the value of μ will decide whether plane stress or plane strain conditions are considered. By substituting a

finite element nodal point displacement u_i^* at some point (r,θ) near the crack-tip into equations 2.9 , a value of the stress intensity factor k_1^* can be obtained from :-

$$k_1^* = 2G \left(\frac{2\pi}{r}\right)^{\frac{1}{2}} u_i^* / f_i(\mu,\theta) \qquad (3.15)$$

A number of such values can be calculated for different values of r and a fixed value of θ from a particular displacement component. A plot of k_1^* as a function of r can then be prepared. If the displacements used are the exact values, then the value of k_1^* obtained as r approaches zero would tend to the exact value of the stress intensity factor k_1 associated with the mode 1 conditions. Finite elements displacements obtained using conventional elements have been found to be rather inaccurate at small distances away from the crack-tip. This limiting process is not found, therefore, to be usable in practice. In such cases it was found[13] that with increasing refinement of the element size, the k_1^* curves obtained from the element displacements rapidly approach a constant slope with increasing distance r from the crack-tip. The intercept of the tangent to the constant slope portion of the curve with the k_1^* axis was then used as the k_1 estimate. Chan et al[13] found that tha most accurate estimates for k_1 , for an eccentrically loaded plate with one edge crack, were those obtained from the k_1^* curve corresponding to the U_y (in the x-y plane) displacement on the crack surface.

This method of interpretation has been employed in many investigations including the works based on special crack-tip elements[19] and isoparametric elements[22].

3.2.1.2 The Stress Method

This involves a correlation of the finite element nodal point stresses near the crack-tip with the established crack-tip stress equations. For mode 1 conditions, the stresses in polar co-ordinates terms are :-

$$\sigma_i = \frac{k_1}{(2\pi r)^{\frac{1}{2}}} \quad f_i(\theta) \qquad (3.16)$$

Where,

$$\sigma_1 = \sigma_r , \quad \sigma_2 = \sigma_\theta , \quad \sigma_3 = \tau_{r\theta}$$

and

$$f_1(\theta) = \cos\frac{\theta}{2}\left(1 + \sin^2\frac{\theta}{2}\right)$$

$$f_2(\theta) = \cos^3\frac{\theta}{2}$$

$$f_3(\theta) = \tfrac{1}{2}\cos\frac{\theta}{2}\sin\theta$$

By substituting a finite element nodal point stress σ_i^* at some point (r,θ) near the crack-tip into equations 2.8 , a value of k_1^* may

be calculated from :-

$$k_1^* = (2\pi r)^{\frac{1}{2}} \quad \sigma_i^* / f_i(\theta) \qquad (3.17)$$

From plots of k_1^* as a function of r for a fixed value of θ and a particular stress component, estimates of k_1 can be made. Again if the finite element employed is not capable of representing the stress singularity condition at the crack-tip, the k_1^* curve must be extrapolated from points away from the crack-tip. Chan et al[13] state that for the problem mentioned in the previous section, reasonable estimates of k_1 by the stress method can be obtained from the k_1^* curve corresponding to σ_y (in the x-y plane) on the $\theta = 0$ plane.

In general this method leads to less accurate results than those obtained by the displacement method. This is not unexpected, since the stresses in an assumed displacement solution are themselves inferior in accuracy to the displacements.

3.2.2 The Energy Methods

In general these may be grouped into two basic methods. The first will be referred to as the energy-release rate approach and the second is called the line-integral energy method.

3.2.2.1 Energy-Release Rate Method

An elastic body subjected to applied loads and containing an extending crack provide energy release-rate R available for the crack extension process. This rate is defined as the amount of energy required to produce a unit increase in the area of the free surface of the crack. Referring to figure 3.7 , the available energy for an increment of crack extension dA is provided by work done by the loads $P_i\ dS_i$, and the release dV in the total strain energy V stored in the body. Thus

$$R = P_i \frac{d\delta_i}{dA} - \frac{dV}{dA} \qquad (3.18)$$

Where i,j = 1,2, ... , n and n is the number of applied loads.

The displacements of a linear elastic body are related to the applied loads by

$$\delta_i = \lambda_{ij}\ P_j \qquad (3.19)$$

Where λ_{ij} are the influence coefficients which depend on the

configuration of the body containing the crack area A.

The strain energy in the body is equal to the work done by the loads, i.e.

$$V = \tfrac{1}{2} P_i \delta_i = \tfrac{1}{2} \lambda_{ij} P_i P_j \qquad (3.20)$$

Equations 3.18 and 3.20 give

$$R = P_i \frac{d\delta_i}{dA} - \tfrac{1}{2} \frac{d}{dA} (P_i \delta_i) \qquad (3.21)$$

If either P_i or δ_i is given for each load point i, the corresponding δ_i or P_i must be determined in order to evaluate the derivatives appearing in equation 3.21 . If this can be done, the energy release rate R may be evaluated.

If a system of constant applied forces is acting on the cracked structure, i.e. P_i = constant, equation 3.21 simplifies to :-

$$R = \tfrac{1}{2} P_i \frac{d\delta}{dA} \qquad (3.22)$$

For the particular case of a single applied force P, the energy release rate will be given by

$$R = \tfrac{1}{2} P \frac{d\delta}{dA} \qquad (3.23)$$

Paris and Sih[9] have shown that direct relationships exist between energy-release rates and stress intensity factors. For isotropic materials and plane strain conditions, these are :-

$$R_1 = \frac{(1-\nu^2)}{E} k_1^2$$

$$R_2 = \frac{(1-\nu^2)}{E} k_2^2 \qquad (3.24)$$

$$R_3 = \frac{(1-\nu^2)}{E} k_3^2$$

Where R_1, R_2 and R_3 are the energy-release rates associated with the three modes of stress fields at the crack-tip. If more than one mode exist, the principle of superposition can be used. For plane stress conditions these equations become :-

$$R_1 = \frac{k_1^2}{E}$$

$$R_2 = \frac{k_2^2}{E} \qquad (3.25)$$

$$R_3 = \frac{k_3^2}{E}$$

The above R-k relationships provide a method of evaluating the stress intensity factors from values of energy-release rates. In the finite element method, a cracked structure is represented by a number

of elements jointed at the nodal points. Displacements and forces at these nodal points are the basic results of such an analysis and hence evaluation of the energy-release rate is possible using equations 3.18-3.23 . The stress intensity factors can then be calculated using equations 3.24 and 3.25 .

It has been pointed out[15] that the crack-tip stress field will make relatively little contribution to the over-all deflection of the structure. Adequate representation of this field, a difficulty associated with the use of conventional elements, to determine stresses in the vicinity of the crack-tip is therefore not necessary.

This method of interpretation was developed and used by many authors including Wattwood[14], Dixon and Stranigan[15], Mowbray[37] and Owen and Griffiths[38] . The authors of reference 15 found that, for the mode 1 problems they had analysed, even with one or two elements covering the boundary of the crack, the values of k_1 were only slightly low when obtained by the energy-release rate approach. Owen and Griffiths[38] point out that an advantage of this method is that the results are not so sensitive to the size of the finite element mesh at the crack-tip.

A disadvantage of this approach, in its original form, is that to obtain the energy-release rate R, two finite element solutions are needed which differ only in the crack size. One means of avoiding this requirement is by the 'differential stiffness' procedure[39,40]. This procedure may be explained as follows :-

In a finite element formulation, the structure nodal force vector $\underset{\sim}{F}$ is related to the corresponding generalised displacements $\underset{\sim}{U}$ by

$$\underset{\sim}{F} = \underset{\sim}{K}\,\underset{\sim}{U} \qquad (3.26)$$

For a given system of applied forces a solution may be obtained for the nodal displacements from :-

$$\underset{\sim}{U} = \underset{\sim}{K}^{-1}\,\underset{\sim}{F} \qquad (3.27)$$

Thus for a given crack size, a finite element solution is obtained once $\underset{\sim}{K}^{-1}$ is found. If the crack is now opened by a small distance δa and if $\delta\underset{\sim}{K}$ is the corresponding change in the stiffness matrix, the stiffness equations of the new configuration become :-

$$\underset{\sim}{F} = (\underset{\sim}{K} + \delta\underset{\sim}{K})\,(\underset{\sim}{U} + \delta\underset{\sim}{U}) \qquad (3.28)$$

Where $\delta\underset{\sim}{U}$ is the change in the solution. Ignoring the product of small order terms, equation 3.28 reduces to :-

$$\underset{\sim}{K}\,\delta\underset{\sim}{U} + \delta\underset{\sim}{K}\,\underset{\sim}{U} = 0$$

or

$$\delta\underset{\sim}{U} = -\underset{\sim}{K}^{-1}\,\delta\underset{\sim}{K}\,\underset{\sim}{U} \qquad (3.29)$$

The change in the solution can therefore be calculated directly once δK is known. In practice this calculation is generally simple

because only a small part of SK is populated since the crack extension affects only a few elements in the over-all structure idealization. It follows, therefore, that using this procedure it is possible to calculate the energy-release rate from the solution of the original configuration.

It was pointed out[9] that equations 3.24 and 3.25 assume that the crack is planar and extends in its own plane. It should be remembered that in practice cracks do not extend in a planar manner with k_2 and k_3 present, or even with k_1 alone in anisotropic media, and hence these relationships are of limited application.

3.2.2.2 The Line Integral Energy Method

Rice[36] has shown that the value of the line integral :-

$$J = \int_L (W\,dy - T\frac{du}{dx}\,ds) \qquad (3.30)$$

where L is a contour surrounding the crack-tip as shown in figure 3.8 , is the same for any path and is proportional to the square of the crack-tip stress intensity factor. In equation 3.30 , W is the strain energy density defined by

$$W = W(e) = \int_0 \sigma_{ij}\,d\epsilon_{ij} \qquad (3.31)$$

Where $e = \epsilon_{ij}$ is the infinitesimal strain tensor. T is the traction vector defined according to the outward normal along L, $T_i = \sigma_{ij}\,n_j$. u is the displacement vector and dS is an element of arc length along L.

The line integral is evaluated in an anticlockwise sense starting from the lower crack surface and continuing along the path L to the upper flat surface. This integral being equivalent to the energy-release rate of the previous section and can therefore be used to evaluate the stress intensity factor. For plane strain conditions, for example, Rice[36] gives the following relationship :-

$$k_1^2 = \frac{J\,E}{(1-\nu^2)} \qquad (3.32)$$

which is the same as the first of equations 3.24 .

By numerically evaluating the integral of equation 3.30 , using the finite element results, over a path surrounding the crack-tip, an estimate of the stress intensity factor can be obtained using equation 3.32 . Chan et al[13] have shown that this approach gives values of stress intensity factors which are similar to those obtained by the direct methods.

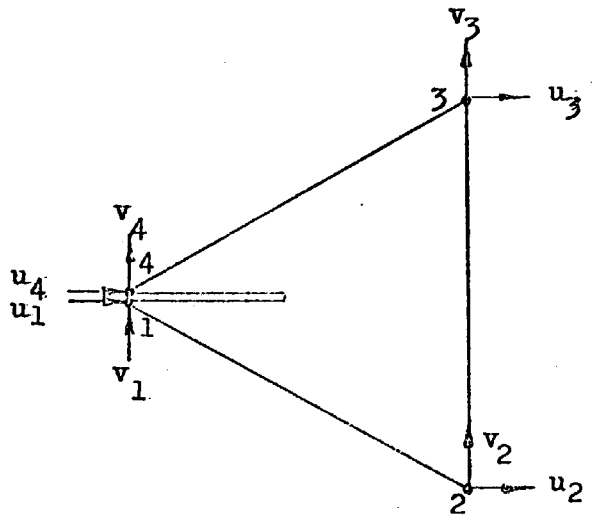

Figure 3.1 Cracked triangle (reference 17)

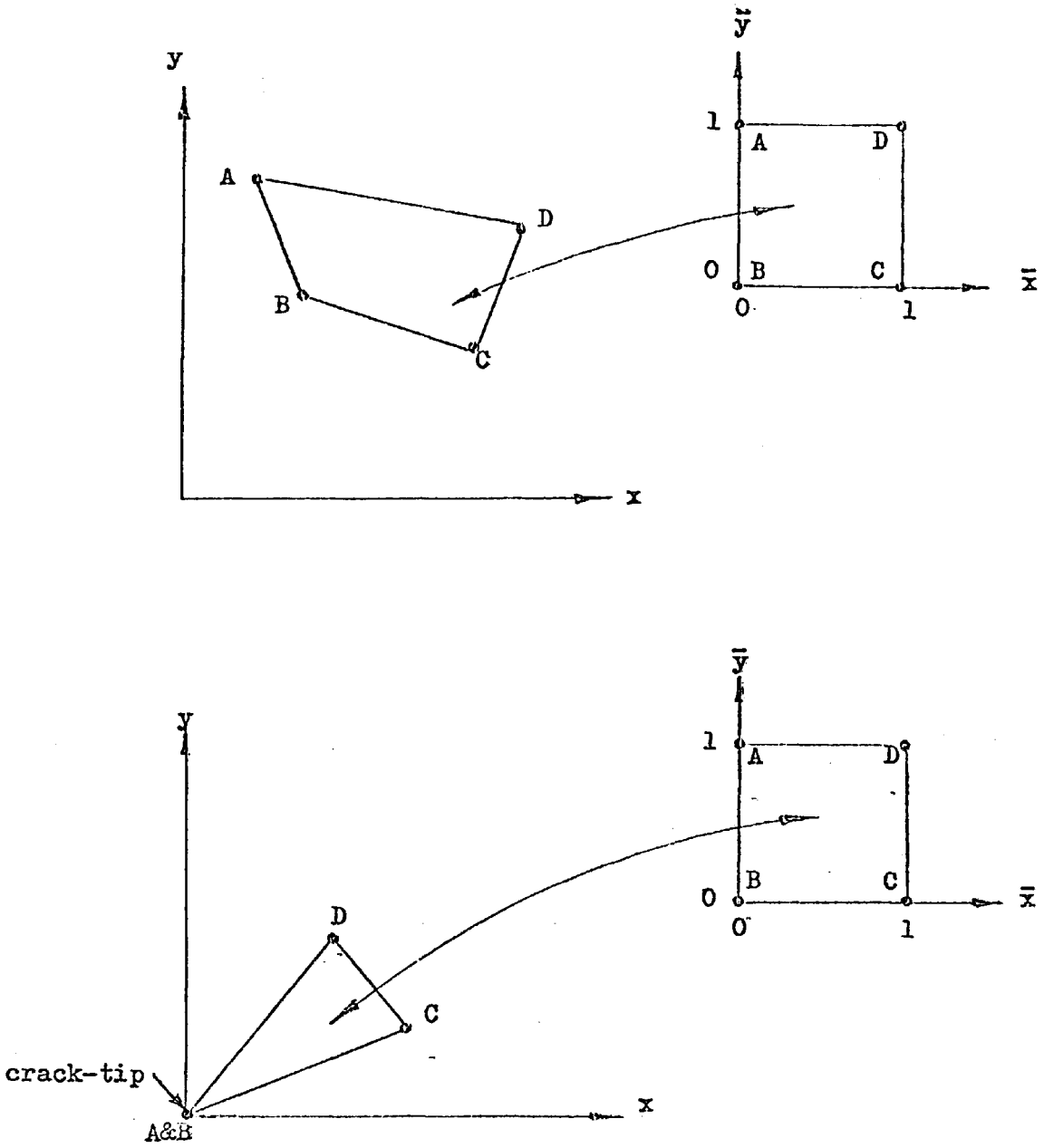

Figure 3.2 Mapping of a square into a quadrilateral or a triangle (reference 21)

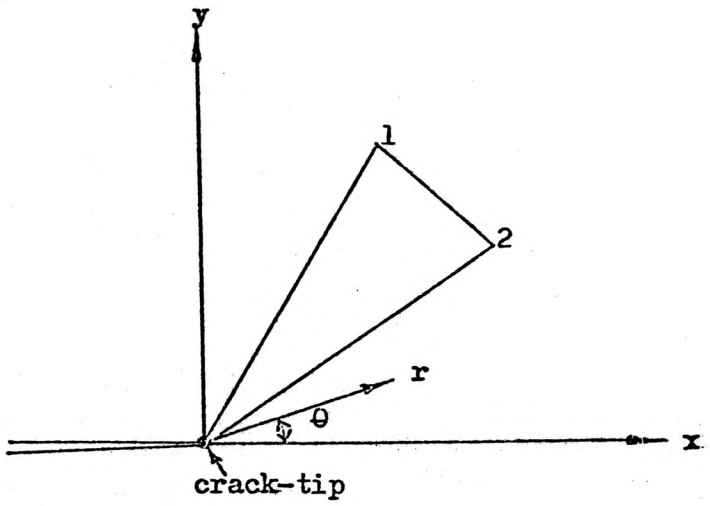

Figure 3.3 Triangular crack-tip element

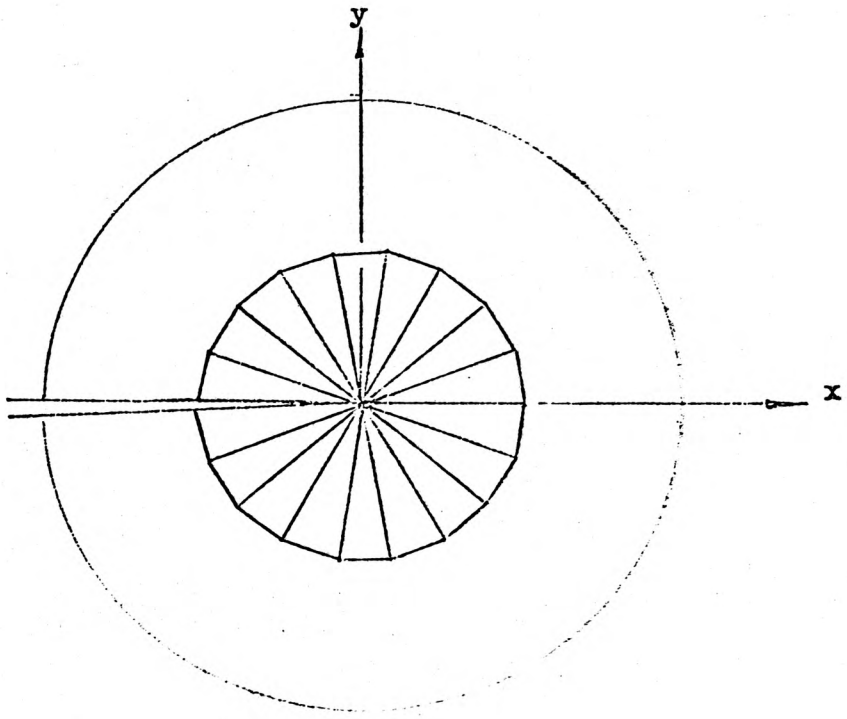

Figure 3.4 Cracked body with singular triangular elements surrounding the crack-tip

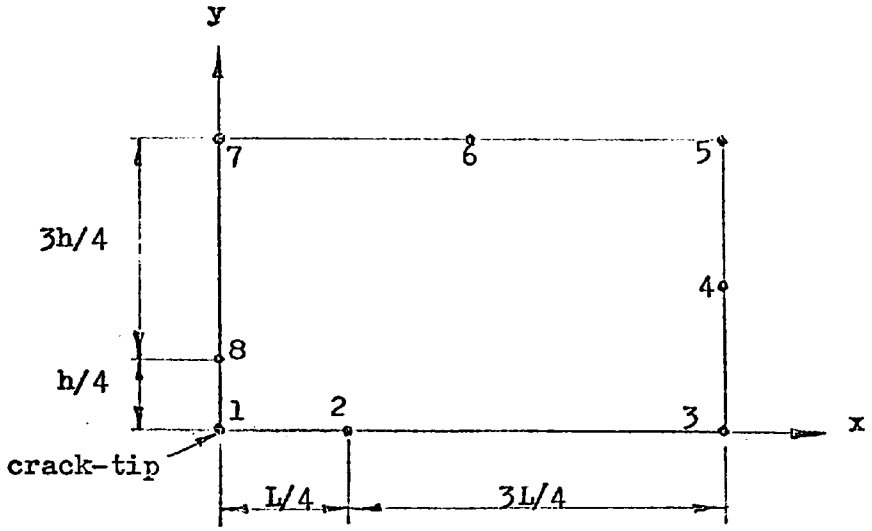

Figure 3.5 Quadrilateral isoparametric singular element (references 22 & 23)

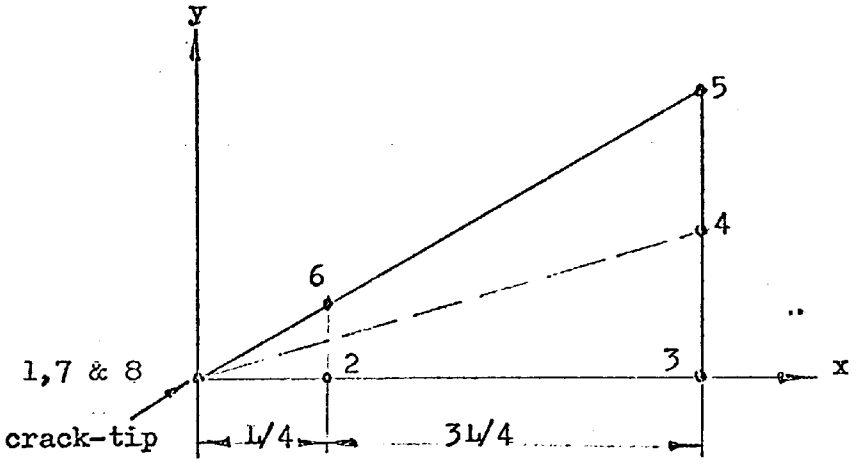

Figure 3.6 Triangular isoparametric singular element (reference 27)

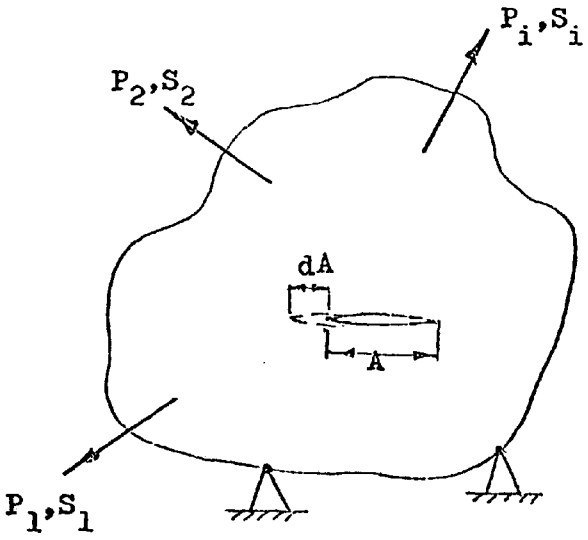

Figure 3.7 Cracked body under arbitrary system of applied loads

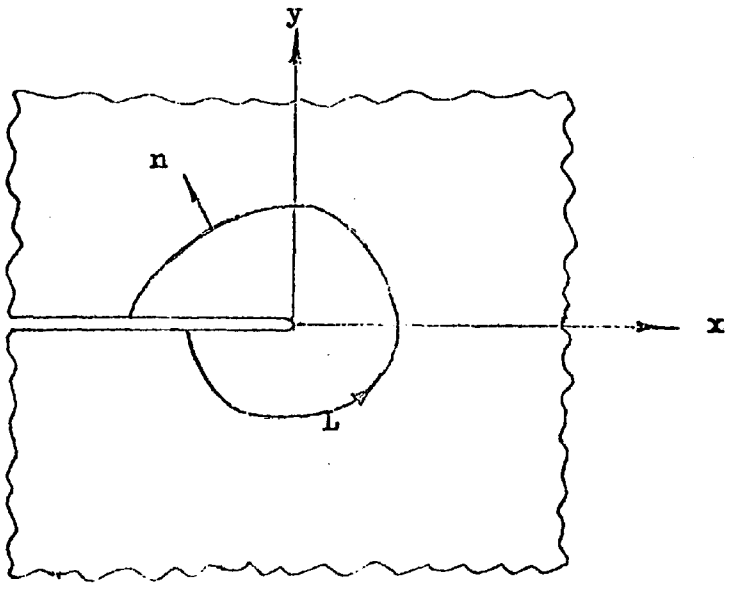

Figure 3.8 Arbitrary contour around crack-tip

CHAPTER 4 FINITE ELEMENTS FOR THE SINGULAR FIELD NEAR THE CRACK-TIP

In this chapter, after a brief outline of the general finite element procedure, the formulation in terms of polar co-ordinates of two element stiffness matrices which take account of the singular condition in the vicinity of the crack-tip is presented.

The first element, designated by I, is entirely new and is 'trapezoidal' in shape having two straight and two circular boundaries. The element is formed from two 'triangular' subregions suitable for combination with constant strain triangular elements[4].

The second element, designated by II, is 'triangular' and is based on simple displacement functions similar to those used by Wilson[19]. The difference between Wilson's element and that presented here is that the former have all its boundaries straight while the latter has one of its boundaries circular. When analysing problems, a cluster of this type of elements, all having a common nodal point at the tip of the crack, is surrounded by elements I. The circular boundary of element II made it possible to preserve the true geometry of the interface between the two types of elements.

Other attempts at developing singular elements which were unsuccessful are briefly mentioned.

The chapter is concluded with a detailed numerical study on the effectiveness of the new elements by analysing two problems under mode 1 and mode 2 conditions for which 'exact' solutions are available.

4.1 The Finite Element Method

The finite element method is described in detail in the literature and will only be outlined briefly here. In this method the structure is divided into a number of finite subregions (elements) connected at discrete points called nodes. For each subregion, a displacement function in terms of discrete parameters a_i ($i = 1,2,.....n$) is prescribed. An approximate solution for these parameters can be obtained by minimising the potential energy of the structure and loads under the constraints imposed. If the prescribed displacement function satisfy certain requirements with respect to continuity and conformity, it can be shown that as the size of the elements decrease indefinitely, the solutions obtained converge to the exact solution. The minimisation procedure involves the development of the over-all structure stiffness matrix from individual element stiffness matrices $\underset{\sim}{K}_e$. For two dimensional analysis and in terms of polar co-ordinates, $\underset{\sim}{K}_e$ may be evaluated from :-

$$\underset{\sim}{K}_e = \underset{\sim}{C}^{-1,T} \iint \underset{\sim}{B}^T \underset{\sim}{D} \underset{\sim}{B} \; r \, d\theta \, dr \quad \underset{\sim}{C}^{-1} \tag{4.1}$$

The matrices $\underset{\sim}{C}$, $\underset{\sim}{B}$ and $\underset{\sim}{D}$ are defined by the following equations :-

$$\underset{\sim}{U}_e = \underset{\sim}{C} \, \underset{\sim}{a} \tag{4.2}$$

$$\underset{\sim}{\epsilon}_e = \underset{\sim}{B} \, \underset{\sim}{a} \tag{4.3}$$

$$\underset{\sim}{\sigma}_e = \underset{\sim}{D} \, \underset{\sim}{\epsilon}_e \tag{4.4}$$

Where

$\underset{\sim}{U}_e$ is a vector containing the element nodal displacements,

$\underset{\sim}{\epsilon}_e$ " " " " " strains,

and $\underset{\sim}{\sigma}_e$ " " " " " stresses.

The resulting structure stiffness matrix $\underset{\sim}{K}$ is a square matrix, symmetrical about the leading diagonal, relating the nodal forces $\underset{\sim}{F}$ to the corresponding structure nodal displacements $\underset{\sim}{U}$ by the following equation :-

$$\underset{\sim}{F} = \underset{\sim}{K}\,\underset{\sim}{U} \tag{4.5}$$

For a given system of applied forces and/or displacements a solution may be obtained for the nodal displacements by inverting the structure stiffness matrix. Thus

$$\underset{\sim}{U} = \underset{\sim}{K}^{-1}\,\underset{\sim}{F} \tag{4.6}$$

Once the nodal displacements are calculated the element nodal stresses (or stresses at any point within the element) may be evaluated from the following equation :-

$$\underset{\sim}{\sigma}_e = \underset{\sim}{S}_e\,\underset{\sim}{C}^{-1}\,\underset{\sim}{U}_e \tag{4.7}$$

Where $\underset{\sim}{S}_e$ is an element stress matrix given by

$$\underset{\sim}{S}_e = \underset{\sim}{D}\,\underset{\sim}{B} \qquad (4.8)$$

B is the strain-displacement matrix containing the element strains given byequations 4.11-4.13 . $\underset{\sim}{D}$ is the rigidity matrix given by

for plane stress

$$\underset{\sim}{D} = \frac{E\,t}{(1-\nu^2)} \begin{bmatrix} 1 & \nu & 0 \\ \nu & 1 & 0 \\ 0 & 0 & \frac{(1-\nu)}{2} \end{bmatrix} \qquad (4.9)$$

for plane strain

$$\underset{\sim}{D} = \frac{E\,t}{(1+\nu)(1-2\nu)} \begin{bmatrix} 1-\nu & \nu & 0 \\ \nu & 1-\nu & 0 \\ 0 & 0 & \frac{(1-\nu)}{2} \end{bmatrix} \qquad (4.10)$$

where E is the elasticity modulus, t is the thickness and ν is Poisson's ratio.

4.2 Trapezoidal Element I

The stiffness matrix formulated here is for the 'trapezoidal' element shown in figure 4.3 . The element has four boundaries, two of which are straight in the radial direction and the other two circular. The element is initially considered to be made up of two 'triangular' subregions as shown in figure 4.1 . The procedure adopted in forming the 'trapezoidal' element from the two triangles will be described later. The element is derived in terms of the polar co-ordinates system shown.

4.2.1 Derivation of the Displacement Functions

Ashwell, Sabir and Roberts[7] demonstrated how a satisfactory displacement shape function can be derived from assumed simple strain functions by integrating the strain-displacement equations. Following their method and using the notation adopted in reference 10 , the strain components for two dimensional analysis are :-

$$\epsilon_r = \frac{\partial u}{\partial r} = f_r \qquad (4.11)$$

$$\epsilon_\theta = \frac{u}{r} + \frac{\partial v}{r\partial \theta} = f_\theta \qquad (4.12)$$

$$\gamma_{r\theta} = \frac{\partial u}{r\partial \theta} + \frac{\partial v}{\partial r} - \frac{v}{r} = f_{r\theta} \qquad (4.13)$$

where f_r , f_θ and $f_{r\theta}$ are functions of r amd θ .

If $f_r = f_\theta = f_{r\theta} = 0$, equations 4.11-4.13 can be integrated to give the following complimentary functions :-

$$u = a_1 \sin\theta + a_2 \cos\theta$$

$$v = a_1 \cos\theta - a_2 \sin\theta + a_3 r \qquad (4.14)$$

where a_1 , a_2 and a_3 are independent constants of integration.

Equations 4.14 represent displacements with zero strains, i.e. they represent rigid body displacements.

If $f_r \neq 0$, $f_\theta \neq 0$ and $f_{r\theta} \neq 0$, particular integrals can be obtained from equations 4.11-4.13 by making suitable choices for f_r , f_θ and $f_{r\theta}$. Each 'triangular' subregion will have six degrees of freedom, namely u and v at each node, and thus the shape function is expected to have six independent constants - three are required for the rigid body displacements, equations 4.14 , leaving three constants available for the strain functions. Consideration of the crack-tip equations 2.8 and 2.10 suggest strain functions of the form $f(\theta)/r^{\frac{1}{2}}$. The following strain functions are thus assumed :-

$$f_r = \frac{1}{r^{\frac{1}{2}}} (b_1 + b_2 \theta)$$

$$f_\theta = \frac{1}{r^{\frac{1}{2}}} (b_3 + b_4 \theta) \qquad (4.15)$$

$$f_{r\theta} = \frac{1}{r^{\frac{1}{2}}} (b_5 + b_6 \theta)$$

Where b_1 , b_2 , ... b_6 are constants, three of which are independent. The three dependent constants are eliminated by satisfying the compatibility equations 4.11 - 4.13 . By substituting for the strain functions f_r and f_θ in equations 4.11 and 4.12 , the following particular integrals may be obtained :-

$$u = 2 (b_1 + b_2 \theta) \; r^{\frac{1}{2}} \tag{4.16}$$

$$v = \left[(b_3 - b_1) \theta + \frac{1}{2} (b_4 - 2 b_2) \theta^2 \right] r^{\frac{1}{2}} \tag{4.17}$$

Substituting for u , v and $f_{r\theta}$ in equation 4.13 , we have :-

$$b_4 = b_5 = 2 a_2 \tag{4.18}$$

$$b_6 = b_1 - \frac{1}{2} b_3 \tag{4.19}$$

Eliminating b_4 from equation 4.17 , we have :-

$$u = 2 (b_1 + b_2 \theta) \; r^{\frac{1}{2}} \tag{4.20}$$

$$v = (b_3 - 2 b_1) \theta \; r^{\frac{1}{2}} \tag{4.21}$$

Equations 4.20 and 4.21 can be simplified slightly by observing that :-

(i) u requires an independent term containing $r^{\frac{1}{2}}$ and a term containing $r^{\frac{1}{2}} \theta$.

(ii) v requires one independent term containing $r^{\frac{1}{2}} \theta$ (as b_1 is independent of $(b_3 - 2 b_1)$ if b_3 is independent).

Thus,

$$u = (a_4 + a_5 \theta) r^{\frac{1}{2}} \tag{4.22}$$

$$v = a_6 \theta r^{\frac{1}{2}} \tag{4.23}$$

The complete solution for u and v thus become :-

$$u = a_1 \sin \theta + a_2 \cos \theta + a_4 r^{\frac{1}{2}} + a_5 r^{\frac{1}{2}} \theta \tag{4.24}$$

$$v = a_1 \cos \theta - a_2 \sin \theta + a_3 r + a_6 r^{\frac{1}{2}} \theta \tag{4.25}$$

The corresponding expressions for the strains are :-

$$\epsilon_r = \frac{1}{2} r^{-\frac{1}{2}} (a_4 + a_5 \theta) \tag{4.26}$$

$$\epsilon_\theta = \frac{1}{r^{\frac{1}{2}}} (a_4 + a_6 + a_5 \theta) \tag{4.27}$$

$$\gamma_{r\theta} = \frac{1}{2} r^{-\frac{1}{2}} (2 a_5 - a_6 \theta) \tag{4.28}$$

Consideration of these equations indicate that ϵ_r and ϵ_θ each contain one independent constant, while $\gamma_{r\theta}$ is completely dependent on ϵ_r and ϵ_θ . It is considered that this is the only possibility if terms of $f(\theta)/r^{\frac{1}{2}}$ are to be used while satisfying the compatibility equations. It is also observed from equations 4.24 and 4.25 that coupling in the displacements is provided only by the rigid body terms.

4.2.2 Stiffness Matrices for the 'Triangular' Sub-elements

The shape functions (equations 4.24 and 4.25) are now used to develop the stiffness matrices for the two sub-elements Q and Q* shown in figure 4.1 . The positive directions for the radial displacement u and circumferential displacement v together with their corresponding forces F_u and F_v are shown in figure 4.2 . The generalised nodal displacement vector $\underset{\sim}{U}_e$ for each sub-element is calculated by substituting for the co-ordinates of the three nodal points shown in figure 4.1 , in equations 4.24 and 4.25 . Writing the result in matrix notation, we have :-

$$\underset{\sim}{U}_e = \begin{Bmatrix} u \\ v \end{Bmatrix} = \underset{\sim}{C}\,\underset{\sim}{a} \qquad (4.29)$$

The $\underset{\sim}{C}$ matrices for the sub-elements Q and Q* are given on pages 68 and 69 . The six constants a_1 to a_6 are expressed in terms of the six nodal displacements by multiplying both sides of equation 4.29 by the inverse of $\underset{\sim}{C}$. Thus,

$$\underset{\sim}{a} = \underset{\sim}{C}^{-1}\,\underset{\sim}{U}_e \qquad (4.30)$$

$$
\begin{bmatrix} u_1 \\ v_1 \\ u_2 \\ v_2 \\ u_3 \\ v_3 \end{bmatrix} =
\left[\begin{array}{c|c|c|c|c|c}
0 & 1 & 0 & R_1^{\frac{1}{2}} & 0 & 0 \\
\hline
1 & 0 & R_1 & 0 & 0 & 0 \\
\hline
0 & 1 & 0 & R_2^{\frac{1}{2}} & 0 & 0 \\
\hline
1 & 0 & R_2 & 0 & 0 & 0 \\
\hline
S & C & 0 & R_2^{\frac{1}{2}} & R_2^{\frac{1}{2}} & 0 \\
\hline
C & -S & R_2 & 0 & 0 & R_2^{\frac{1}{2}}
\end{array}\right]
\begin{bmatrix} a_1 \\ a_2 \\ a_3 \\ a_4 \\ a_5 \\ a_6 \end{bmatrix}
$$

where $S = \sin \alpha$

$C = \cos \alpha$

For other notations see figure 4.1

The $\underset{\sim}{C}$ Matrix for Triangular Sub-Element Q

$$\begin{bmatrix} u_1 \\ v_1 \\ u_2 \\ v_2 \\ u_3 \\ v_3 \end{bmatrix} = \left[\begin{array}{c|c|c|c|c|c} 0 & 1 & 0 & R_1^{\frac{1}{2}} & 0 & 0 \\ \hline 1 & 0 & R_1 & 0 & 0 & 0 \\ \hline S & C & 0 & R_1^{\frac{1}{2}} & R_1^{\frac{1}{2}} & 0 \\ \hline C & -S & R_1 & 0 & 0 & R_1^{\frac{1}{2}} \\ \hline S & C & 0 & R_2^{\frac{1}{2}} & R_2^{\frac{1}{2}} & 0 \\ \hline C & -S & R_2 & 0 & 0 & R_2^{\frac{1}{2}} \end{array}\right] \begin{bmatrix} a_1 \\ a_2 \\ a_3 \\ a_4 \\ a_5 \\ a_6 \end{bmatrix}$$

where $S = \sin \alpha$

$C = \cos \alpha$

For other notations see figure 4.1

The $\underset{\sim}{C}$ Matrix for Triangular Sub-Element Q^*

The $\underset{\sim}{C}^{-1}$ matrices for the two sub-elements are calculated and the results are given on pages 71 and 72.

The strains at any point in the sub-elements Q and $\overset{*}{Q}$ are expressed in terms of u and v and their derivatives using equations 4.11 - 4.13 . Substituting for the displacements from equations 4.24 and 4.25 and carrying out the differentiations, the strains can be expressed in terms of the 'a' constants as shown in equations 4.26 - 4.28 . Writing the results in a matrix notation, we have :-

$$\underset{\sim}{\epsilon}_e = \begin{Bmatrix} \epsilon_r \\ \epsilon_\theta \\ \gamma_{r\theta} \end{Bmatrix} = \underset{\sim}{B}\,\underset{\sim}{a} \qquad (4.31)$$

Where $\underset{\sim}{B}$ is a (3 x 6) strain matrix given on page 73.

The stresses are related to the strains by Hooke's law. In matrix notation this can be written as :-

$$\underset{\sim}{\sigma}_e = \begin{Bmatrix} \sigma_r \\ \sigma_\theta \\ \tau_{r\theta} \end{Bmatrix} = \underset{\sim}{D}\,\underset{\sim}{\epsilon}_e \qquad (4.32)$$

Where $\underset{\sim}{D}$ is the rigidity matrix given by equation 4.9 for plane stress and by equation 4.10 for plane strain.

$$\begin{bmatrix} a_1/H_1 \\ a_2/H_2 \\ a_3/H_1 \\ a_4/H_2 \\ a_5 \\ a_6 \end{bmatrix} = H_3^{-1} \begin{bmatrix} 0 & R_2 & 0 & -R_1 & 0 & 0 \\ R_2^{\frac{1}{2}} & 0 & -R_1^{\frac{1}{2}} & 0 & 0 & 0 \\ 0 & -1 & 0 & 1 & 0 & 0 \\ -1 & 0 & 1 & 0 & 0 & 0 \\ (1-C)\,H_4 & -S\,R_2 & H_5 & S\,R_1 & R_2-R_1 & 0 \\ H_6 & (1-C)\,R_2 & H_7 & CR_1-R_2 & 0 & R_2-R_1 \end{bmatrix} \begin{bmatrix} u_1 \\ v_1 \\ u_2 \\ v_2 \\ u_3 \\ v_3 \end{bmatrix}$$

where

$H_1 = \alpha R_2^{\frac{1}{2}}$

$H_2 = \alpha R_2^{\frac{1}{2}} (R_2^{\frac{1}{2}} - R_1^{\frac{1}{2}})$

$H_3 = (R_1^{\frac{1}{2}} + R_2^{\frac{1}{2}}) H_2$

$H_4 = R_2^{\frac{1}{2}} H_2/\alpha$

$H_5 = (R_2^{\frac{1}{2}} - R_1^{\frac{1}{2}}) (C R_1^{\frac{1}{2}} - R_2^{\frac{1}{2}})$

$H_6 = S H_2/\alpha$

$H_7 = - S R_1^{\frac{1}{2}} (R_2^{\frac{1}{2}} - R_1^{\frac{1}{2}})$

$S = \sin\alpha \qquad C = \cos\alpha$

For other notations see figure 4.1

The $\underset{\sim}{C}^{-1}$ Matrix for Triangular Sub-Element Q

$$\begin{bmatrix} a_1/J_1 \\ a_2/J_1 \\ a_3/\alpha \\ a_4/\alpha \\ a_5 \\ a_6 \end{bmatrix} = J_2^{-1} \begin{bmatrix} 0 & CJ_3 & SJ_4 & J_5 & -SR_1 & -CR_1 \\ 0 & -SJ_3 & R_2^{\frac{1}{2}}J_5 & -SJ_4 & -R_1^{\frac{1}{2}}J_5 & SR_1 \\ 0 & R_2^{\frac{1}{2}}-R_1^{\frac{1}{2}} & -SR_2^{\frac{1}{2}} & -CR_2^{\frac{1}{2}} & SR_1^{\frac{1}{2}} & CR_1^{\frac{1}{2}} \\ J_6 & SJ_3 & -R_2^{\frac{1}{2}}J_5 & SJ_4 & R_1^{\frac{1}{2}}J_5 & -SR_1 \\ -J_6 & -SJ_3 & R_2-R_1 & -SJ_4 & (1-C)J_7 & SR_1 \\ 0 & R_1-R_2 & R_2^{\frac{1}{2}}J_8 & CR_2-R_1 & -R_1^{\frac{1}{2}}J_8 & (1-C)R_1 \end{bmatrix} \begin{bmatrix} u_1 \\ v_1 \\ u_2 \\ v_2 \\ u_3 \\ v_3 \end{bmatrix}$$

where

$J_1 = \alpha R_1^{\frac{1}{2}}$

$J_2 = \alpha R_1^{\frac{1}{2}} (R_2^{\frac{1}{2}} - R_1^{\frac{1}{2}}) (R_1^{\frac{1}{2}} + C R_2^{\frac{1}{2}})$

$J_3 = R_2^{\frac{1}{2}} (R_2^{\frac{1}{2}} - R_1^{\frac{1}{2}})$

$J_4 = R_1^{\frac{1}{2}} R_2^{\frac{1}{2}}$

$S = \sin \alpha$

$J_5 = (C R_1^{\frac{1}{2}} + R_2^{\frac{1}{2}})$

$J_6 = J_2/\alpha R_1^{\frac{1}{2}}$

$J_7 = R_1^{\frac{1}{2}} (R_1^{\frac{1}{2}} - R_2^{\frac{1}{2}})$

$J_8 = S (R_1^{\frac{1}{2}} + R_2^{\frac{1}{2}})$

$C = \cos \alpha$

For other notations see figure 4.1

The $\underset{\sim}{C}^{-1}$ Matrix for Triangular Sub-Element Q*

$$\begin{bmatrix} \epsilon_r \\ \hline \epsilon_\theta \\ \hline \gamma_{r\theta} \end{bmatrix} = \frac{1}{2\, r^{\frac{1}{2}}} \left[\begin{array}{c|c|c|c|c|c} 0 & 0 & 0 & 1 & \theta & 0 \\ \hline 0 & 0 & 0 & 2 & 2\,\theta & 2 \\ \hline 0 & 0 & 0 & 0 & 2 & -\theta \end{array}\right] \begin{bmatrix} a_1 \\ \hline a_2 \\ \hline a_3 \\ \hline a_4 \\ \hline a_5 \\ \hline a_6 \end{bmatrix}$$

The $\underset{\sim}{B}$ Matrix for Sub-Elements Q and Q^*

We now have all the matrices required for the evaluation of the stiffness matrices for the two sub-elements Q and Q^*. The matrix product $\underset{\sim}{B}^T \underset{\sim}{D} \underset{\sim}{B}$ $(= \underset{\sim}{H})$ appearing in the general formula (equation 4.1) is evaluated. This is a (6 x 6) symmetrical matrix given on page 75 . The stiffness matrices for the two sub-elements Q and Q^* are now respectively calculated from the following equations :-

$$\underset{\sim}{K}_e = \underset{\sim}{C}^{-1,T} \int_{f(\theta)}^{R_2} \int_{0}^{\alpha} \underset{\sim}{H} \; r \, d\theta \, dr \quad \underset{\sim}{C}^{-1} \qquad (4.33)$$

$$\underset{\sim}{K}_e = \underset{\sim}{C}^{-1,T^*} \int_{R_1}^{f(\theta)} \int_{0}^{\alpha} \underset{\sim}{H} \; r \, d\theta \, dr \quad \underset{\sim}{C}^{-1^*} \qquad (4.34)$$

where $f(\theta) = q\, R_1 / (q \cos\theta - \sin\theta) = r$

which represents the equation of the straight line boundary common to the two sub-elements, and

$$q = R_2 \sin\alpha / (R_2 \cos\alpha - R_1)$$

R_1 , R_2 and α are as defined in figure 4.1 .

$$\underset{\sim}{H} = \frac{E\,t}{4r(1-\nu^2)}$$

$$\begin{bmatrix}
0 & 0 & 0 & 0 & 0 & 0 \\
 & 0 & 0 & 0 & 0 & 0 \\
 & & 0 & 0 & 0 & 0 \\
 & & & 5+4\nu & (5+4\nu)\theta & 4+2\nu \\
 & & & & (5+4\nu)\theta^2 + 2(1-\nu) & 3(1+4\nu)\theta \\
 & & & & & (1-\nu)\theta^2/2 + 4
\end{bmatrix}$$

symmetrical

The $\underset{\sim}{H}$ Matrix for Sub-Elements Q and Q^*

4.2.3 Stiffness Matrix for the 'Trapezoidal' Element

The two sub-elements are now combined to obtain the stiffness matrix for the trapezoidal element I shown in figure 4.3 . The positive directions of displacements and their corresponding forces are shown in figure 4.4 . Following the node numbering system shown in figures 4.1 and 4.3 , it is observed that the two sub-elements Q and Q^* are connected at nodes 1 and 1^*, and at nodes 3 and 3^* to give nodes 1 and 4 , respectively on element I. Nodes 2 and 3 of I are nodes 2 of Q^* and 2 of Q respectively. Such observation will determine the positions of the $Q_{i,j}$ and $Q^*_{i,j}$ $(i,j = 1,2, \ldots, 6)$ coefficients in the over-all (8 x 8) stiffness matrix for element I. Where a contribution is made by both Q and Q^*, the two coefficients are superimposed. The resulting matrix is given on page 77 , in terms of the coefficients of Q and Q^* stiffness matrices.

$$
\begin{bmatrix} F_{u1} \\ F_{v1} \\ F_{u2} \\ F_{v2} \\ F_{u3} \\ F_{v3} \\ F_{u4} \\ F_{u4} \end{bmatrix} =
\begin{bmatrix}
Q_{1,1}+Q^{*}_{1,1} & Q_{1,2}+Q^{*}_{1,2} & Q^{*}_{1,3} & Q^{*}_{1,4} & Q_{1,3} & Q_{1,4} & Q_{1,5}+Q^{*}_{1,5} & Q_{1,6}+Q^{*}_{1,6} \\
 & Q_{2,2}+Q^{*}_{2,2} & Q^{*}_{2,3} & Q^{*}_{2,4} & Q_{2,3} & Q_{2,4} & Q_{2,5}+Q^{*}_{2,5} & Q_{2,6}+Q^{*}_{2,6} \\
 & & Q^{*}_{3,3} & Q^{*}_{3,4} & 0 & 0 & Q^{*}_{3,5} & Q^{*}_{3,6} \\
 & & & Q^{*}_{4,4} & 0 & 0 & Q^{*}_{4,5} & Q^{*}_{4,6} \\
 & & & & Q_{3,3} & Q_{3,4} & Q_{3,5} & Q_{3,6} \\
 & & \text{symmetrical} & & & Q_{4,4} & Q_{4,5} & Q_{4,6} \\
 & & & & & & Q_{5,5}+Q^{*}_{5,5} & Q_{5,6}+Q^{*}_{5,6} \\
 & & & & & & & Q_{6,6}+Q^{*}_{6,6}
\end{bmatrix}
\begin{bmatrix} u_1 \\ v_1 \\ u_2 \\ v_2 \\ u_3 \\ v_3 \\ u_4 \\ v_4 \end{bmatrix}
$$

The Stiffness Matrix for the Trapezoidal Element

4.3 Triangular Element II

In this section a stiffness matrix for the 'triangular' element shown in figure 4.5 is presented. The positive directions of displacements and their corresponding forces are as shown. The element stiffness matrix is based on displacement shape functions (embedding the singularity associated with the crack-tip region) similar to those suggested by Wilson[19] . These are :-

$$u = (a_1 + a_2\,\theta)\; r^{\frac{1}{2}} \tag{4.35}$$

$$v = (a_3 + a_4\,\theta)\; r^{\frac{1}{2}} \tag{4.36}$$

The corresponding strain components are obtained from equations 4.11 - 4.13 . These are :-

$$\epsilon_r = \frac{1}{2\,r^{\frac{1}{2}}}\;(a_1 + a_2\,\theta) \tag{4.37}$$

$$\epsilon_\theta = \frac{1}{r^{\frac{1}{2}}}\;(a_1 + a_4 + a_2\,\theta) \tag{4.38}$$

$$\gamma_{r\theta} = \frac{1}{2\,r^{\frac{1}{2}}}\;(2\,a_2 - a_3 - a_4\,\theta) \tag{4.39}$$

It is observed that ϵ_θ and $\gamma_{r\theta}$ each contain one independent constant, while ϵ_r is dependent on ϵ_θ and $\gamma_{r\theta}$.

While Wilson's element has three straight boundaries, the element presented here has one of its boundaries circular. This is done so that when surrounded by the trapezoidal elements (I), developed in the previous section, the present element (II) will preserve the true geometry at the common interface.

Referring to figure 4.5 , the element will have a total of four degrees of freedom, namely u and v at each node. When analysing problems, the crack-tip will be considered to be enclosed by a number of such elements, all having a common node at the tip.

The nodal displacement vector $\underset{\sim}{U}_e$ is calculated by substituting for the co-ordinates of the two nodal points shown in figure 4.5 , in equations 4.35 and 4.36 . The resulting $\underset{\sim}{C}$ matrix (equation 4.29) is given by :-

$$\begin{bmatrix} u_1 \\ v_1 \\ u_2 \\ v_2 \end{bmatrix} = \left[\begin{array}{c|c|c|c} R^{\frac{1}{2}} & -\alpha R^{\frac{1}{2}} & 0 & 0 \\ \hline 0 & 0 & R^{\frac{1}{2}} & -\alpha R^{\frac{1}{2}} \\ \hline R^{\frac{1}{2}} & \alpha R^{\frac{1}{2}} & 0 & 0 \\ \hline 0 & 0 & R^{\frac{1}{2}} & \alpha R^{\frac{1}{2}} \end{array}\right] \begin{bmatrix} a_1 \\ a_2 \\ a_3 \\ a_4 \end{bmatrix}$$

The inverse of this matrix, i.e. $\underset{\sim}{C}^{-1}$ (equation 4.30) is given by :-

$$\begin{bmatrix} a_1 \\ a_2 \\ a_3 \\ a_4 \end{bmatrix} = \frac{1}{2\alpha R^{\frac{1}{2}}} \begin{bmatrix} \alpha & 0 & \alpha & 0 \\ -1 & 0 & 1 & 0 \\ 0 & \alpha & 0 & \alpha \\ 0 & -1 & 0 & 1 \end{bmatrix} \begin{bmatrix} u_1 \\ v_1 \\ u_2 \\ v_2 \end{bmatrix}$$

The strain matrix $\underset{\sim}{B}$ (equation 4.31) is obtained by substituting for the displacements from equations 4.35 and 4.36 in equations 4.11 - 4.13 and carrying out the differentiation. The resulting (3 x 4) matrix is given by :-

$$\begin{bmatrix} \epsilon_r \\ \epsilon_\theta \\ \gamma_{r\theta} \end{bmatrix} = \frac{1}{2 R^{\frac{1}{2}}} \begin{bmatrix} 1 & \theta & 0 & 0 \\ 2 & 2\theta & 0 & 2 \\ 0 & 2 & -1 & -\theta \end{bmatrix} \begin{bmatrix} a_1 \\ a_2 \\ a_3 \\ a_4 \end{bmatrix}$$

The rigidity matrix $\underset{\sim}{D}$ is given by either of the two equations 4.9 and 4.10 .

We now have all the matrices required for the evaluation of the element stiffness matrix II given by equation 4.1 . The result is a

(4 x 4) matrix relating the element nodal force vector $\underset{\sim}{F}_e$ to the corresponding element nodal displacement vector $\underset{\sim}{U}_e$. This is given as follows :-

$$\begin{bmatrix} F_{u1} \\ F_{v1} \\ F_{u2} \\ F_{v2} \end{bmatrix} = \frac{E\,t}{24(1-\nu^2)\alpha} \begin{bmatrix} 4J_1 + 6J_2 & -9J_3 & 2J_1 - 6J_2 & 3J_4 \\ & 2J_5 + 12 & -3J_4 & J_5 - 12 \\ & & 4J_1 + 6J_2 & 9J_3 \\ \text{symmetrical} & & & 2J_5 + 12 \end{bmatrix} \begin{bmatrix} u_1 \\ v_1 \\ u_2 \\ v_2 \end{bmatrix}$$

where

$$J_1 = (5 + 4\nu)\,\alpha^2 \qquad J_4 = (5 + \nu)\,\alpha$$

$$J_2 = 1 - \nu \qquad J_5 = (1 - \nu)\,\alpha^2$$

$$J_3 = (1 + \nu)\,\alpha$$

E is the elasticity modulus, t is the thickness and ν is Poisson's ratio.

The stiffness matrix given here is for plane stress. The corresponding matrix for plane strain conditions may be obtained by replacing E by $E/(1 - \nu^2)$ and ν by $\nu/(1 - \nu)$.

4.4 Other Elements

Other attempts at deriving stiffness matrices for the trapezoidal element (figure 4.3) and the triangular element (figure 4.5) from alternative displacement functions were made. These elements, which are briefly reported on in this section, were found to be unsatisfactory and therefore disregarded.

4.4.1 'Trapezoidal' Element I*

A more direct approach for deriving displacement functions for the trapezoidal element shown in figure 4.3 is by considering the element itself, rather than the two triangular sub-regions (figure 4.1) . In this way the element has four nodes, at each of which two degrees of freedom are prescribed making a total of eight degrees of freedom. The displacement functions will thus be expected to have eight independent constants. Using the method of reference 7, adopted in section 4.2, three of these constants are required for the rigid body modes as represented in equations 4.14 , leaving five for the strain functions. Carrying on with the procedure followed in section 4.2 and assigning terms of the form $f(\theta)/r^{\frac{1}{2}}$ for the strains, particular integrals for the compatibility equations 4.11 - 4.13 may be obtained. The resulting complete solution for the displacements is as follows :-

$$u = a_1 \sin\theta + a_2 \cos\theta + a_4 r^{\frac{1}{2}} + a_5 r^{\frac{1}{2}}\theta + a_6 r^{\frac{1}{2}}\theta^2$$

$$v = a_1 \cos\theta - a_2 \sin\theta + a_3 r + a_7 r^{\frac{1}{2}}\theta + a_8 r^{\frac{1}{2}}\theta^2 \qquad (4.40)$$

The corresponding expressions for the strains are :-

$$\epsilon_r = \frac{1}{2}\frac{1}{r^2}\left(a_4 + a_5\,\theta + a_6\,\theta^2\right)$$

$$\epsilon_\theta = \frac{1}{r^2}\left(a_4 + a_7 + (a_5 + 2\,a_8)\,\theta + a_6\,\theta^2\right) \qquad (4.41)$$

$$\gamma_{r\theta} = \frac{1}{2}\frac{1}{r^2}\left(2\,a_5 + (4\,a_6 - a_7)\,\theta - a_8\,\theta^2\right)$$

It was found that the (8 x 8) $\underset{\sim}{C}$ matrix (see equation 4.29) resulting from equations 4.40 , relating the nodal displacement vector to the eight independent constants, is so badly conditioned that an inverse (i.e. $\underset{\sim}{C}^{-1}$) was not possible. This inverse is vital for the calculation of the element stiffness matrix (see equation 4.1), and hence tha approach was abandoned.

It is for this reason the idea of dividing the 'trapezoidal' element into two 'triangular' sub-regions (see section 4.2) arose. Although this sub-division led to more complex integration terms, when calculating the stiffness matrix, it made the two 'triangular' sub-elements easier to combine, from a computing aspect, with constant strain triangular elements[4] when analysing fracture problems.

4.4.2 'Triangular' Element II*

An attempt will now be made to derive displacement shape functions for the element shown in figure 4.5 from approximations made on the crack-tip equations 2.9 and 2.11 for mode 1 and mode 2 conditions respectively. If the trigonometric terms in equations 2.9 are expressed in terms of polynomial expansions :-

$$\sin\theta = \theta - \frac{\theta^3}{3!} + \frac{\theta^5}{5!} - \cdots\cdots\cdots$$

$$\cos\theta = 1 - \frac{\theta^2}{2!} + \frac{\theta^4}{4!} - \cdots\cdots\cdots$$

it can be shown that , ignoring higher powers of θ, for mode 1 conditions we may write,

$$u = (b_1 + b_2\,\theta^2)\; r^{\frac{1}{2}}$$

$$v = (b_3 + b_4\,\theta^2)\;\theta\; r^{\frac{1}{2}} \qquad (4.42)$$

However, it is found that these equations lead to a singular $\underset{\sim}{C}$ matrix (see equation 4.29) .

Similarly for mode 2 conditions we may write,

$$u = (c_1 + c_2 \theta^2)\ \theta\ r^{\frac{1}{2}}$$

$$v = (c_3 + c_4 \theta^2)\ r^{\frac{1}{2}} \qquad (4.43)$$

Again, the $\underset{\sim}{C}$ matrix based on these shape functions is singular. One possibility emerges, however, and the following functions are considered :-

$$u = (a_1 + a_2 \theta^2)\ r^{\frac{1}{2}}$$

$$v = (a_3 + a_4 \theta^2)\ r^{\frac{1}{2}} \qquad (4.44)$$

The corresponding strain components are :-

$$\epsilon_r = \frac{1}{2}\, r^{-\frac{1}{2}}\ (a_1 + a_2 \theta^2)$$

$$\epsilon_\theta = r^{-\frac{1}{2}}\ (a_1 + a_2 \theta^2 + 2 a_4 \theta) \qquad (4.45)$$

$$\gamma_{r\theta} = \frac{1}{2}\, r^{-\frac{1}{2}}\ (4 a_2 \theta - a_3 - a_4 \theta^2)$$

It is found, as will be seen in the next section, that element II* based on equations 4.44 lead to less satisfactory results for displacements and unsatisfactory results for stresses when compared to those obtained using element II .

4.5 Problems Considered and Discussion of the Results

In this section an assessment will be made on the effectiveness of the elements developed in this chapter, namely I, II and II*, by analysing two problems for which exact solutions are available. Also, a comparison will be made between the results obtained here and those obtained by other authers[19,21].

In the two examples solved, a semi-infinite crack in an infinite plane was analysed by considering a finite circular region of radius 30.25 (see figure 4.6) centred at the crack-tip. In the first problem, the outer boundaries of the body were subjected to forces corresponding to the opening mode 1 conditions. This was done by imposing the displacements obtained from equations 2.9 at these boundaries. Only one half of the body, i.e. $\theta = 0$ to $\theta = \pi$, was considered, and this was divided into 11 annular rings as shown in figures 4.6 and 4.7 . These rings described radii :-

$$0.5 \ , \ 1.0 \ , \ 1.625 \ , \ 1.5^2 \ , \ 2.0^2 \ , \ 2.5^2 \ , \ \ldots\ldots\ldots \ , \ 5.5^2 \ .$$

This was done so that direct comparison with results obtained in reference 21 can be made. The displacements as calculated from equations 2.9 were imposed at the boundaries $\theta = 0$, $\theta = \pi$ and $r = 30.25$. The crack opening deformation of the body under these conditions are shown in figure 4.8 .

In order to demonstrate the convergence characteristics of the results, several solutions were obtained for different number of elements, namely 2 , 4 , 6 , 8 , 10 and 12 , in the circumferential direction. In all these meshes triangular elements II, of radius 0.5 , were used at the crack-tip. These were surrounded by trapezoidal elements I covering the remainder of the body. The body was considered under plane stress conditions with $E = 200$, $\nu = 0.3$ and $t = 1.0$.

The results obtained for this problem are shown in figures 4.10 - 4.19 . In figures 4.10 and 4.11 , convergence curves for the displacements and stresses at $r = 0.5$ and $\theta = 90^{\circ}$, on the boundary of the triangular element II are prepared. The exact results using equations 2.8 and 2.9 are also shown. It is seen that the v-displacement exhibits faster convergence to more accurate values than that for the u-displacement. When (11 x 6) elements are used, the value for v is within 1% of the 'exact' solution, while that for u is 2.6% in error. However if a criterion for convergence is based on the difference between results of two successive element refinements being within 1% , then the u-displacement converges to within 1.8% of the 'exact' solution when (11 x 8) elements are used, and the v-displacement converges to within 1.8% using as few as (11 x 2) elements.

Stresses at the common interface to elements I and II, i.e. at $r = 0.5$, may be calculated using stress matrices based on either element I or II . Figure 4.11 gives convergence curves for the stresses at $r = 0.5$ and $\theta = 90^{\circ}$, calculated from a stress matrix based on element II. It can be shown that if the convergence criterion stated above is used,

the stresses σ_r and $\tau_{r\theta}$ obtained using (11 x 10) elements converge to within 2.8% of the exact solutions. However, σ_θ exhibits much slower convergence and is in 14% error when (11 x 12) elements are used.

The results obtained using a stress matrix based on element I are also shown in figure 4.11 . It is generally seen that this matrix give similar results for σ_r and $\tau_{r\theta}$ and improved results for σ_θ . A nearly converged value for θ (within 6.5% of the 'exact' solution) is obtained using (11 x 12) elements. The percentage error in u , v , σ_r , σ_θ and $\tau_{r\theta}$ obtained using (11 x 12) elements are summarised in table 4.1 .

It is observed that the solutions obtained increase in accuracy with increasing distance from the crack-tip. In table 4.2 , the results for the five quantities at r = 2.25 and $\theta = 90^\circ$, using (11 x 12) elements are shown. It is seen that the accuracy of σ_θ is still inferior to those of the other four quantities.

The same problem was analysed by Tracey[21] using his element discussed in chapter 3 . For the results he reported, the first four rings contained 24 elements at 7.5°, while the remaining rings were divided into 12 elements at 15° intervals. He states that the mesh employed contained a total of 192 elements and 229 nodes with 410 degrees of freedom after applying the special constraints required at the tip elements. Generally, Tracey's results for U_x and U_y (in the x-y plane) at r = 0.5 were within 2% of the 'exact' values in the range $22^\circ \leqslant \theta \leqslant 180^\circ$. For $\theta = 15^\circ$,however, the results were 5% in error. In the present work, although a coarser mesh was used (132 elements, 156 nodes and 312 degrees of freedom), the results for the

displacements were nowhere more than 1.5% in error. While the present results for the stresses had a maximum error of 6.5% , Tracey reports a maximum error in the stresses of 4% . It will be shown later that the accuracy of the results for the stresses obtained here will be further improved when calculated at the mid-points of the outer boundaries of the triangular tip elements.

Wilson[19] analysed a similar problem employing his triangular element, similar to element II here, at the crack-tip surrounded by constant strain triangular elements[4] . The crack-tip elements had a radius of one half the radius of the body. When 18 singular elements were used together with an unspecified number of constant strain elements covering the remainder of the body, results within approximately 3% for displacements at the boundary of the tip elements were obtained. The author[19] also demonstrated that when the whole body was represented by constant strain elements, the errors were as high as 21% .

In figures 4.12 and 4.13 , the nodal displacements u and v at the boundary of the triangular elements II , i.e. at r = 0.5 , are shown. It is seen that, irrespective of the position of the node, the accuracy of the results is maintained on the whole boundary. The results obtained, when the triangular elements II are replaced by elements II* are also shown. It is seen that these elements lead to less accurate results, the errors being more significant for the u-displacements.

Figures 4.14 - 4.16 give the results for the stresses at the same boundary, i.e. at r = 0.5 . It was found that the stresses obtained when

elements II* are employed were rather inaccurate and, therefore, were omitted from the figures. Stresses calculated at the mid-points of the boundary of elements II are also shown. These exhibit appreciable improvements in the results, especially for σ_θ whose accuracy is found to be inferior to those of σ_r and $\tau_{r\theta}$ when calculated at the nodes.

When calculating stresses at the nodes, with the exception of the nodal points at the boundary of the structure, four stress values are obtained from the four elements jointed at that node. The results shown in figures 4.14 - 4.16 were obtained by simple averaging. In order to show the degree of discontinuity of the stresses, the individual values at the boundary $r = 0.5$ are plotted in figures 4.17 - 4.19 . It is interesting to note that the values for σ_θ , whose accuracy was found to be inferior to those of σ_r and $\tau_{r\theta}$, exhibit the highest degree of discontinuity. It can generally be concluded that the discontinuities in σ_r and $\tau_{r\theta}$ decrease as θ increases, i.e. as the angular distance from the crack surface increases. Figures 4.20 - 4.22 show slightly lower discontinuities in the stresses at the boundary $r = 2.25$. Discontinuity of stresses at the nodes is a common feature to most finite element models and it is generally accepted that more accurate results are obtained when the stresses are calculated at the interior of the elements.

In figures 4.23 - 4.25 the nodal stresses as calculated from a stress matrix based on element I are given as a function of r. The results demonstrate the rapid increase in the stresses as the crack-tip is approached. As pointed out earlier, the accuracy of the results increase with increasing distance r .

From the above discussion it can generally be concluded that in the present work, using smaller number of elements than those employed by Tracey[21] and Wilson[19] , more accurate results for displacements and stresses (within 3% , with the exception of σ_θ) near the crack-tip, were obtained for mode 1 conditions. Improved accuracy for σ_θ was obtained from a stress matrix based on element I .

In the second problem the outer boundaries of the body were subjected to forces corresponding to the sliding mode 2 conditions. Again, only one half of the body , i.e. $\theta = 0$ to $\theta = \pi$, was considered and the displacements as calculated from equations 2.11 were imposed at the boundaries $\theta = 0$, $\theta = \pi$ and $r = 30.25$. The crack sliding and general deformation of the body under these conditions are shown in figure 4.9 . The results obtained using the same finite element representations employed in the first problem are given in figures 4.26 - 4.38 . It can be seen that the results are generally of the same order of accuracy as those obtained for mode 1 conditions. However, it is interesting to note that although vanishingly smaller values for the u-displacements are obtained, when compared to those for mode 1 conditions, the results appear to have a higher degree of accuracy. Also, when (11 x 12) elements are used, the error in σ_θ at $r = 0.5$ and $\theta = 90^\circ$ is within 2.3% of the 'exact' value. These results are summarised in table 4.3 .

It may be concluded here that elements I and II give equally accurate results for mode 2 conditions. In particular the errors in σ_θ associated with mode 1 conditions are obviated.

4.6 Conclusions

Two elements (I and II) based on displacement functions which represent closely those associated with the singular character of the strains near the crack-tip were presented. When employing these elements, small meshes can be used to obtain accurate results for displacements and stresses, and hence for stress intensity factors, at relatively large distances from the crack-tip. Somewhat larger meshes, (11 x 12) elements, lead to results, for the immediate vicinity of the tip, within 3% of 'exact' solutions. The elements work equally well whether mode 1 or mode 2 situations are considered.

It is interesting to note that the strains for element I (equations 4.26 - 4.28) and those for element II (equations 4.37 - 4.39) vary in an identical manner, with respect to r and θ , at the common interface. Although the displacements for the two elements (equations 4.24 , 4.25 and 4.35 , 4.36) are continuous only at the nodal points, it is argued that, excepting the rigid body terms, as the radius of the tip elements decrease indefinitely, continuity at the interface will be approached in the limit. The inclusion of the rigid body terms in the displacement functions of element I may be partly responsible for the generally high degree of accuracy obtained for the results at relatively large distances from the crack-tip.

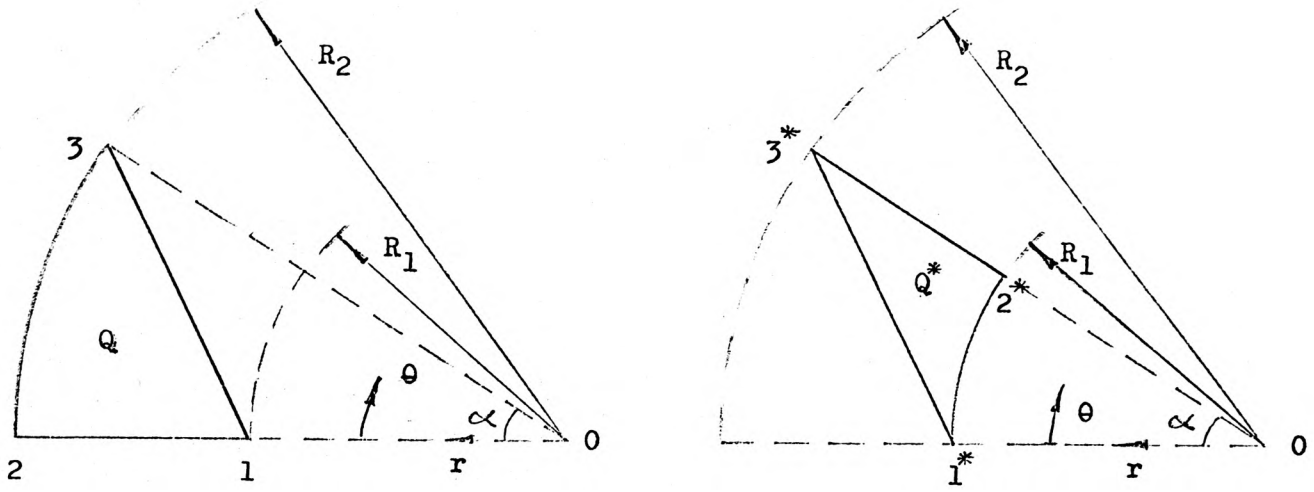

Figure 4.1 Triangular sub-elements Q and Q^*

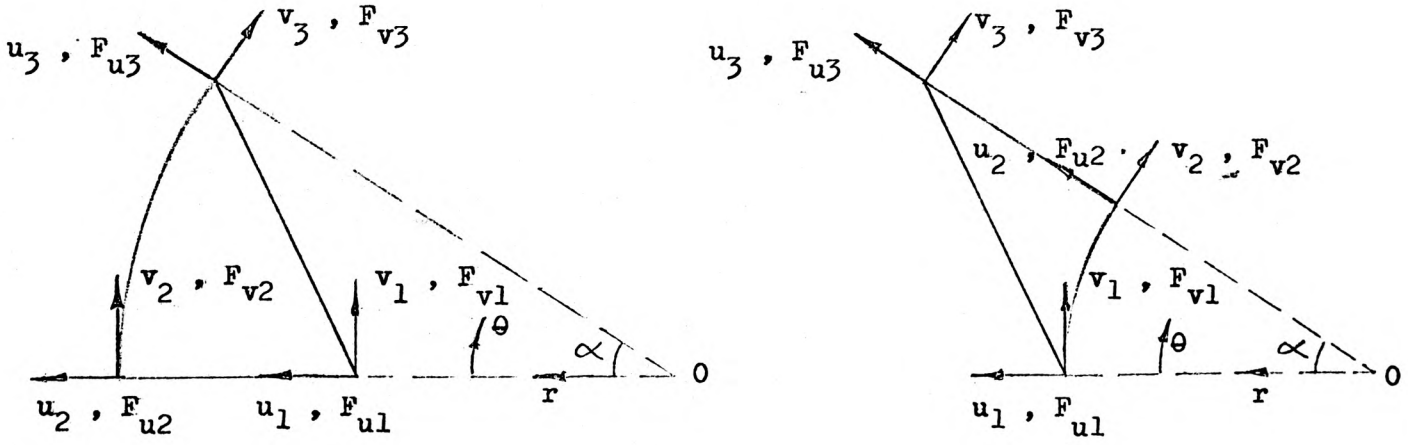

Figure 4.2 Positive directions of displacements and forces

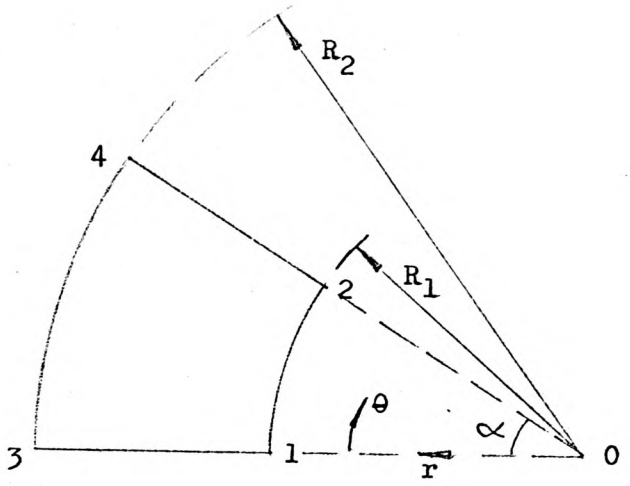

Figure 4.3 Trapezoidal element (I) for analysis near crack-tip

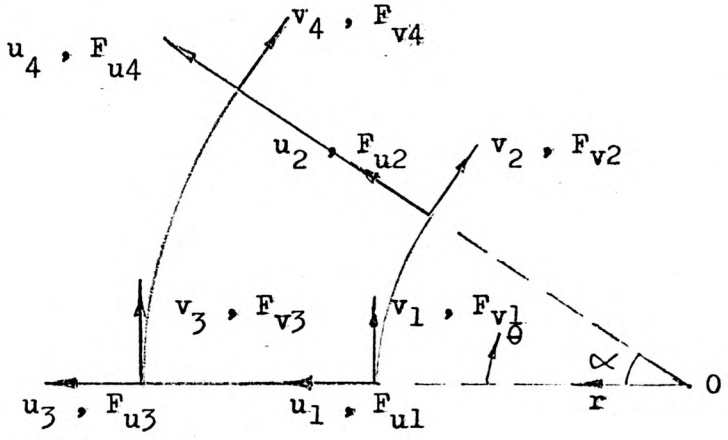

Figure 4.4 Positive directions of displacements and forces

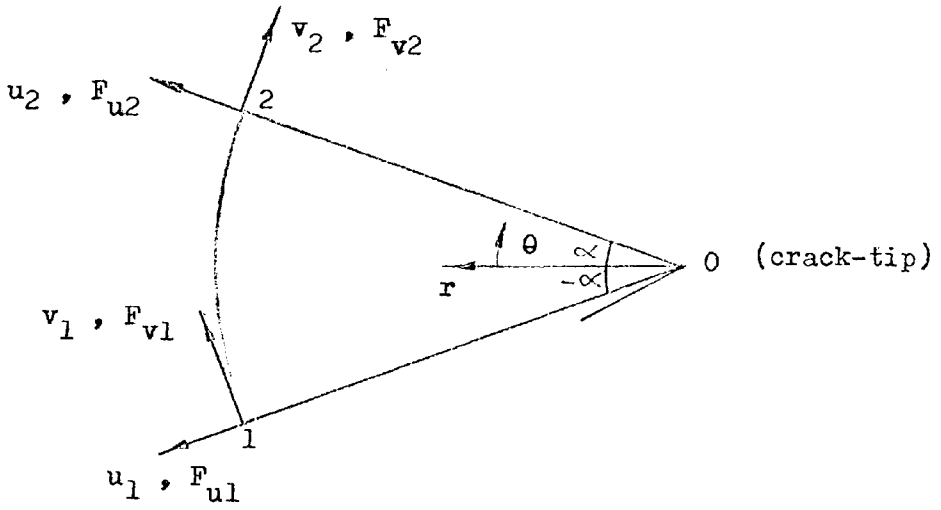

Figure 4.5 Crack-tip element (II)

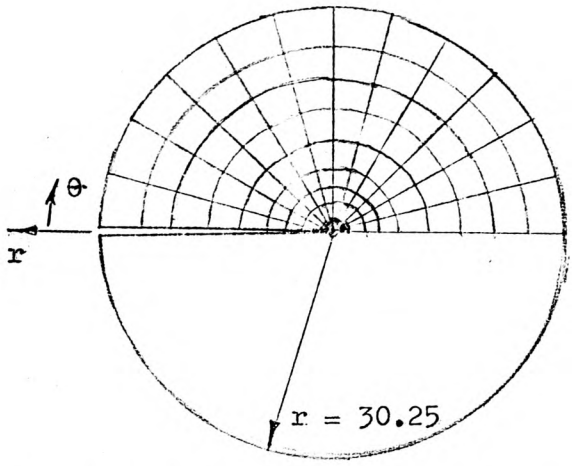

Figure 4.6 Circular body containing a radial crack extending from the centre to its outer boundary

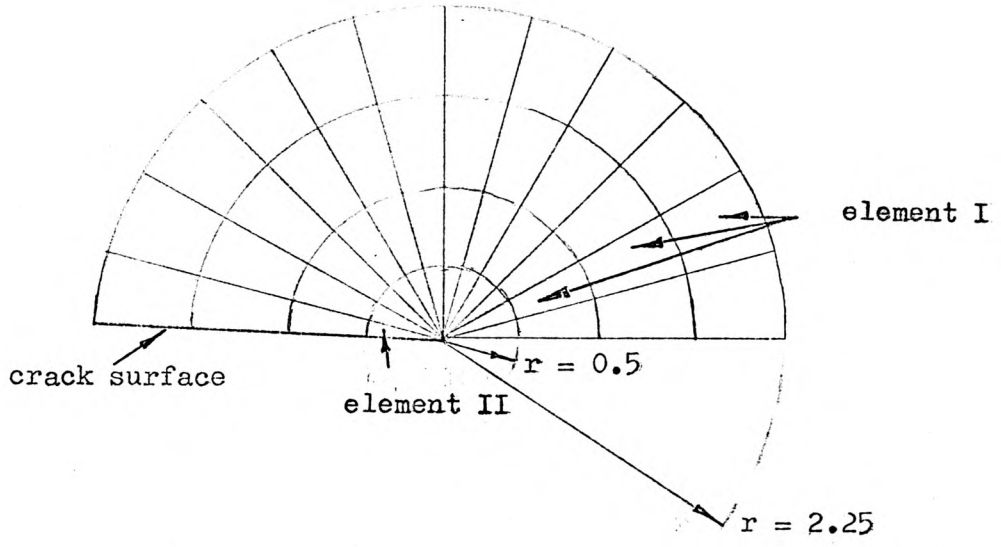

Figure 4.7 Expanded view at the crack-tip region

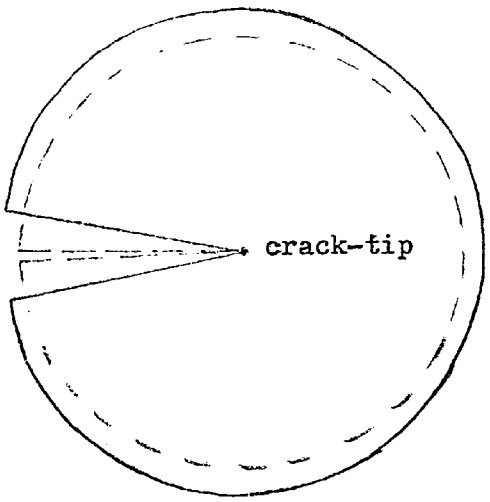

Figure 4.8 Boundary deformation for body subjected to mode 1 tractions (equations 2.9)

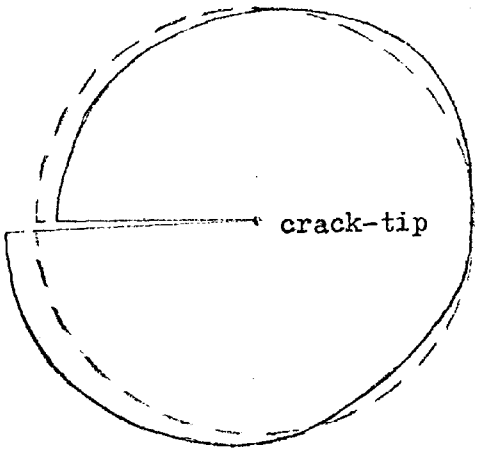

Figure 4.9 Boundary deformation for body subjected to mode 2 tractions (equations 2.11)

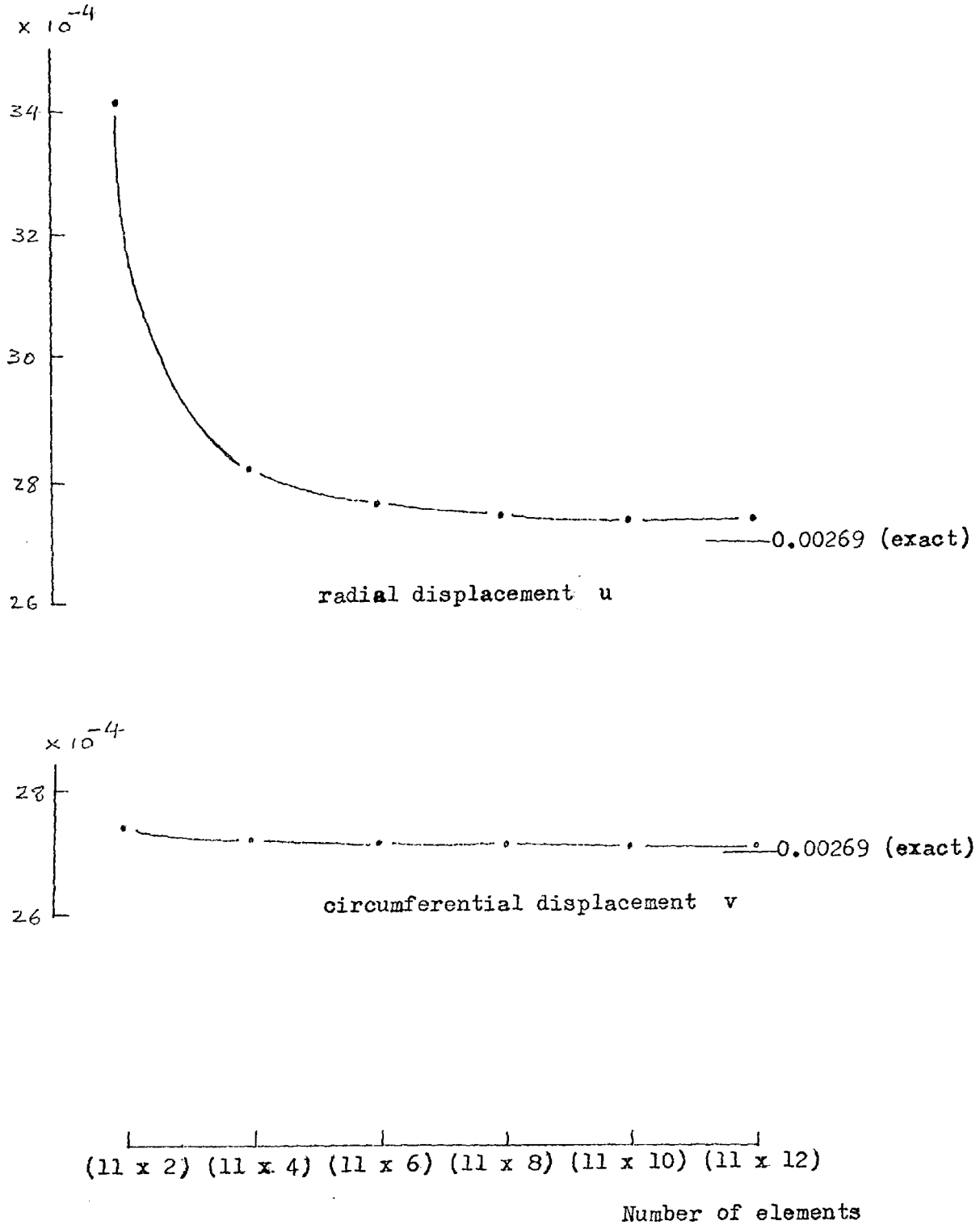

Figure 4.10 Convergence curves for displacements at

($r = 0.5$, $\theta = 90^{\circ}$)

Mode 1 - Plane stress

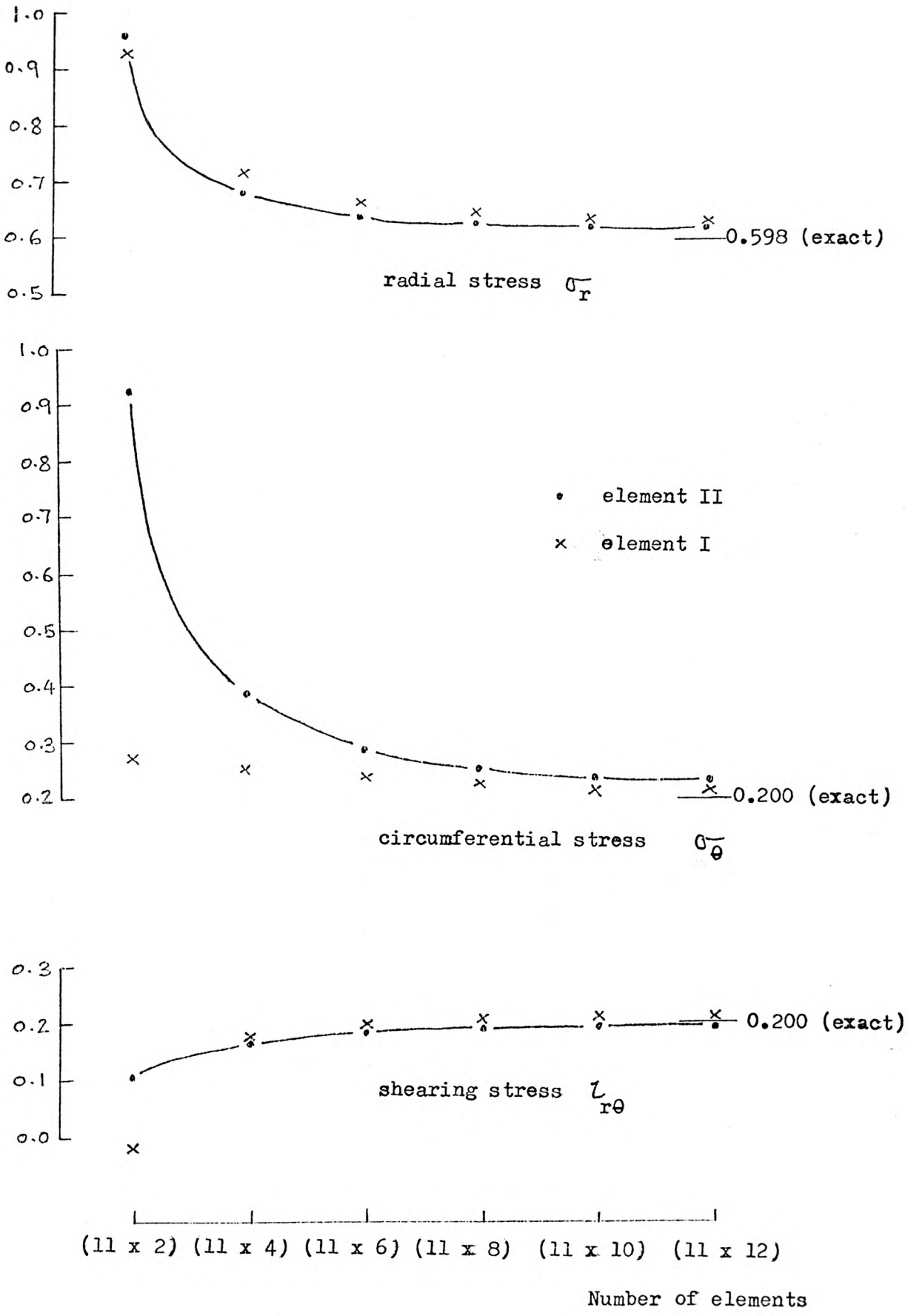

Figure 4.11 Convergence curves for stresses at

($r = 0.5$, $\theta = 90^\circ$)

Mode 1 - Plane stress

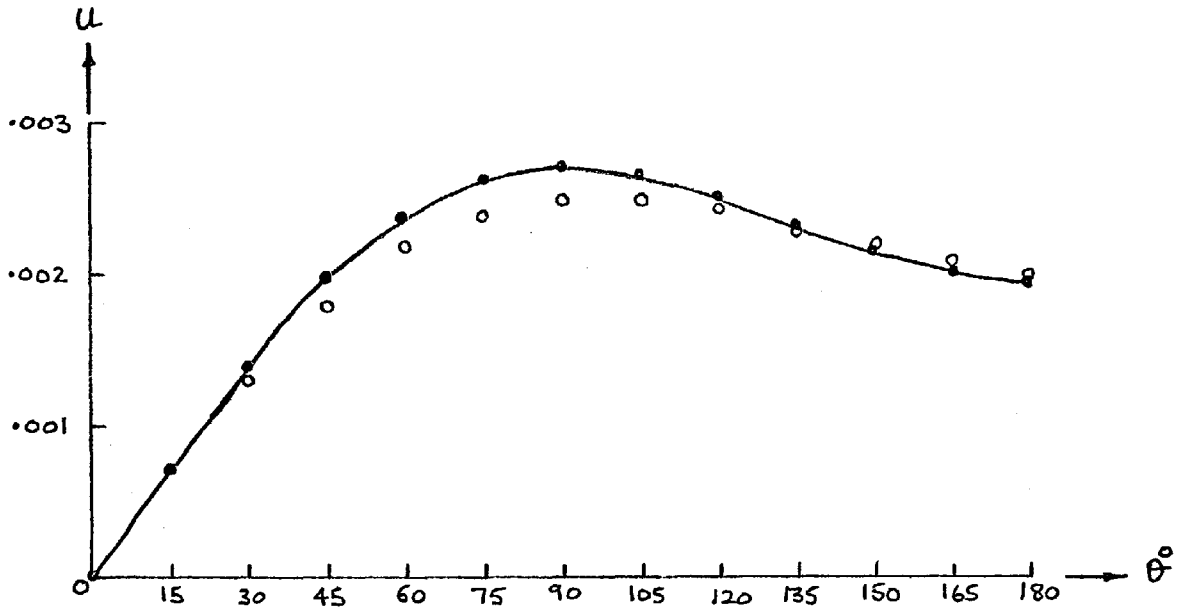

Figure 4.12 Distribution of radial displacements at r = 0.5

Mode 1 - plane stress

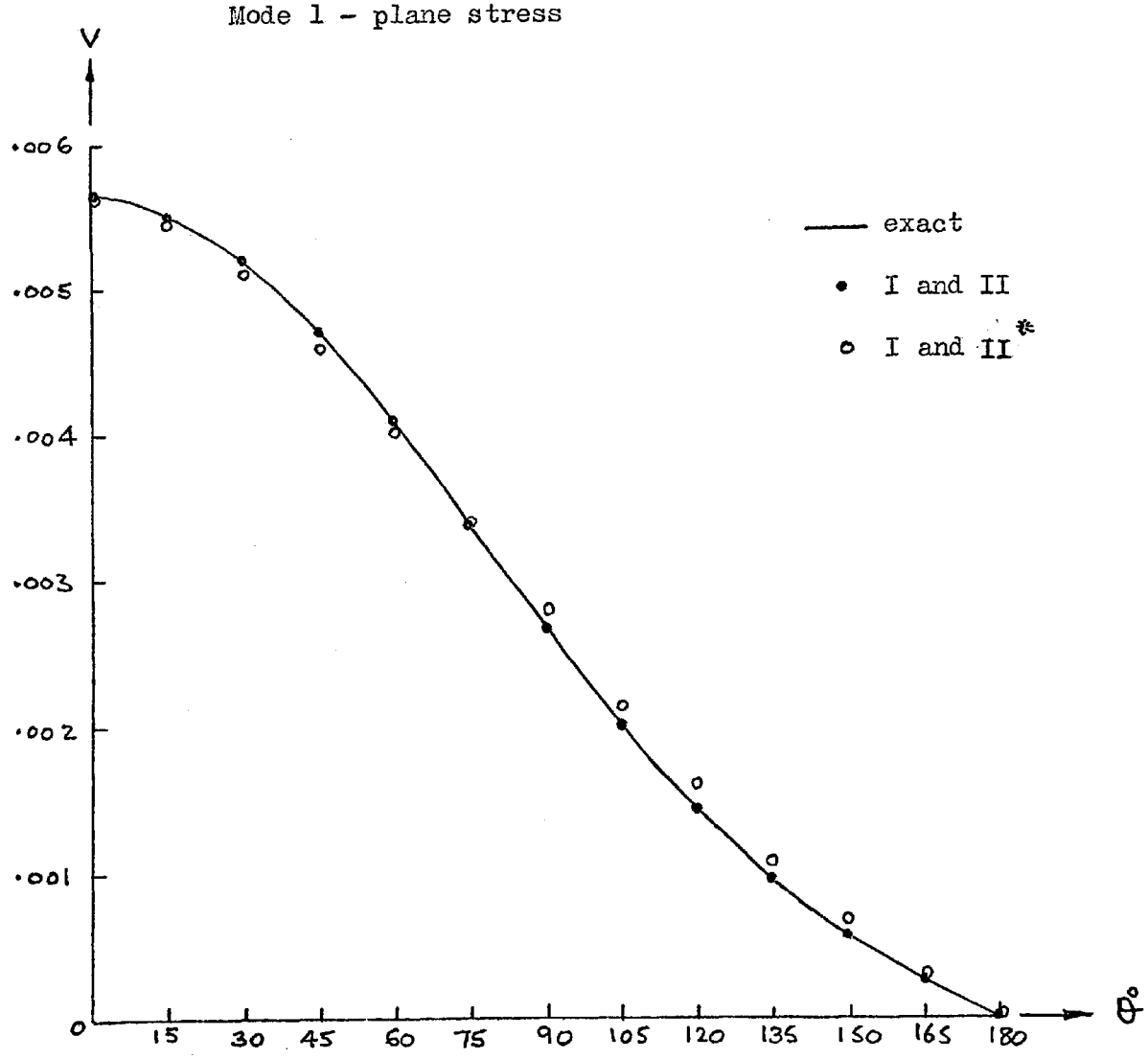

Figure 4.13 Distribution of circumferential displacements at r = 0.5

Mode 1 - plane stress

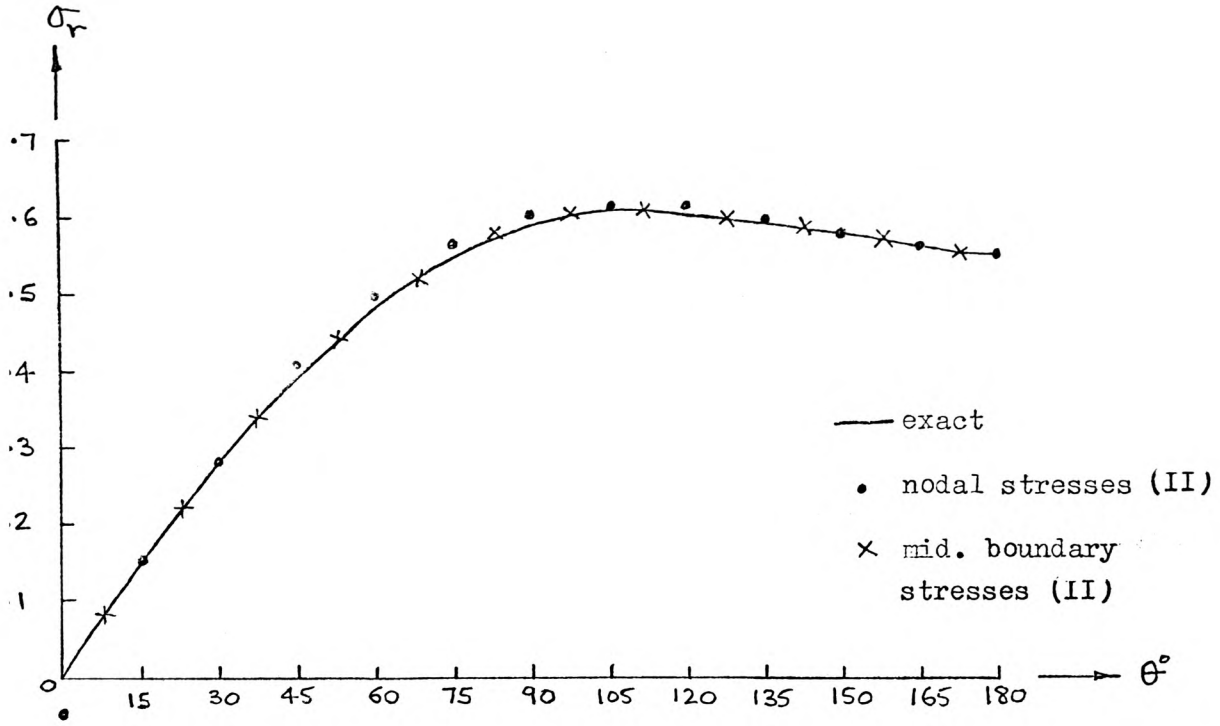

Figure 4.14 Distribution of radial stress at r = 0.5

Mode 1 – plane stress

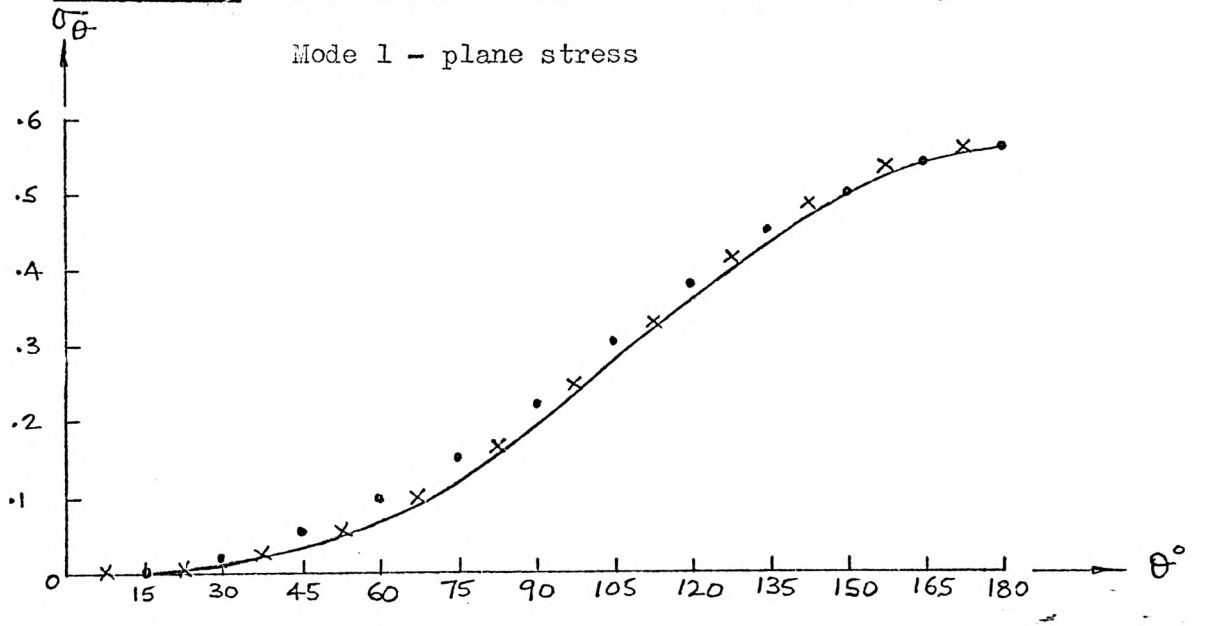

Figure 4.15 Distribution of circumferential stress at r = 0.5

Mode 1 – plane stress

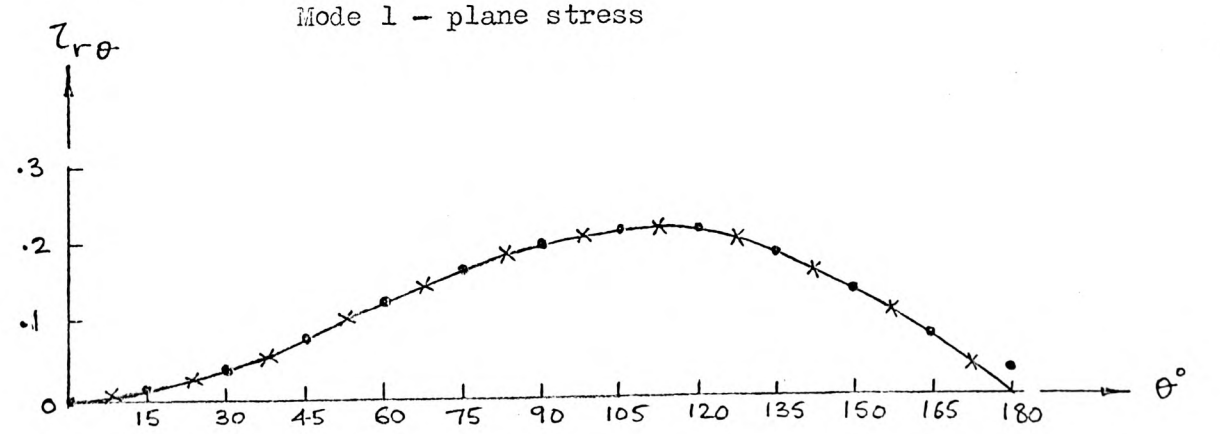

Figure 4.16 Distribution of shearing stress at r = 0.5

Mode 1 – plane stress

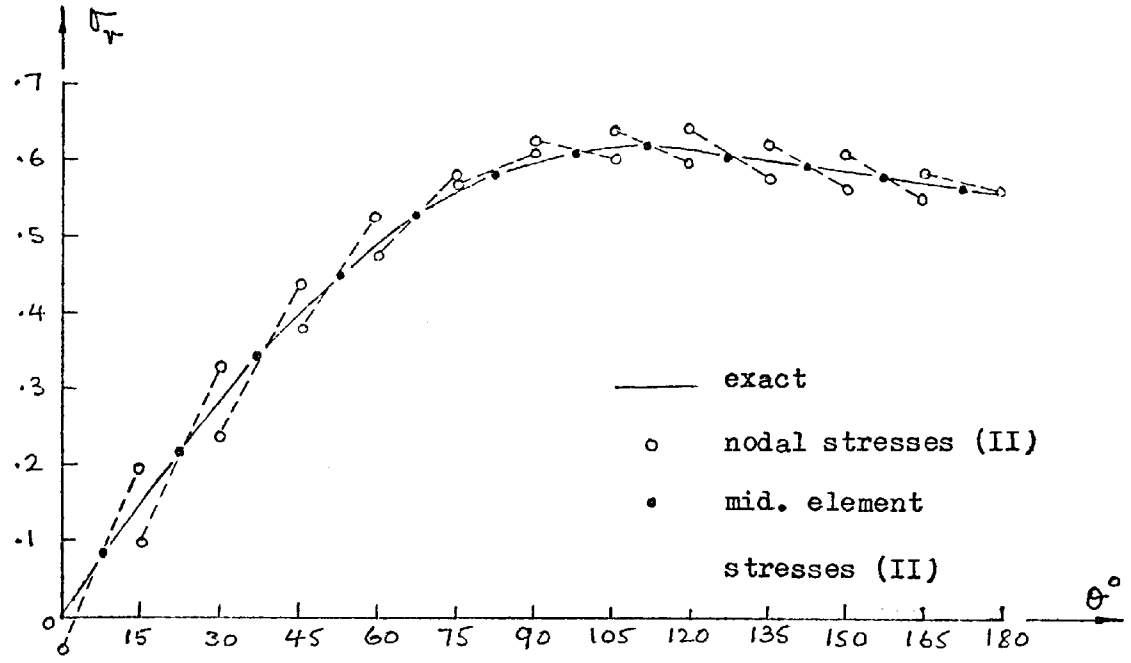

Figure 4.17 Distribution of radial stresses at r = 0.5

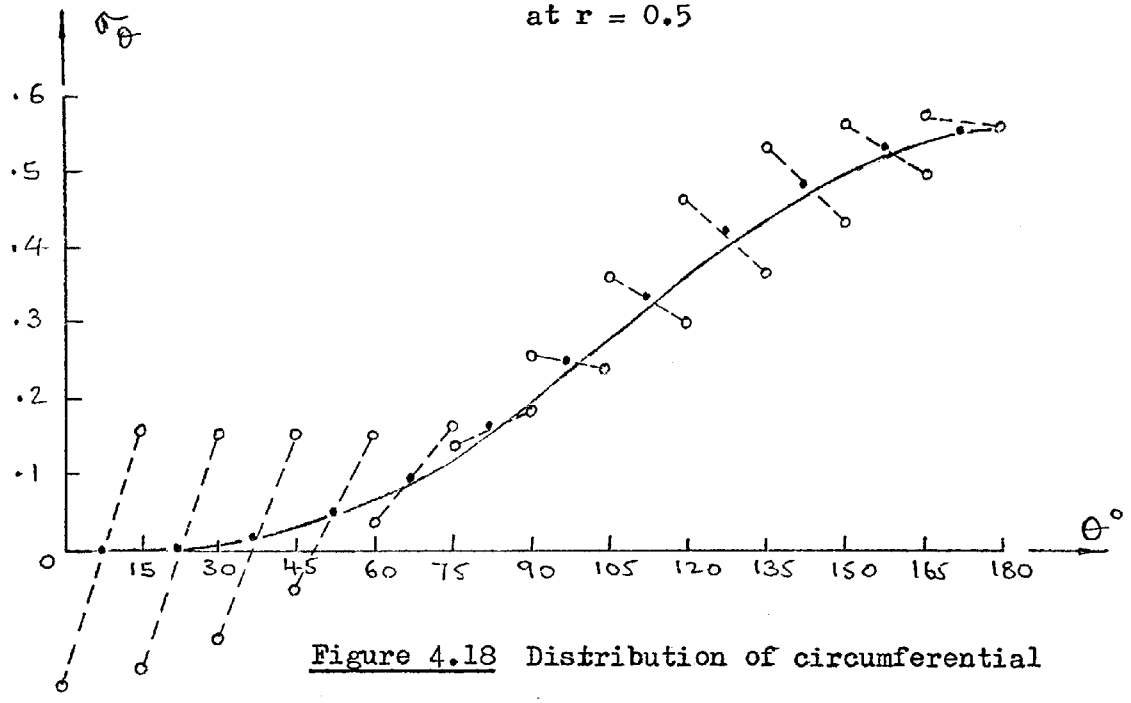

Figure 4.18 Distribution of circumferential stresses at r = 0.5

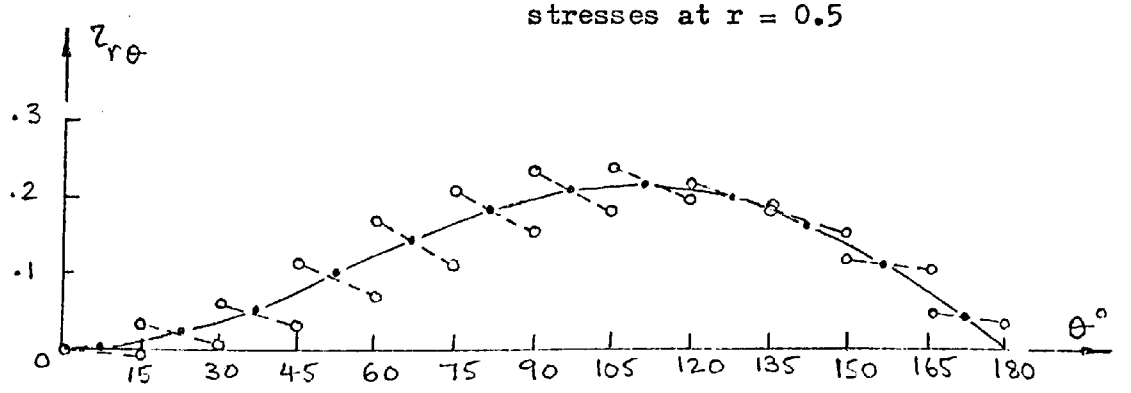

Figure 4.19 Distribution of shearing stresses at r = 0.5

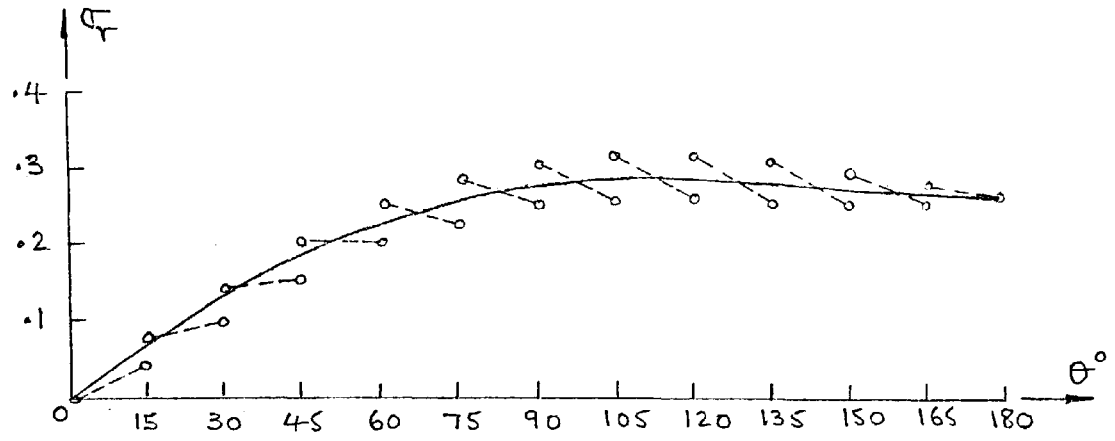

Figure 4.20 Distribution of radial stresses

at r = 2.25

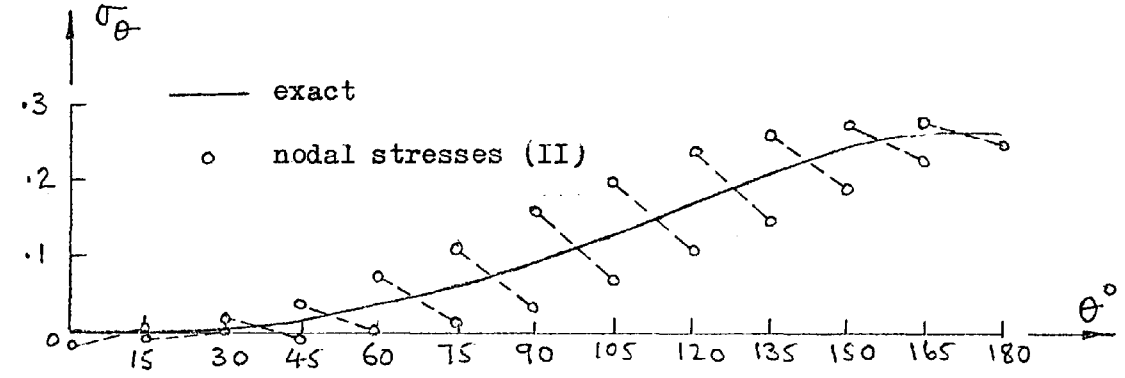

Figure 4.21 Distribution of circumferential stresses

at r = 2.25

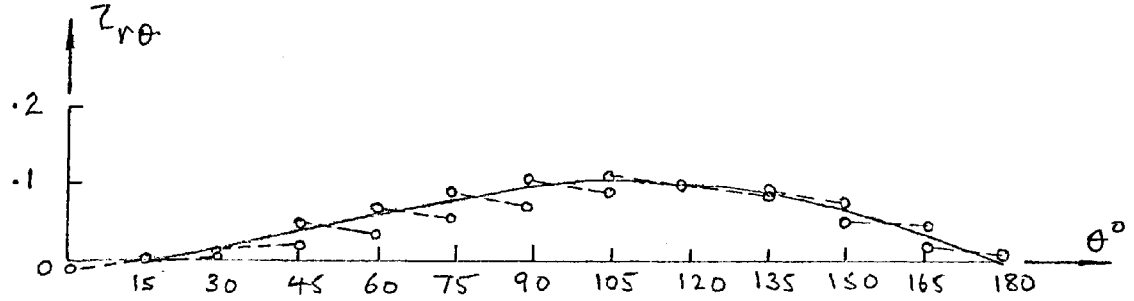

Figure 4.22 Distribution of shearing stresses

at r = 2.25

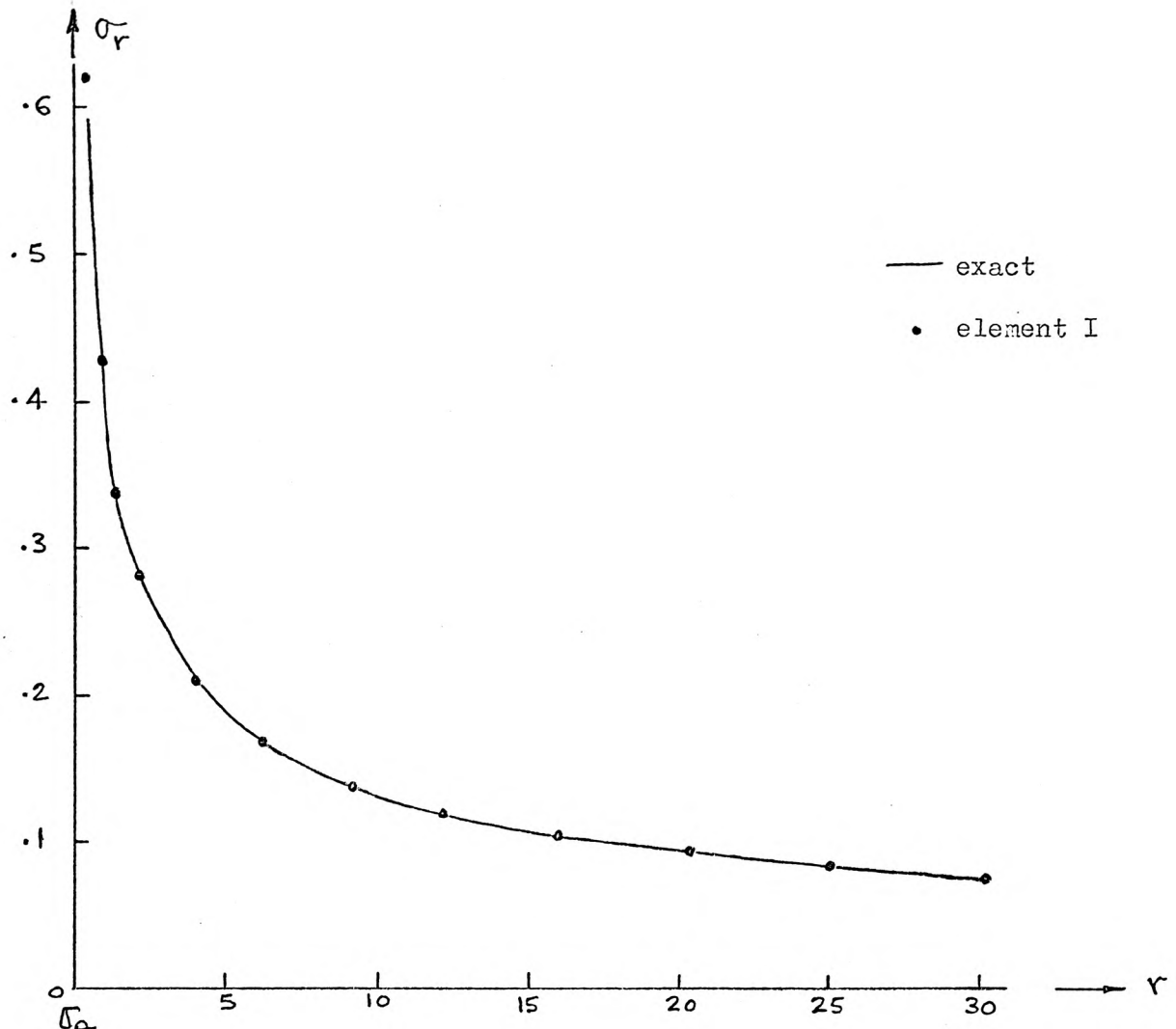

Figure 4.23 Distribution of radial stress at $\theta = 90^\circ$

Mode 1 – plane stress

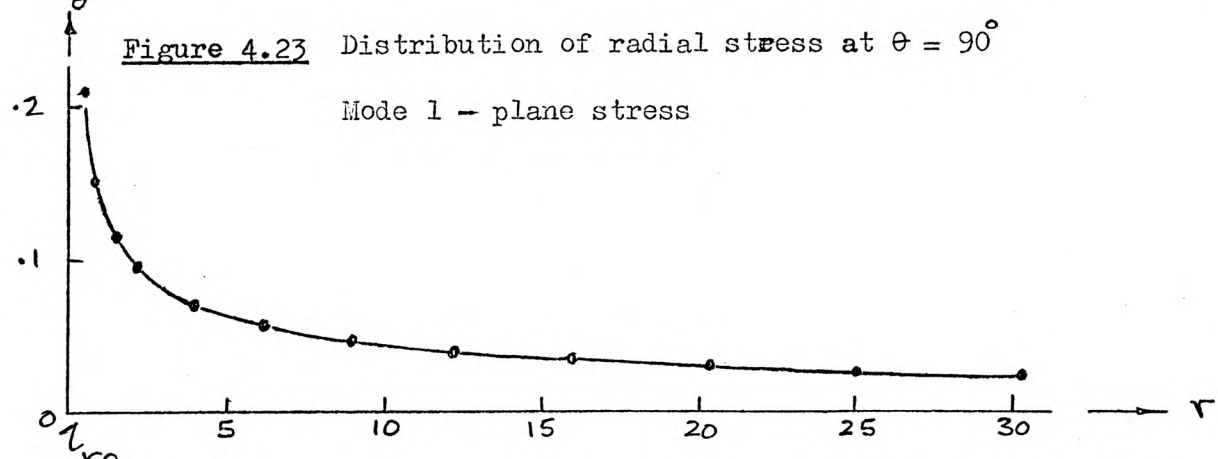

Figure 4.24 Distribution of circumferential stress at $\theta = 90^\circ$

Mode 1 - plane stress

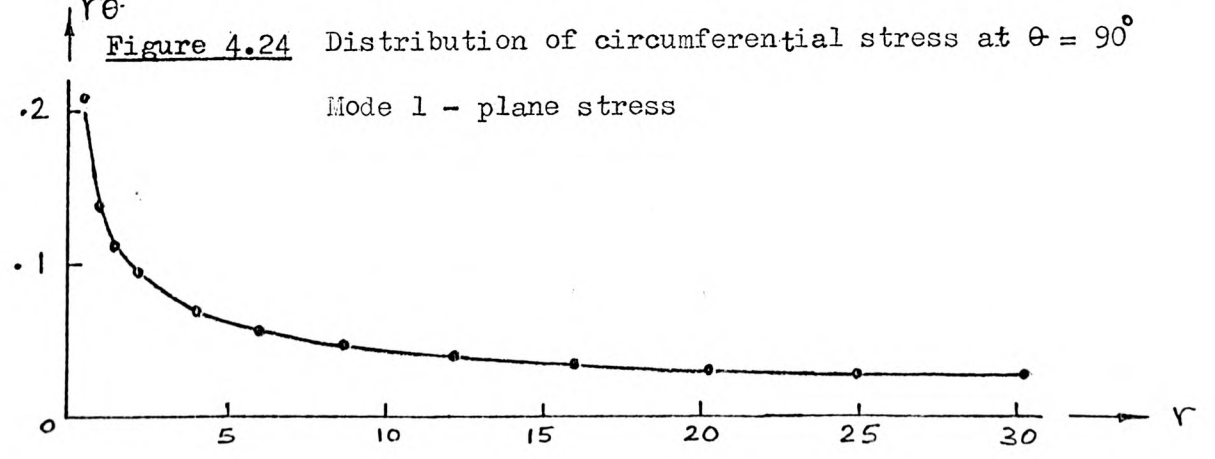

Figure 4.25 Distribution of shearing stress at $\theta = 90^\circ$

Mode 1 – plane stress

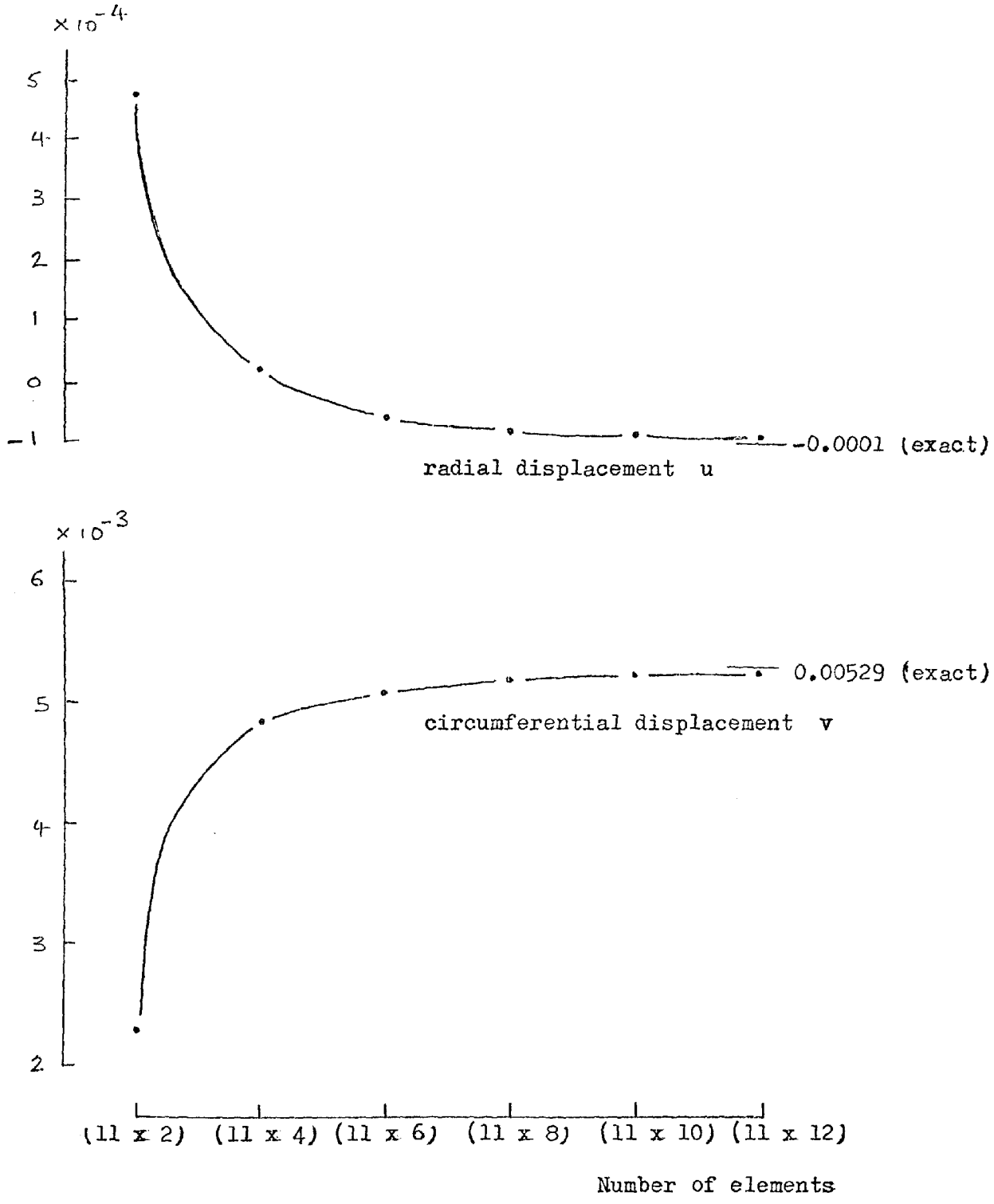

Figure 4.26 Convergence curves for displacements at ($r = 0.5$, $\theta = 90^{\circ}$)

Mode 2 - Plane stress

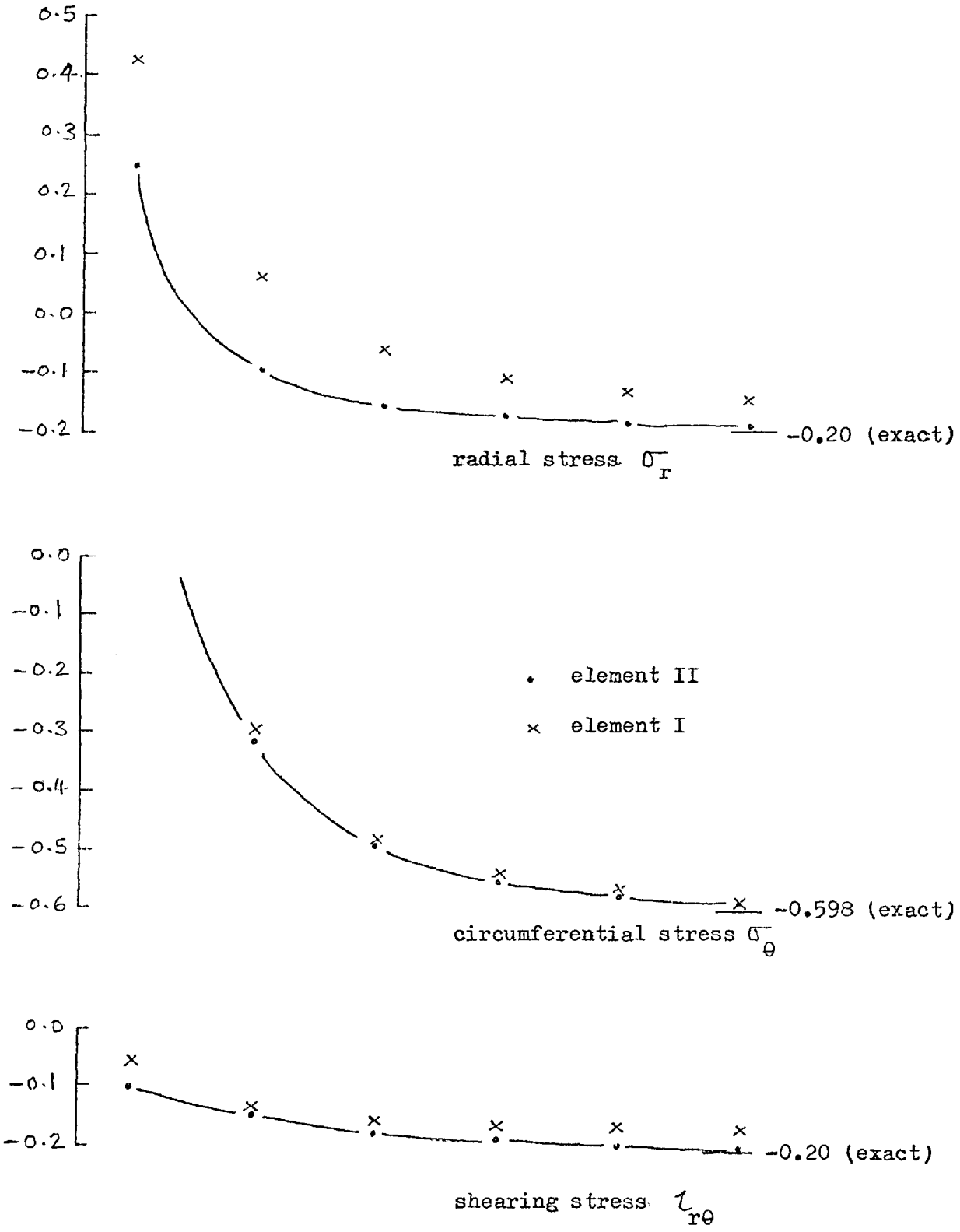

Figure 4.27 Convergence curves for stresses

at ($r = 0{,}5$, $\theta = 90^\circ$)

Mode 2 - Plane stress

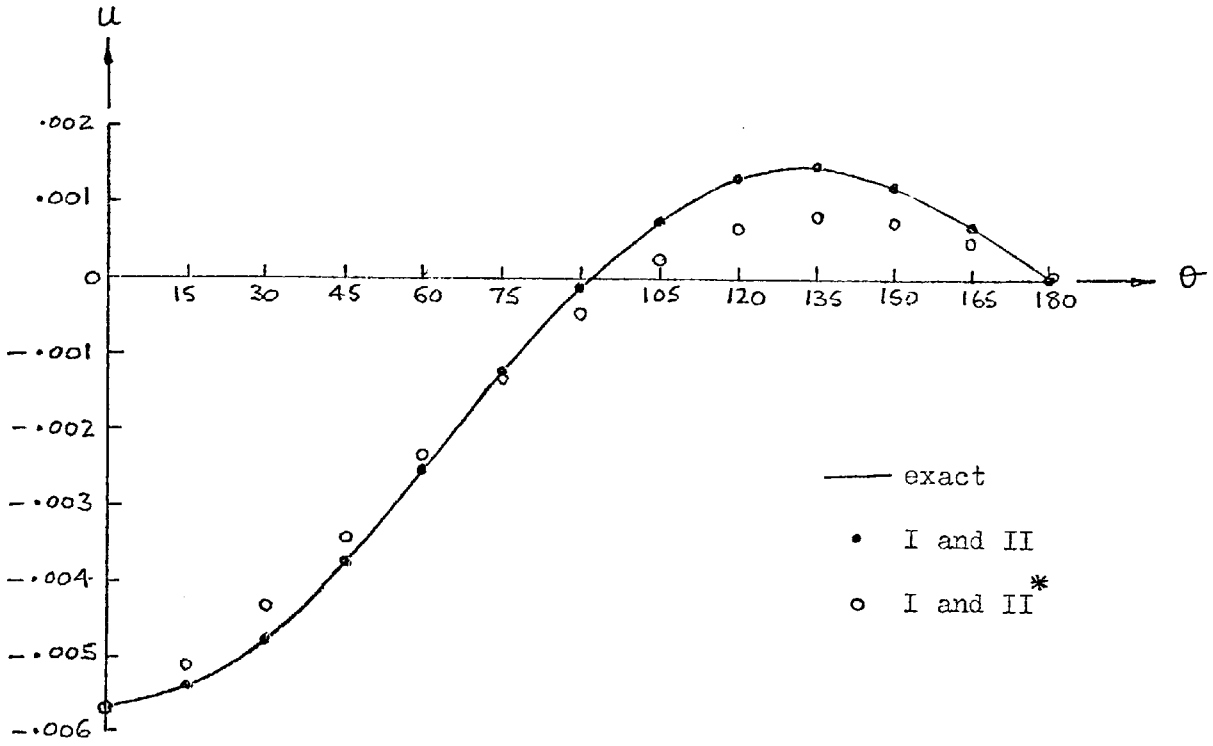

Figure 4.28 Distribution of radial displacement at r = 0.5

Mode 2 - plane stress

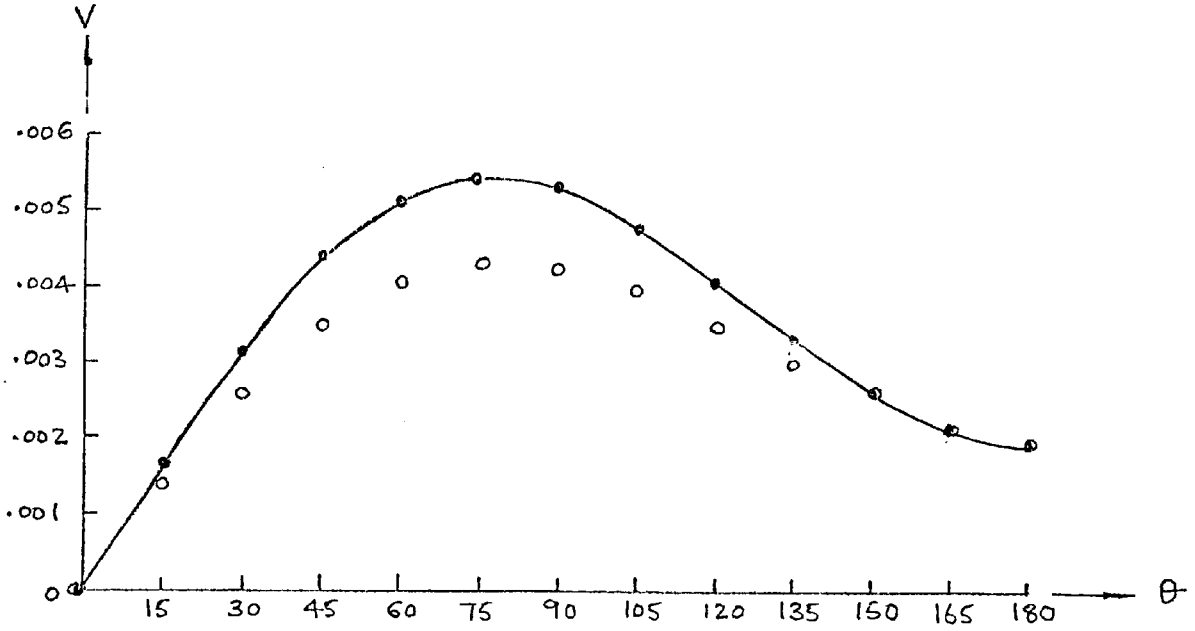

Figure 4.29 Distribution of circumferential displacement at r = 0.5

Mode 2 - plane stress

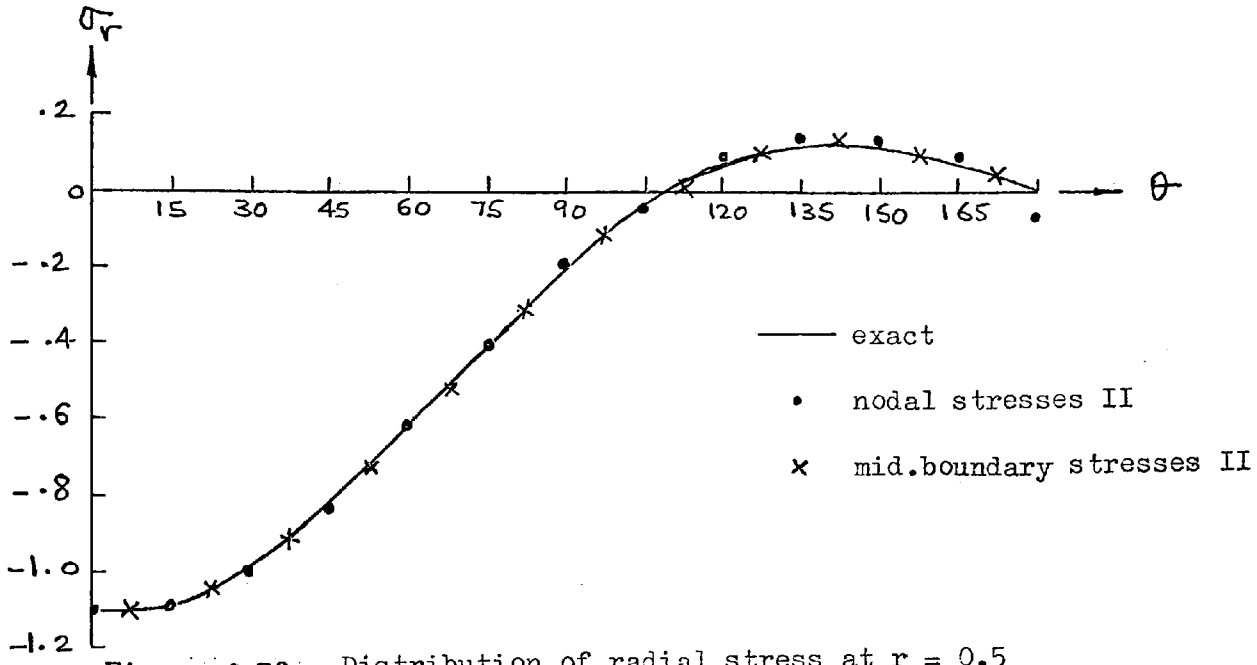

Figure 4.30 Distribution of radial stress at r = 0.5

Mode 2 - plane stress

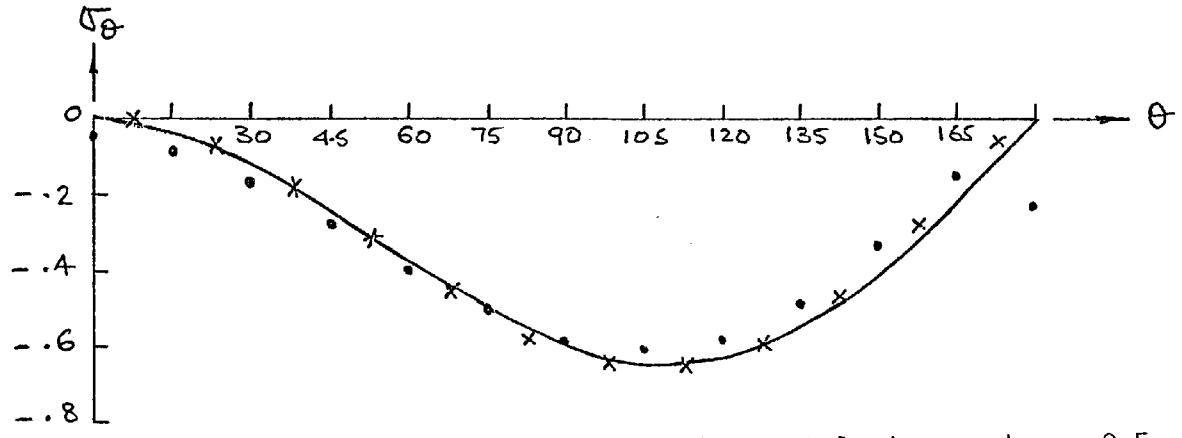

Figure 4.31 Disribution of circumferential stress at r = 0.5

Mode 2 - plane stress

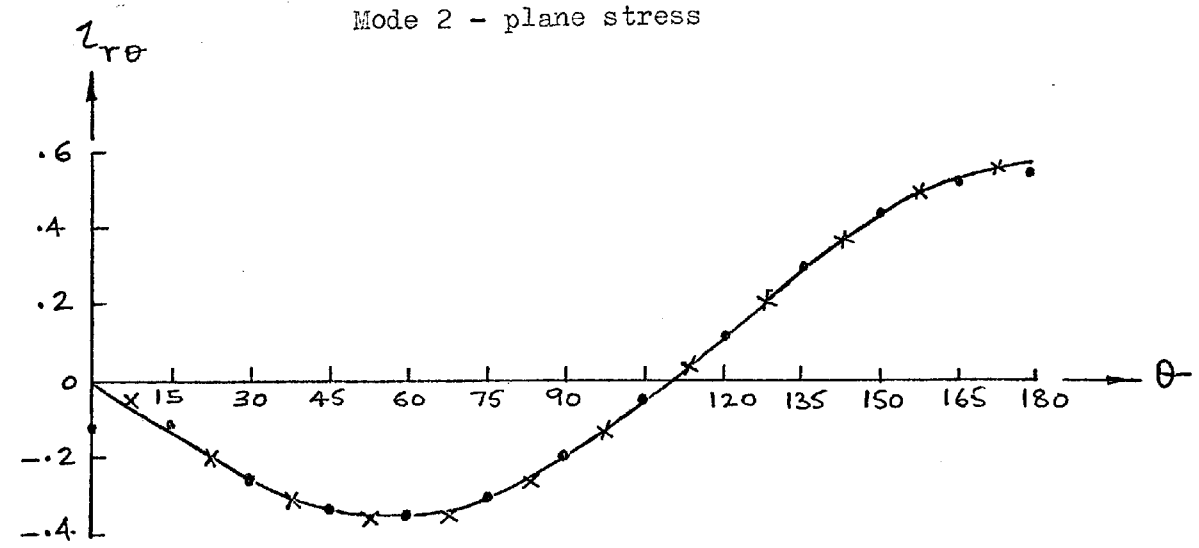

Figure 4.32 Distribution of shearing stress at r = 0.5

Mode 2 - plane stress

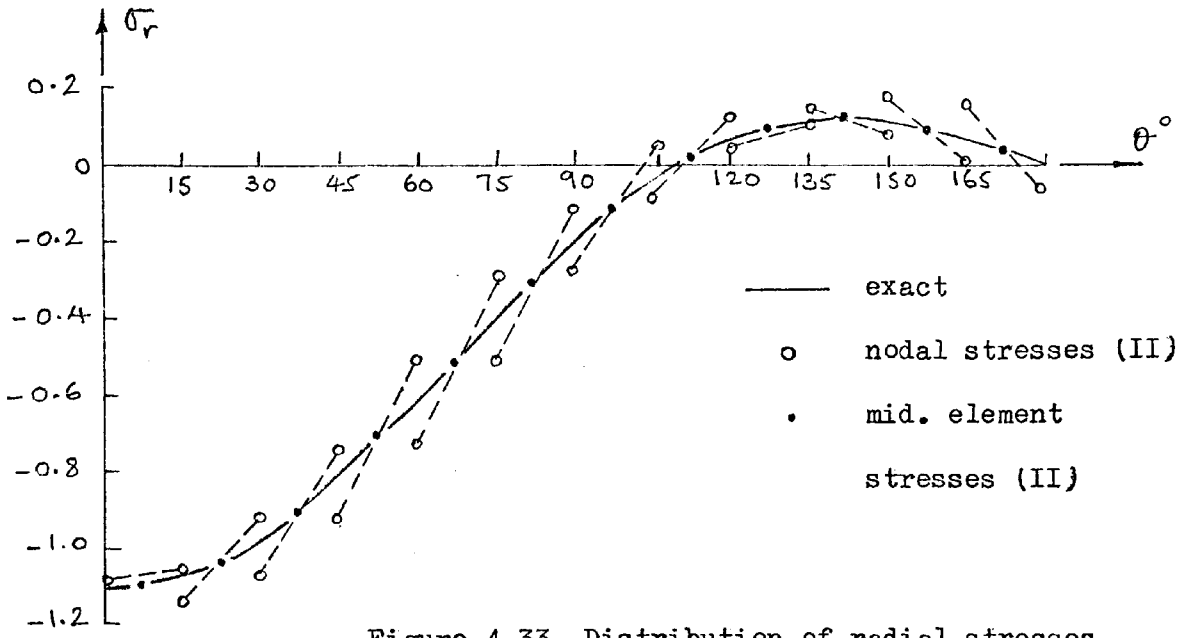

Figure 4.33 Distribution of radial stresses at r = 0.5

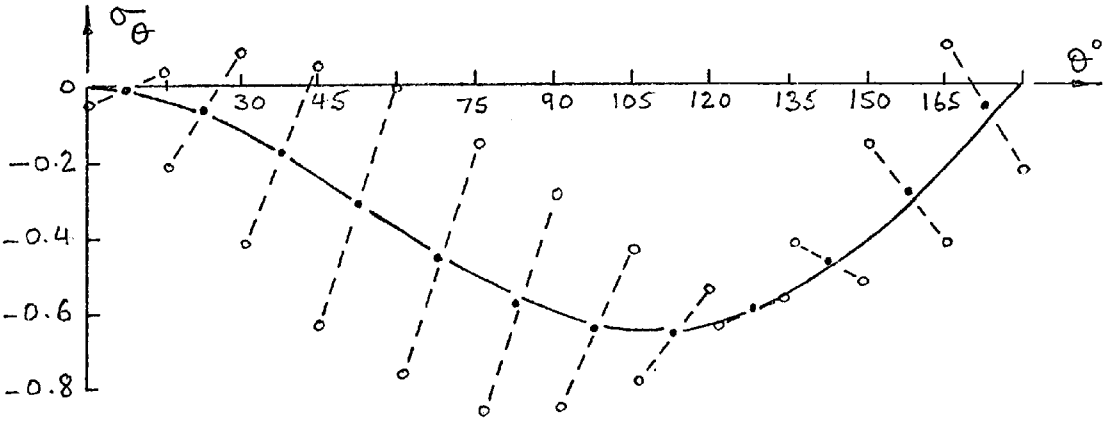

Figure 4.34 Distribution of circumferential stresses at r = 0.5

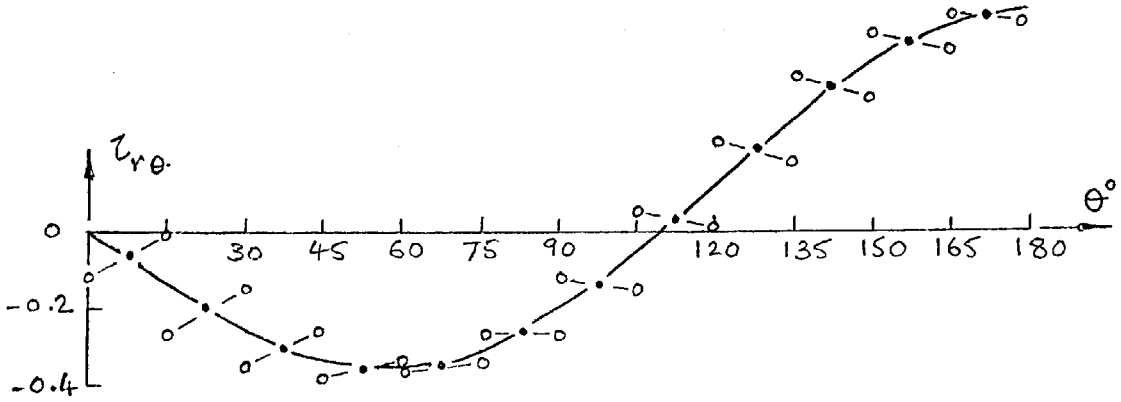

Figure 4.35 Distribution of shearing stresses at r = 0.5

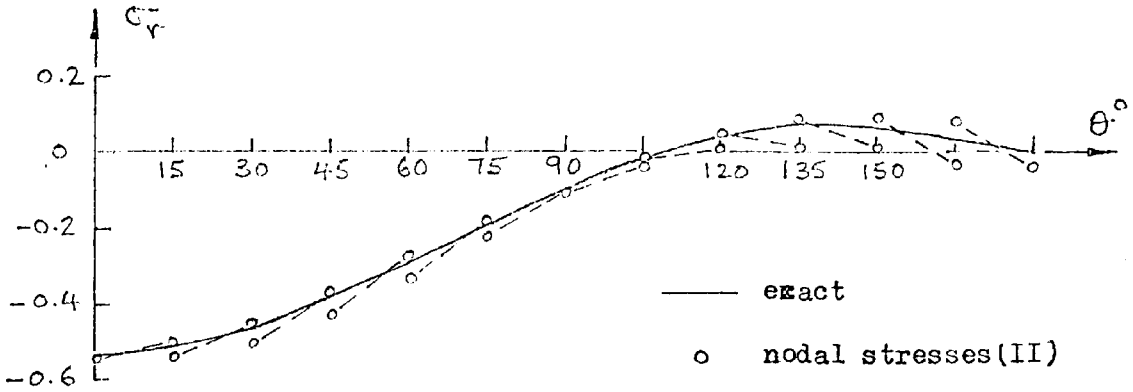

Figure 4.36 Distribution of radial stresses at r = 2.25

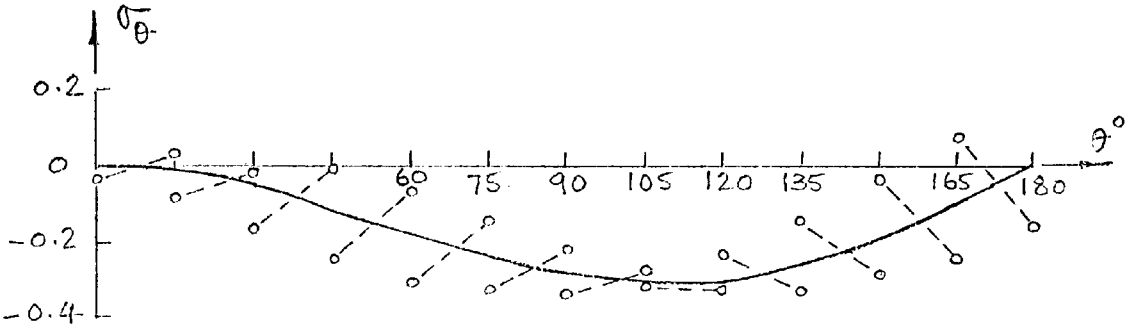

Figure 4.37 Distribution of circumferential stresses at r = 2.25

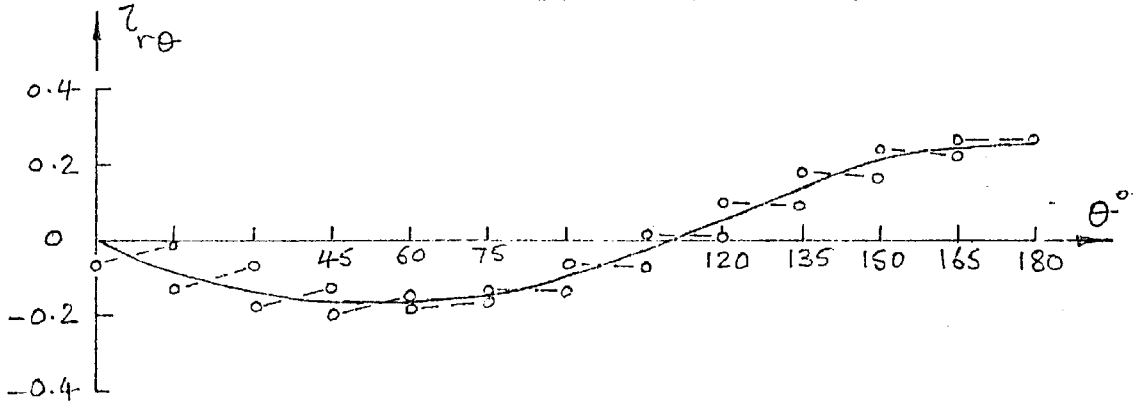

Figure 4.38 Distribution of shearing stresses at r = 2.25

	u	v	σ_r	σ_θ	$\tau_{r\theta}$
'exact'	0.00269	0.00269	0.598	0.200	0.200
(11 x 12) elements II	0.00273	0.00270	0.615	0.213	0.195
percentage error	1.5	0.4	2.8	6.5*	-2.5

* obtained from element I

Table 4.1 Displacements and stresses at r = 0.5 and $\theta = 90^\circ$

Mode 1 conditions - plane stress

	u	v	σ_r	σ_θ	$\tau_{r\theta}$
'exact'	0.00571	0.00571	0.282	0.0940	0.0940
(11 x 12) elements I	0.00576	0.00574	0.284	0.0994	0.0946
percentage error	0.9	0.4	0.7	5.7	0.6

Table 4.2 Displacements and stresses at r = 2.25 and $\theta = 90^\circ$

Mode 1 conditions - plane stress

	u	v	σ_r	σ_θ	$\tau_{r\theta}$
'exact'	-0.00010	0.00529	-0.200	-0.598	-0.200
(11 x 12) elements II	-0.00009	0.00524	-0.193	-0.584	-0.199
percentage error	-0.2	-0.9	-3.5	-2.3	-0.5

This error is relative to the maximum value of u on boundary r = 0.5

Table 4.3 Displacements and stresses at r = 0.5 and $\theta = 90^\circ$

Mode 2 conditions - plane stress

CHAPTER 5 APPLICATIONS TO MODE 1 PROBLEMS

In chapter 4 two new elements (I and II) capable of producing the singular strains associated with the crack-tip region were presented. It was shown that when using these elements in a singular field, even with coarse meshes, accurate results for displacements and stresses can be obtained. In a real situation this singular region is confined to a small area of the cracked plate surrounding the crack-tip. When analysing problems, therefore, the major part of the body must be represented by conventional finite elements. The difficulty usually encountered here is the choice of the size of the singular region. By a rule of thumb, Kobayashi et al[11] define this local region as that within a/40 from the crack-tip, where 'a' is the length of the crack.

In this chapter several problems, of the type used in fracture toughness analysis are solved. Using elements I and II in the singular region and constant strain triangular (CST) elements[4] elsewhere, the results suggest a size of the singular region of the crack-tip which is approximately half that assumed by Kobayashi et al[11]. The results also demonstrate that although acceptable values of the stress intensity factors can be obtained by the displacement extrapolation method, using a cluster of elements II around the crack-tip surrounded by CST elements, the displacement and stress fields near the crack-tip are poorly represented. The inclusion of elements I in the analysis lead to significant improvements in the results. Using these results it is possible to obtain accurate values of stress intensity factors by simple averaging around the crack-tip, thus obviating the need for an extrapolation process.

The results reported in this chapter and in all subsequent analysis employing CST elements are obtained from a programme developed by Coughlan[41] . The programme in its original form employs CST elements derived in terms of the rectangular set of co-ordinates x and y . This was adapted so that it can accommodate elements I and II developed in terms of polar co-ordinates r and θ . Because of the extensive modifications made, it was thought desirable to test the new version by first solving a problem previously analysed , in a similar manner, by Wilson[19] .

5.1 Crackline Loaded Square Plate

Several solutions for a square plate with a single edge crack of dimensions given in figure 5.1 are obtained. The plate is considered under plane strain conditions with $E = 200$, $\nu = 0.3$ and thickness $= 1.0$. Because of symmetry with respect to loading and geometry, only one half of the plate was analysed. Two finite element meshes were employed, the details of which are given below.

Coarse Mesh

The details of this mesh employed in the upper half of the plate are shown in figure 5.2 . The crack-tip at the centre of the plate is enclosed by 12 triangular tip elements II, each subtending an angle of 15° at the tip. These are surrounded by 6 layers, each containing 12 trapezoidal regions in the circumferential direction. Each of these regions is in turn subdivided into two triangular elements. The semi-circular boundaries shown described radii

$$10 , 15 , 21 , 28 , 36 , 45 , 55 .$$

This method of subdivision was used so that automatic generation of the elements and node numbering could be employed in the region within $r = 0.55\ a$, thus reducing the size of the input data significantly. The remainder of the body was divided into triangular elements as shown. The relative sizes of the elements used in this mesh are given in table 5.1 .

Here the terms 'inner' and 'outer' refer to [illegible] elements very close to tip elements II and elements away from the crack-tip respectively. This representation contained 242 elements and 147 nodal points giving a total of 294 degrees of freedom.

Fine Mesh

It will be seen in the following section that the coarse mesh just described leads to inaccurate results for displacements around the crack-tip. As CST elements are used over an area close to the tip of the crack, it was thought necessary to reduce the size of these elements so that they could more adequately represent the large stress gradients there. As before, the crack-tip is enclosed by 12 triangular elements II, each subtending an angle of 15° at the tip. These are surrounded by 12 layers, each containing 24 triangular elements, in the range $0.01 < r/a < 0.55$. The semi-circular boundaries described radii

$$\frac{a}{65} (0.5 , 1.0 , 1.625 , 1.5^2 , 2.0^2 , 2.5^2 , ... , 6.0^2)$$

The details of the mesh within $r = 0.55\ a$ are shown in figure 5.3 . The size of elements for $r > 0.55\ a$ is kept the same as that for the coarse mesh. It is considered that such element sizes, which are of the same order as those used by Chan et al[13] , are capable of producing reasonable results for points remote from the crack-tip. The relative sizes of the elements used in this mesh are given in table 5.1 . This

mesh contained 386 triangular elements and 225 nodal points giving a total of 450 degrees of freedom. Although this mesh contained about 50% more degrees of freedom than the coarse mesh, the size of the input data was kept the same. This was achieved by automatically generating the nodes within $r = 0.55\ a$.

5.1.1 Analyses Employing Elements II and CST Elements

The first solution for the cracked plate shown in figure 5.1 is obtained using the coarse mesh described in the previous section. Although this mesh may be considered to be rather coarse for fracture analysis, it was thought to be reasonable enough since the aim of the first analysis was to reproduce a solution obtained by Wilson[19] employing approximately the same number of degrees of freedom. Roller supports were imposed at the nodal points along the line of symmetry, i.e.

$$v = 0 \qquad \text{at} \quad 0 < r \leqslant 100 \quad \text{and} \quad \theta = 180^{o}$$

The crack surface nodal v-displacements were used to evaluate the crack-tip stress intensity factor k_1 from

$$k_1 = 2\,G\,\left(\frac{2\pi}{r}\right)^{\frac{1}{2}}\ v/f(\theta) \qquad (5.1)$$

where $f(\theta)$ is a function of θ given in the second of equations 2.9 .

A plot of the non-dimensional parameter $Y \left(= k_1 \frac{t W_I}{P a^{\frac{1}{2}}}\right)$ as a function of r is shown in figure 5.4 . The results rapidly approach a constant slope and by extrapolation to r = 0 , an estimate for Y of about 13.4 is obtained. Brown and Srawley[42] give a boundary collocation solution for this problem which is considered[13] to be accurate to within 0.5% . The extrapolated value obtained here is about 7% in error when compared to this solution. The same order of accuracy was obtained by Wilson[19] using about 300 degrees of freedom. Wilson used a cluster of singular tip elements (figure 3.3) of the same radius as that used here, surrounded by CST elements. Although the two solutions employ roughly the same number of degrees of freedom, as Wilson did not give the details of the mesh he used, the two meshes employed are clearly not the same. In spite of this difference and of the inevitable errors involved in the extrapolation process, it is considered that the two analysis produce results of similar accuracy. These results establish confidence in the modified programme, which in its present form can employ elements I, II and CST elements.

Although an acceptable estimate for k_1 is obtained above by the crack-surface displacement extrapolation method, a more detailed study of the results for the region near the crack-tip indicate that the accuracy is generally poor. This is demonstrated in figures 5.5 and 5.6 , where the radial and circumferential displacements u and v at the boundary of tip elements II, i.e. at r = 0.1 a are shown. The results are compared to an 'exact' solution obtained from equations 2.9 . It can generally be seen that the accuracy of the results deteriorate with increasing distance

from the free surface of the crack.

The displacement functions employed in element II make the choice of the size of the tip elements very important. It is considered that the tip elements must not be too large since the inverse square root stress variation is the only possibility allowed. A second solution employing the fine mesh described previously is obtained. In this the tip elements II had radii $R_T = 0.01\ a$. The results for u and v at the boundary of the tip elements together with the 'exact' solution are shown in figures 5.7 and 5.8 . It is seen that the results are totally unrepresentative both in magnitude and in profile. It is concluded that, when used with CST elements, elements II are not capable of assuming a small size of the order of the size of the singular region of the crack-tip. This may explain the reason why the smallest size of tip elements used by Wilson, which are similar to elements II here, was $R_T = 0.1\ a$.

5.1.2 Analyses Employing Elements I , II and CST Elements

If the state of stress or displacement in the vicinity of the crack-tip can be determined with reasonable degree of accuracy, then the stress intensity factor can be calculated by the use of equations 2.8 - 2.11 . The finite element analysis must then produce sufficiently accurate results for stresses or displacements within the region where these equations are valid. The following analysis suggests that such results for displacements are possible if tip elements II are surrounded by elements I. Using the fine mesh, the CST elements employed in the first layer are replaced by elements I. In this the singular region, represented by elements I and II, is approximately 1/70 of the crack length. The results for the u and v-displacements at the boundary $r = 0.01\ a$ are shown in figures 5.7 and 5.8 . It is seen that the results are most pleasing, with a maximum error of about 6% . A simple averaging procedure of the values of k_1 obtained from the u and v-displacements at this boundary yields results within 4% and 3% , respectively, of the collocation solution. The extrapolation curve obtained from the crack surface v-displacements is shown in figure 5.4 . From this an estimate for k_1 which is 6% in error is obtained.

The results presented in this section demonstrate the effectiveness of employing element I in the analysis. It is seen that, using a small number of degrees of freedom, accurate values of stress intensity factors can be obtained by simple averaging of the results near the crack-tip, thus obviating the need for an extrapolation process. Further studies

on the effect of employing elements I in the analysis are made in the following sections.

5.1.3 The Singular Region of the Crack-Tip

In this section the influence of the size of the singular region, represented by elements I and II, on the results for the displacements u and v near the crack-tip is examined. This is done by successively increasing the number of layers employing elements I in the fine mesh shown in figure 5.3 . Several solutions were obtained and table 5.2 gives the number and type of elements used in each solution together with the corresponding size of the singular region R_S/a , where R_S is the radius to the boundary of this region.

The results for the u and v-displacements at the boundary of tip elements II, i.e. at r = 0.01 a are shown in figures 5.9 and 5.10 . It can generally be seen that as the size of the singular region is increased beyond a/70 , overestimated values are obtained. The results suggest that, for the problem considered, the singular region is approximately half that suggested by Kobayashi et al[11]

5.1.4 Influence of Ratio R_S/R_T

Having established an approximate size of the singular region, a further study is now made on the effect of the relative sizes of elements I and II employed in this region. Keeping the radius R_S to the outside boundary of elements I to a/70 , several runs were carried out by varying the radius R_T of tip elements II. Ratios of R_S/R_T of

1.5 , 2.0 and 2.5 were considered. The results for the u and v-displacements at the outside boundary of elements I , i.e. at $r = R_S$, are shown in figures 5.11 and 5.12 . It can be seen that the ratio R_S/R_T has no apparent influence on the results.

5.1.5 Results for Stresses Near the Crack-Tip

As pointed out in section 5.1.2 , if sufficiently accurate results for stresses near the crack-tip can be obtained, then estimates for stress intensity factors may be calculated by the direct application of equations 2.8 - 2.11 . The results for the stresses at the boundary of tip elements II, for $R_S = a/70$ and $R_S/R_T = 2.0$, are shown in figures 5.13 - 5.15 . These are compared to the 'exact' solution obtained from equations 2.8 . It is seen that the accuracy is inferior to that obtained for displacements. Significant improvements are generally obtained when the stresses are calculated at the mid-boundary of the tip elements. It is seen that this improvement is more pronounced for the range $0 < \theta < 60^\circ$. In figures 5.16 - 5.18 the stresses at the middle of the outside boundary of elements I are shown. These indicate that the accuracy improves with increasing distance from the crack-tip.

5.2 Single-Edge Cracked Plate in Tension

In this section a solution for another type of specimen used in k_{1c} testing is obtained. The problem considered is that of an axially loaded single-edge cracked plate whose dimensions are given in figure 5.19 . The plate is considered under plane strain conditions with $E = 200$, $\nu = 0.3$ and $t = 1.0$. Taking advantage of the symmetry, only the upper half of the plate is analysed. The finite element mesh used in the analysis is shown in figure 5.20 . The details of the mesh within $r = 0.55$ a are the same as those used in the fine mesh of the previous problem (see figure 5.3) . This representation contained 434 triangular elements and 279 nodes with a total number of degrees of freedom of 558 .

It is considered[42] that, for this problem, the most accurate estimate for k_1 is that by boundary collocation due to Gross et al[43] . This is given by[42]

$$k_1 \frac{t}{P}\frac{W}{a^{\frac{1}{2}}} = 1.99 - 0.41\,(a/W) + 18.70\,(a/W)^2 - 38.48\,(a/W)^3 + 53.85\,(a/W)^4 \qquad (5.2)$$

This solution, which is within 0.4% for values of a/W up to 0.6 , is based on the assumption that the tensile load is uniformly distributed across the width of the plate at a distance from the crack not less than the width. A valid assumption, provided that the distance between loading points is not less than three times the width of the plate. In the present

analysis this distance is four times the width of the plate.

The extrapolation curve obtained from the crack surface v-displacements is shown in figure 5.19 . This gives an estimate for k_1 which is 8.4% in error. By averaging the values for k_1 obtained from the v-displacements around the crack-tip at $r = 0.01\ a$, an estimate which is less than 6% in error is obtained. It is suggested that the larger outer element sizes, i.e. $A/a^2 = 0.1$, compared to those used for the problem of the preceding section (table 5.1) may be accountable for the smaller degree of accuracy obtained here.

The extrapolation curves obtained in section 5.1 (figure 5.4) correspond to a condition where the uncracked part of the crack plane is subjected to a high degree of bending. It is interesting to note that for the problem analysed in this section, where the crack plane is subjected to a smaller degree of bending, the slope of the extrapolation curve (figure 5.19) is less than that for the previous problem. This behaviour supports the results obtained by Chan et al[13], where the extrapolation curve for a crack in a uniform stress field was found to have a negative slope.

5.3 Compact Tension Specimen

In this section, solutions for the compact tension specimen shown in figure 5.21 are obtained. Several crack sizes were considered. The finite element representation for the case of a/W = 0.33 is shown in figure 5.22 . The mesh, which is obtained by making some modifications to that shown in figures 5.2 and 5.3, contain 394 elements and 232 nodal points with a total of 464 degrees of freedom. For brevity, no details of the meshes employed for the other crack sizes are given. The total number of degrees of freedom for all the meshes used ranged between 458 and 464 .

In fracture toughness testing, the load corresponding to a 2% increment of crack extension is obtained. The k_{1c} value is calculated from this load using a boundary collocation solution[42] , viz :-

$$k_1 \frac{t W^{\frac{1}{2}}}{P} = 29.6\ (a/W)^{\frac{1}{2}} - 185.5\ (a/W)^{3/2} + 655.7\ (a/W)^{5/2} - 1017.0\ (a/W)^{7/2} + 638.9\ (a/W)^{9/2} \qquad (5.3)$$

In figure 5.23 , the finite element results for the stress intensity factors obtained by averaging around the crack-tip are shown together with the boundary collocation solution.

5.4 Conclusions

A new finite element programme, based on that of Coughlan[41] , was developed. This programme is capable of employing the singular elements I and II , developed in the present work, together with CST elements. The programme was tested by solving a problem previously analysed by Wilson[19].

Several problems of the type used in fracture toughness analysis were solved. Although acceptable estimates for stress intensity factors were obtained by the crack-surface displacement extrapolation method, the results demonstrated that the accuracy of the displacements near the crack-tip, when using elements II and CST elements, were generally poor. It is concluded that, when used with CST elements, element II which is similar to that of Wilson[19] is not capable of assuming a small size of the order of the size of the singular region of the crack-tip. The results were greatly improved when elements II were supplemented by a ring of elements I . Using a small number of degrees of freedom, accurate values of stress intensity factors were obtained by simple averaging of the values around the crack-tip, thus obviating the need for an extrapolation process. A size of the singular region of the crack-tip, half that suggested by Kobayashi et al[11], was obtained.

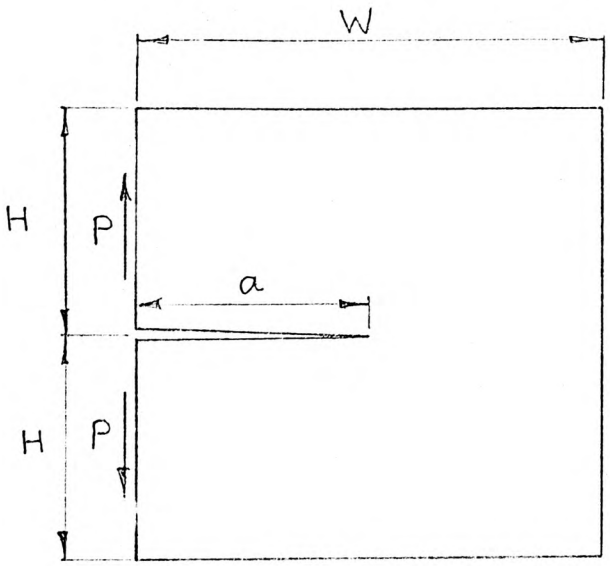

W = 200

H = 100

a = 100

E = 200 , ν = 0.3

t = 1.0 , P = 100

Figure 5.1 Crackline loaded square plate

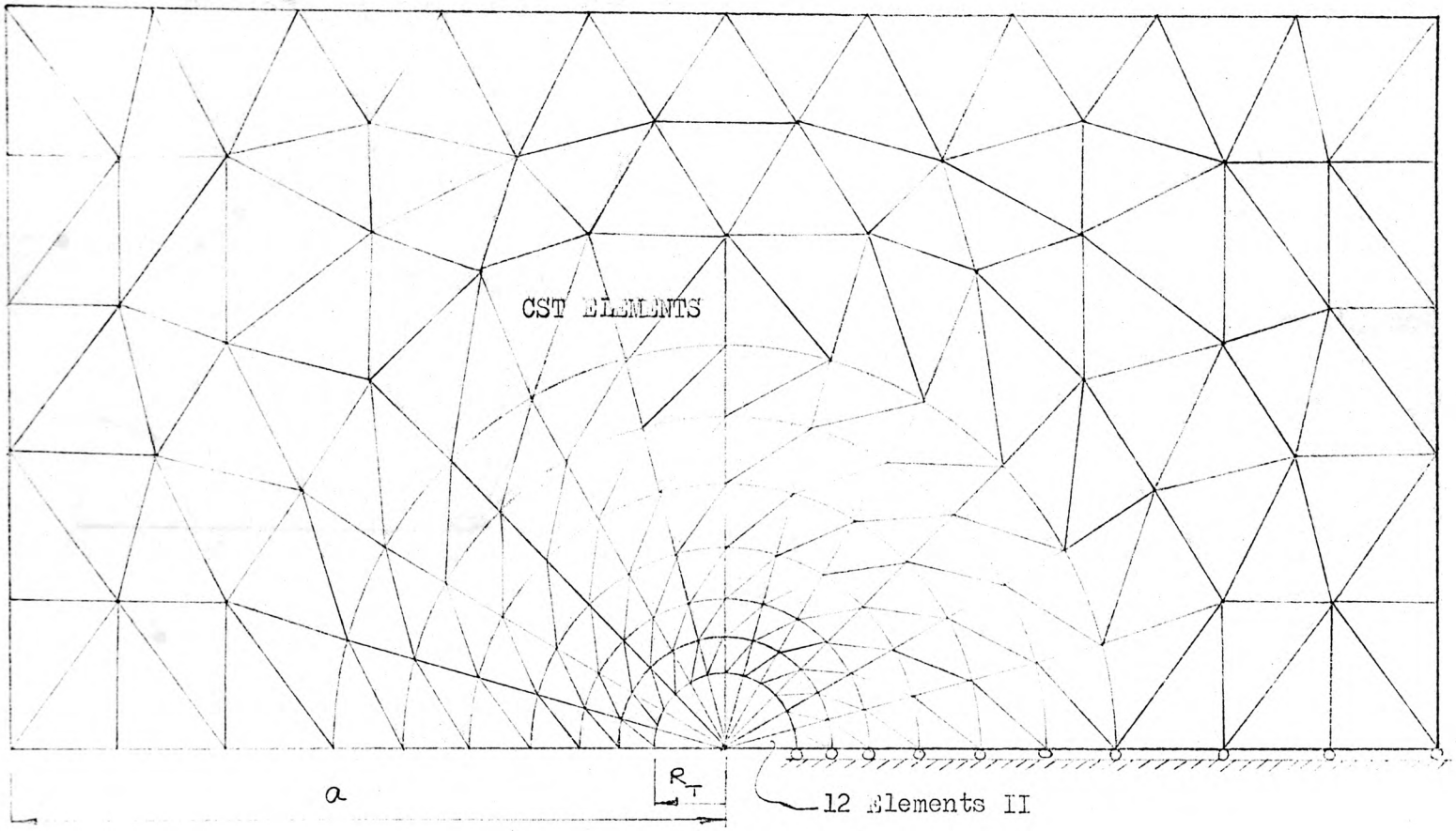

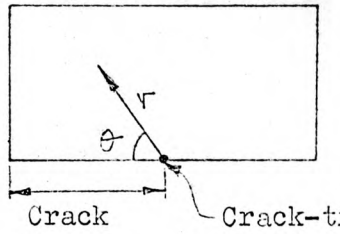

Notation for r and θ

Figure 5.2 Finite element idealisation - Coarse mesh

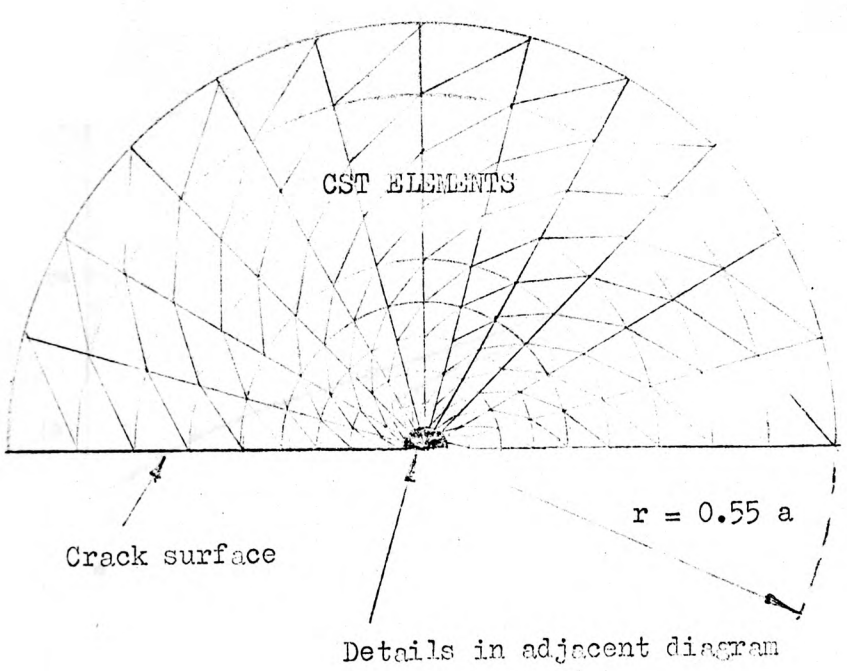

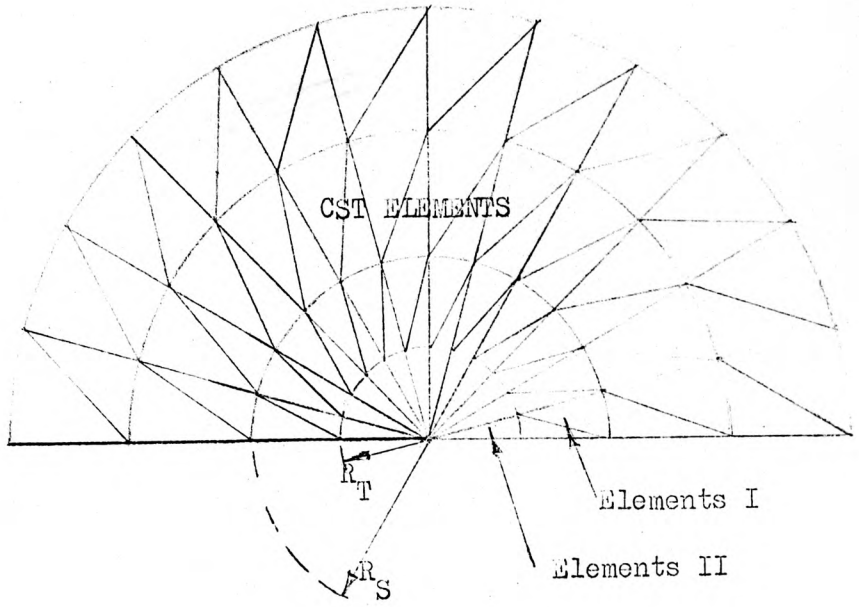

Expanded view near the crack-tip

Figure 5.3 Details within r = 0.55 a - Fine mesh

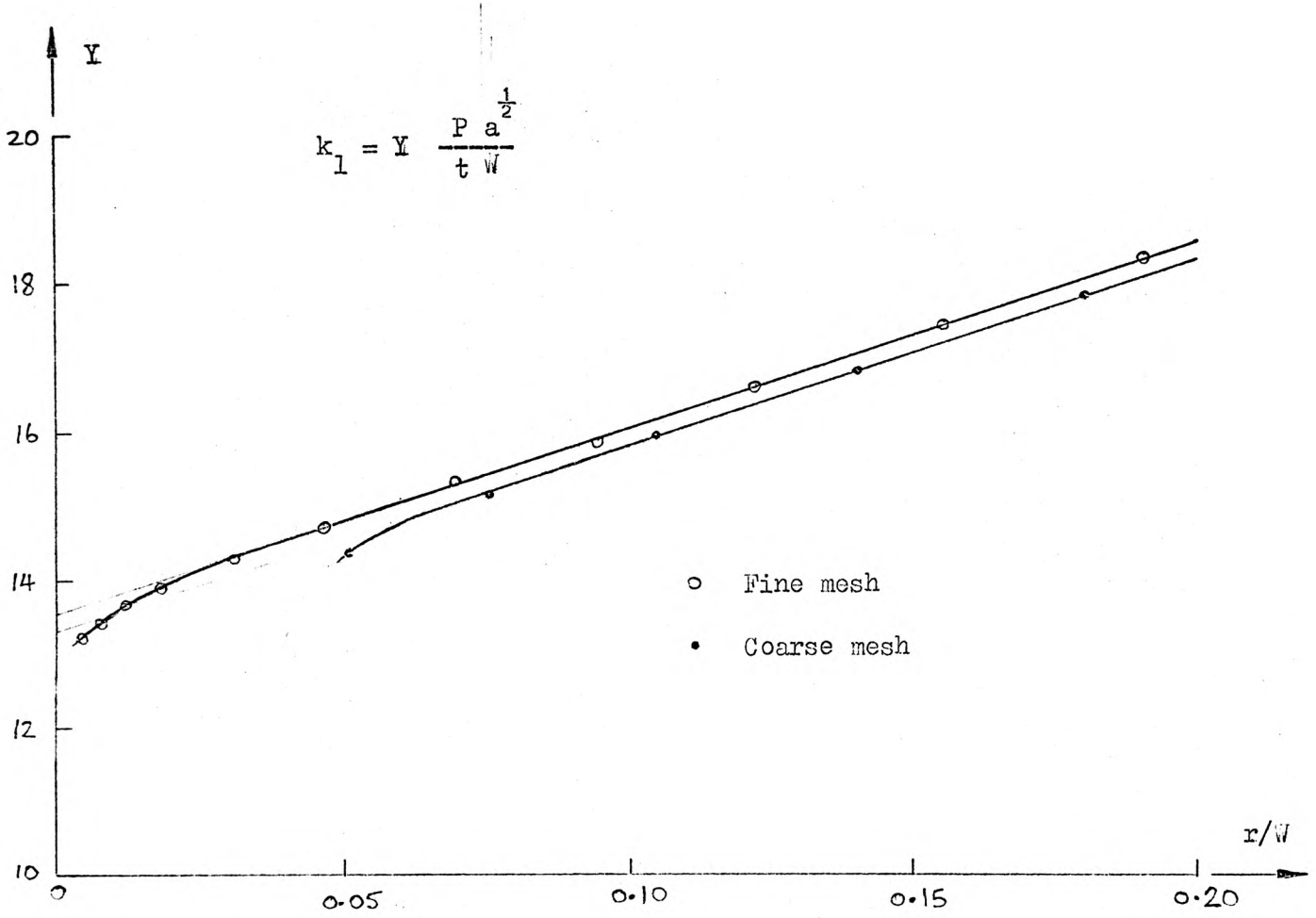

Figure 5.4 Extrapolation curve for the stress intensity factor

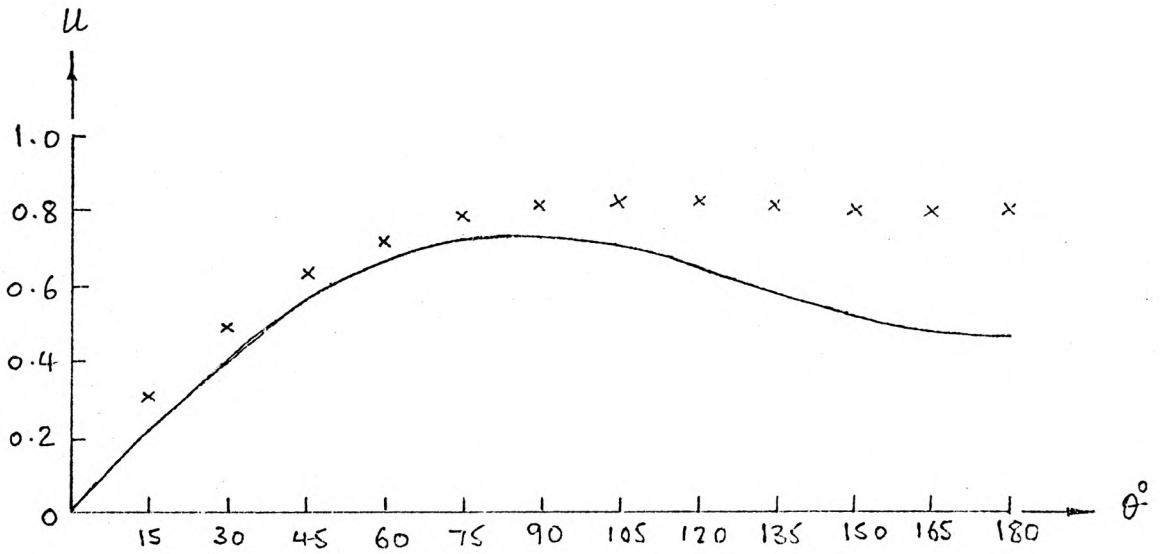

Figure 5.5 Distribution of radial displacements at r = 0.1 a

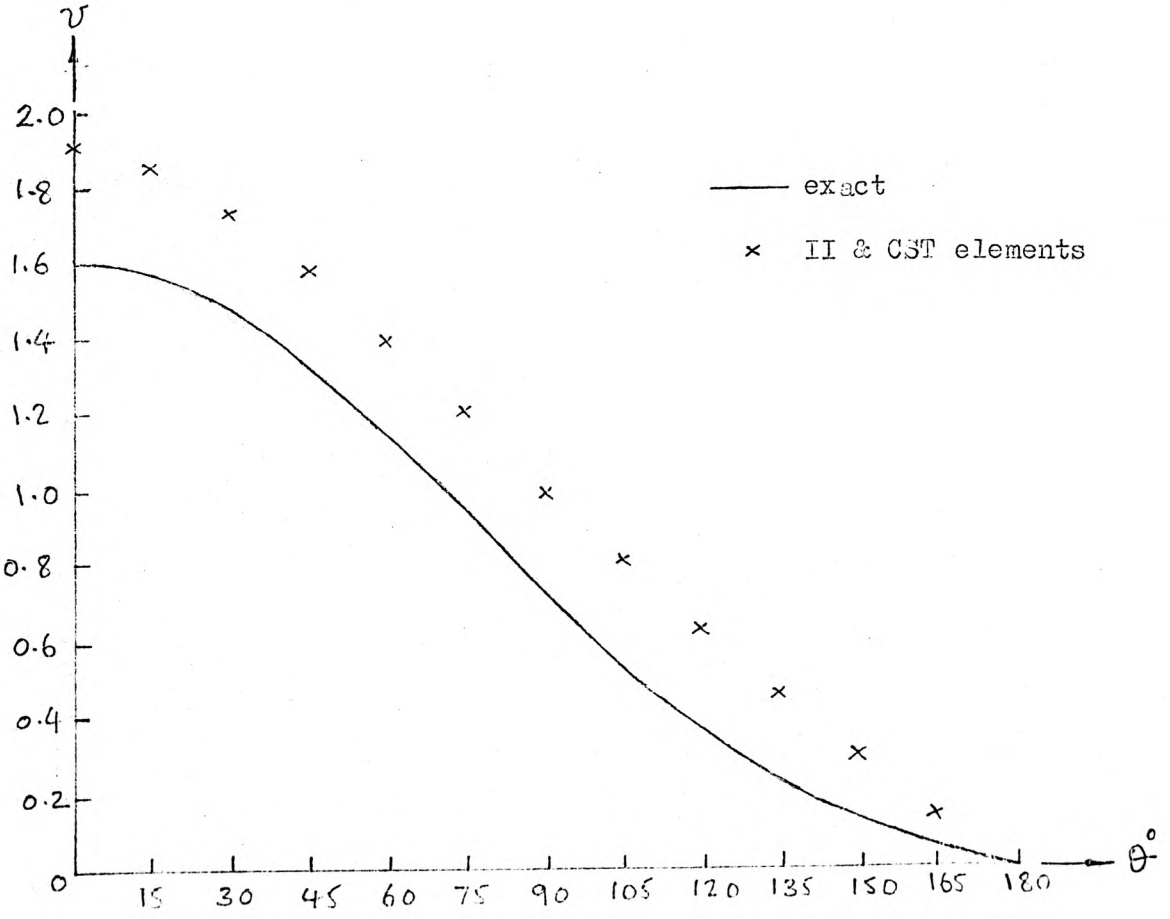

Figure 5.6 Distribution of circumferencial displacements at r = 0.1 a

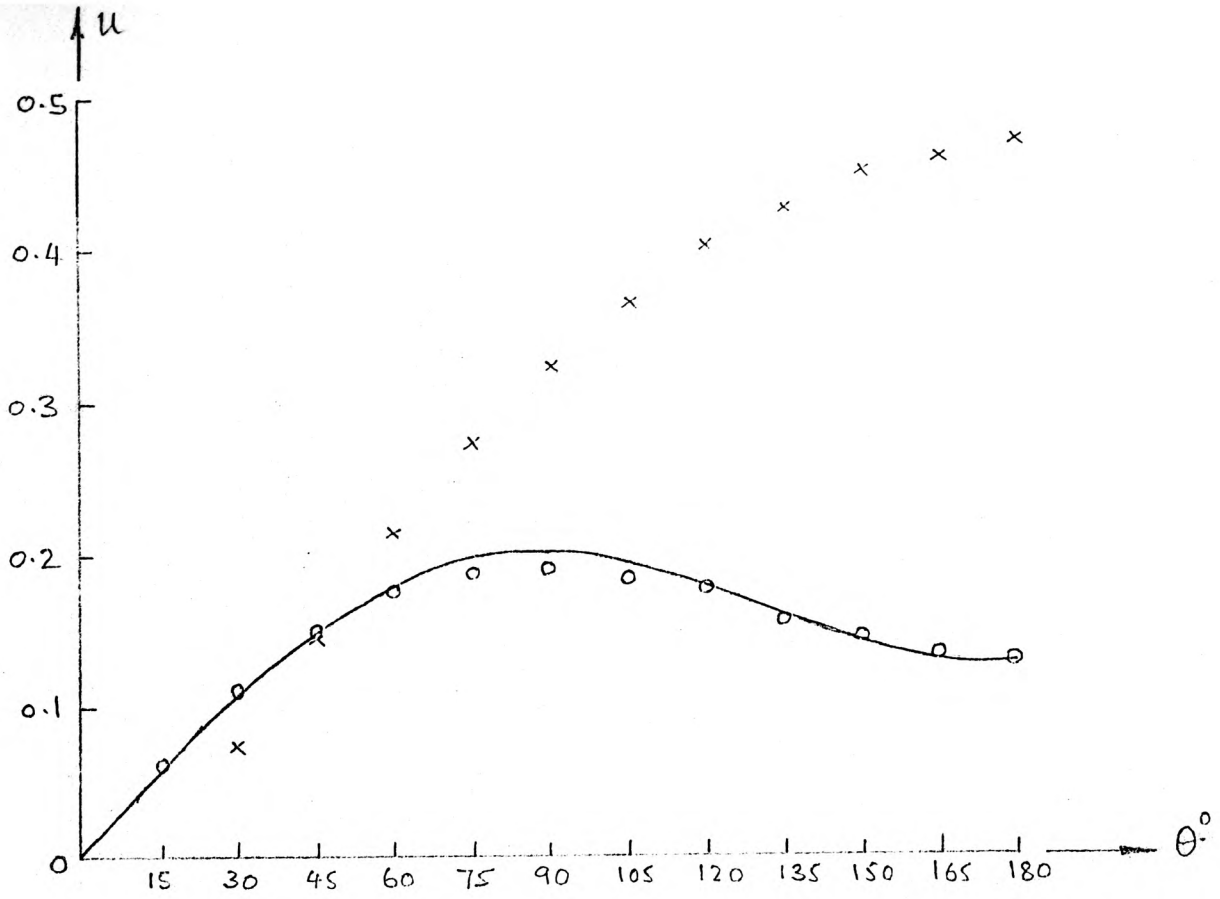

Figure 5.7 Distribution of radial displacements at r = 0.01 a

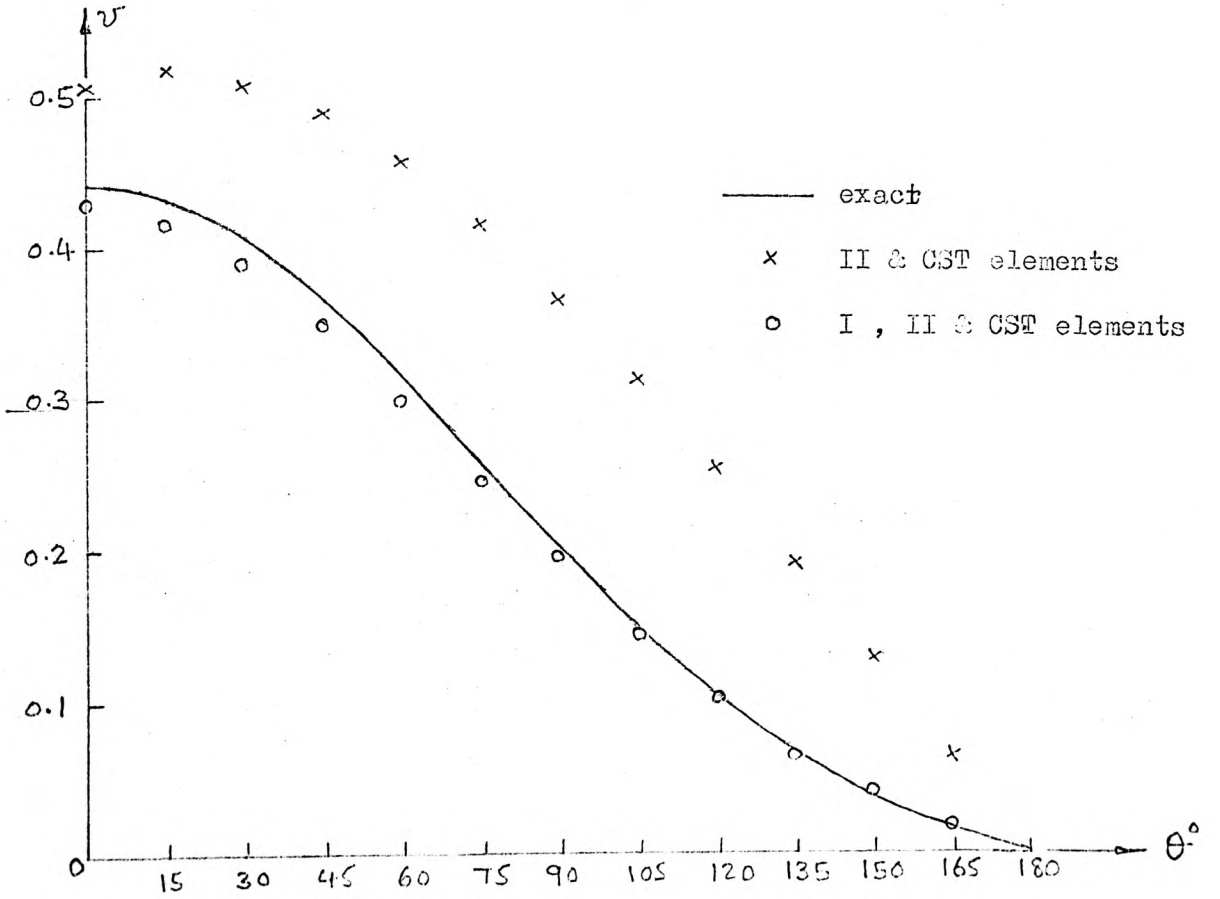

Figure 5.8 Distribution of circumferencial displacements at r = 0.01 a

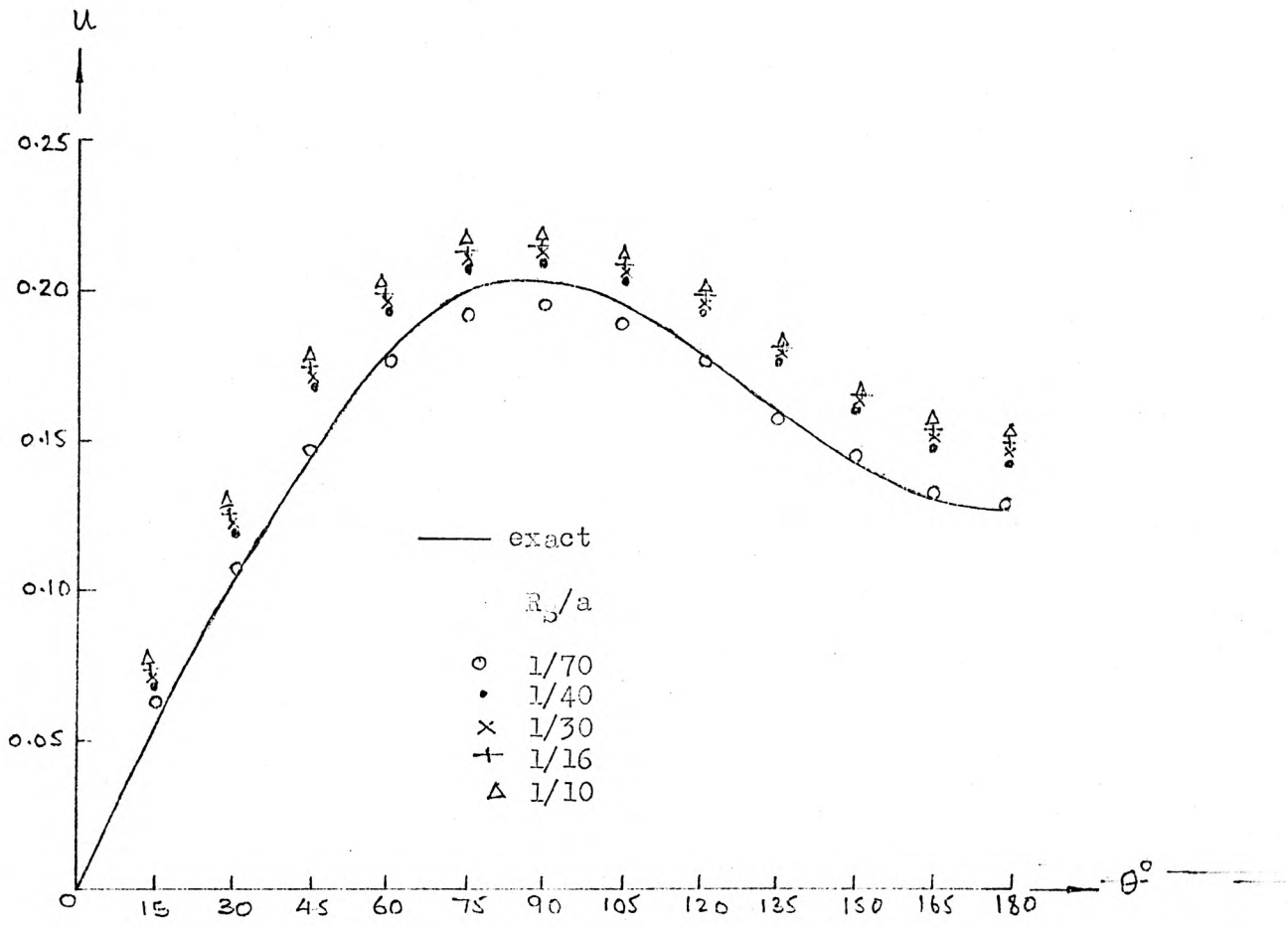

Figure 5.9 Influence of size of singular region on radial displacements

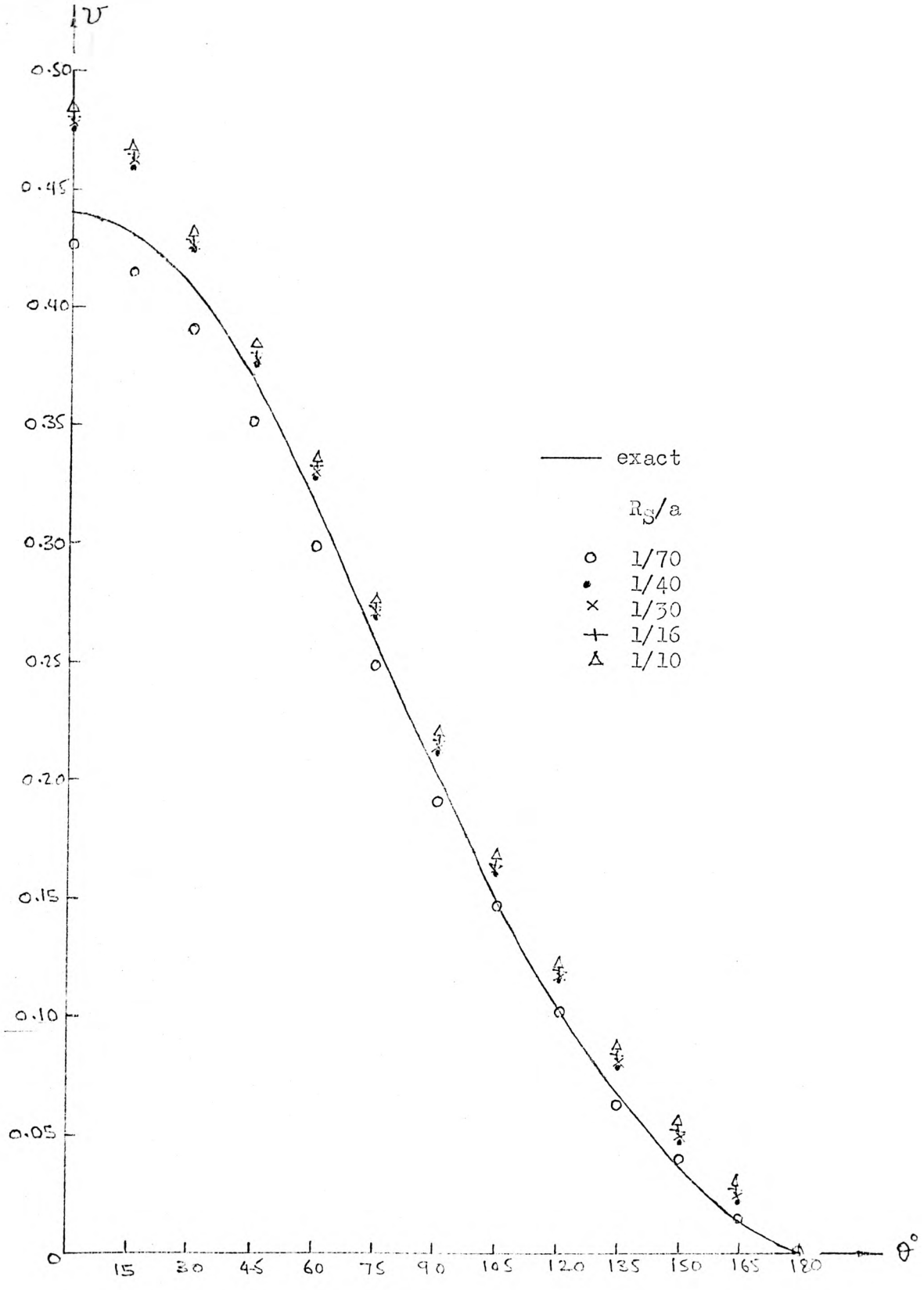

Figure 5.10 Influence of size of singular region on circumferencial displacements

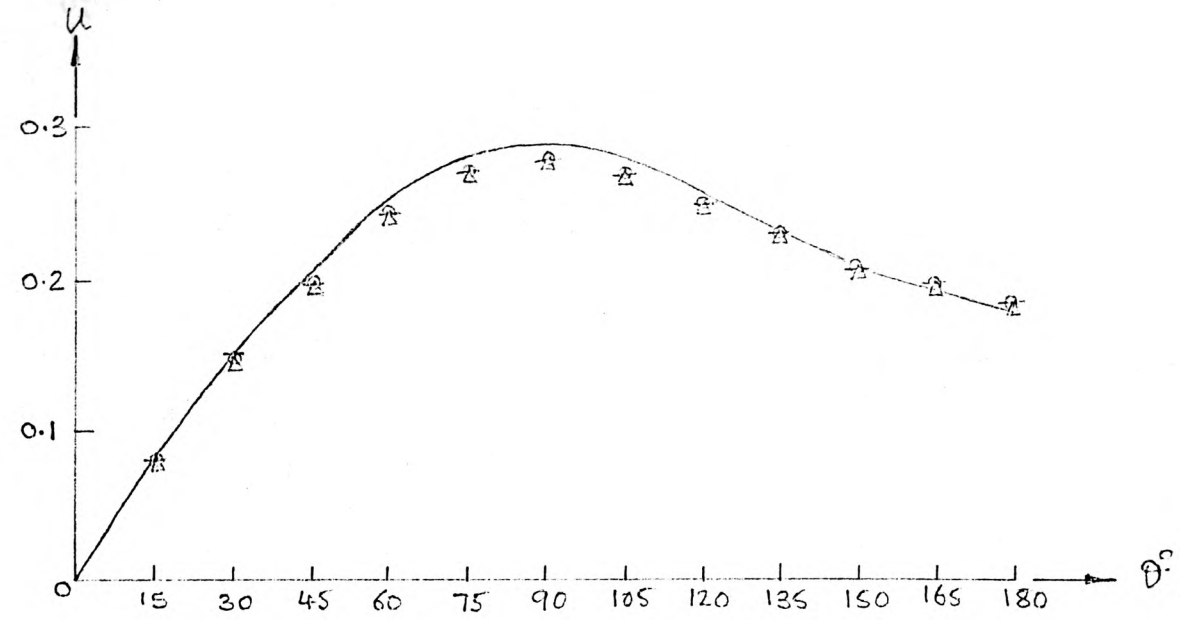

Figure 5.11 Influence of R_S/R_T on radial displacements

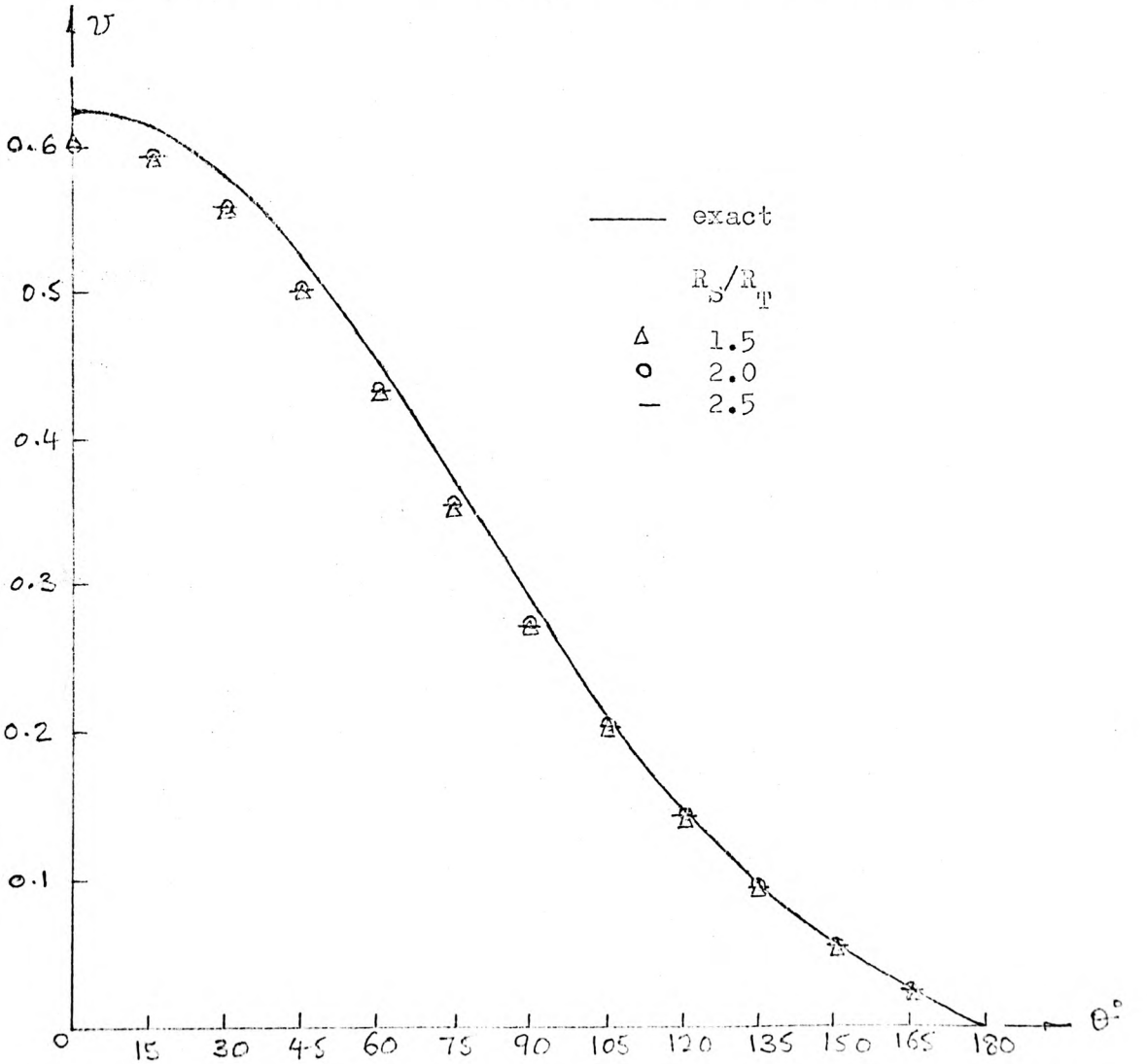

Figure 5.12 Influence of R_S/R_T on circumferencial displacements

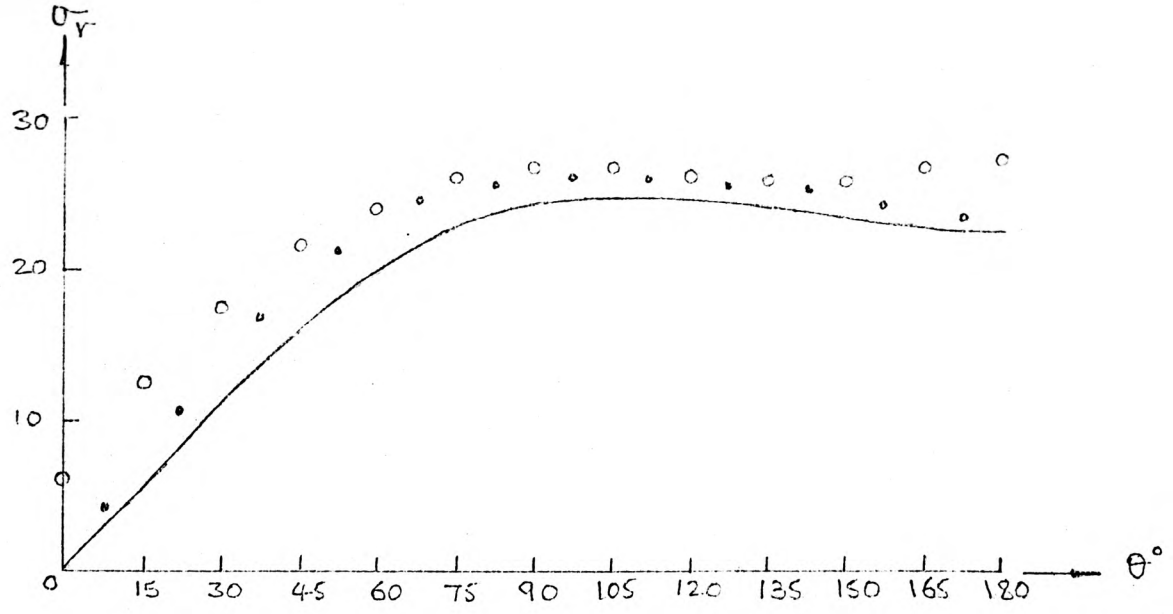

Figure 5.13 Distribution of radial stress at r = 0.01 a

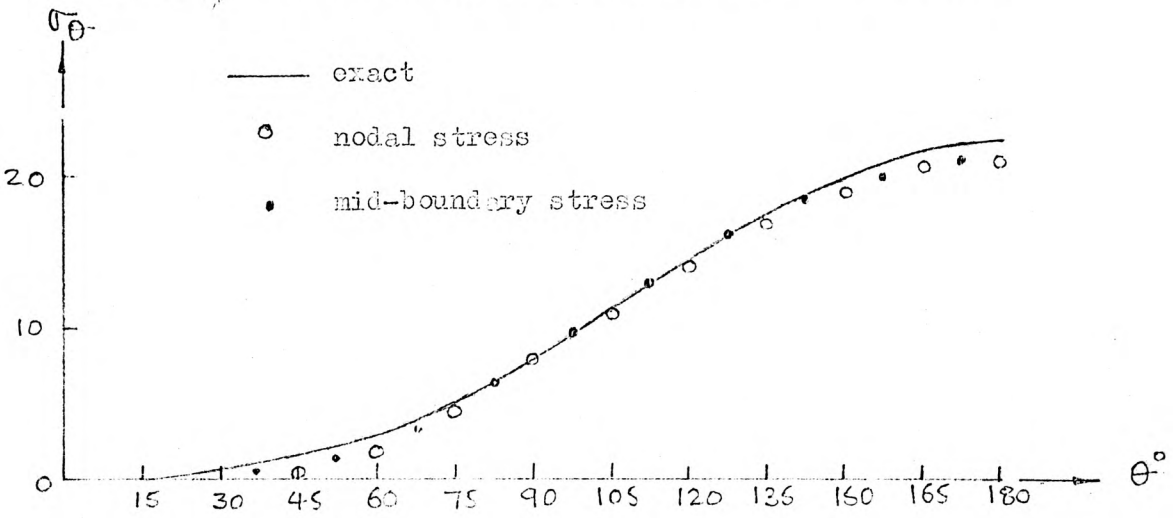

Figure 5.14 Distribution of circumferencial stress at r = 0.01 a

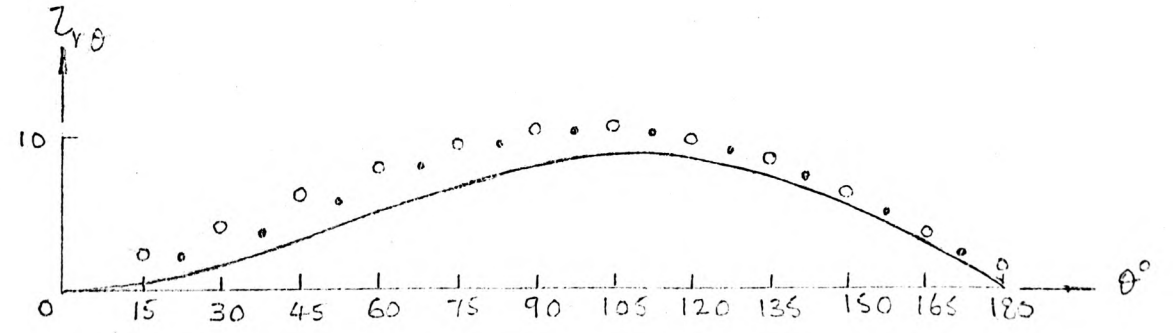

Figure 5.15 Distribution of shearing stress at r = 0.01 a

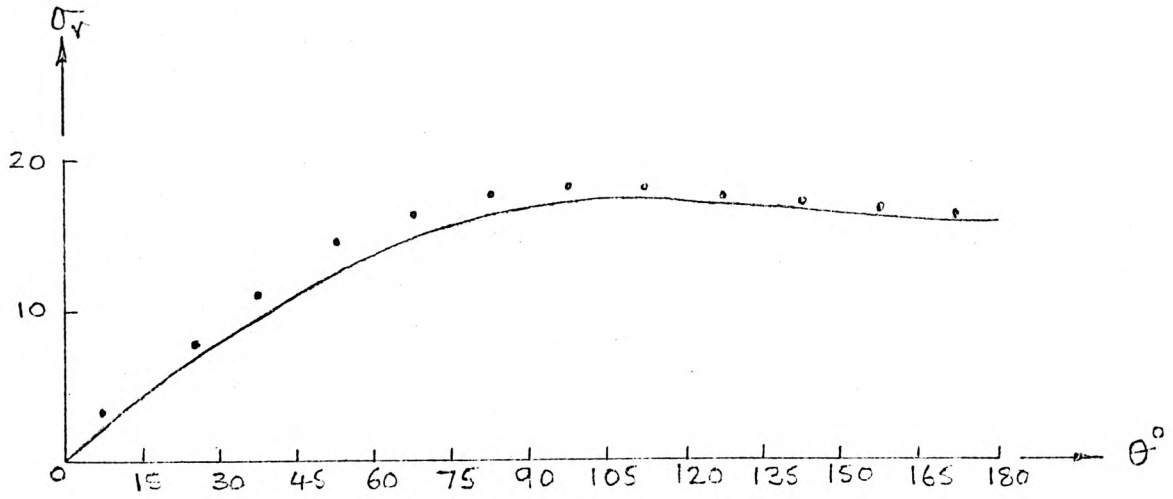

Figure 5.16 Distribution of radial stress at r = 0.015 a

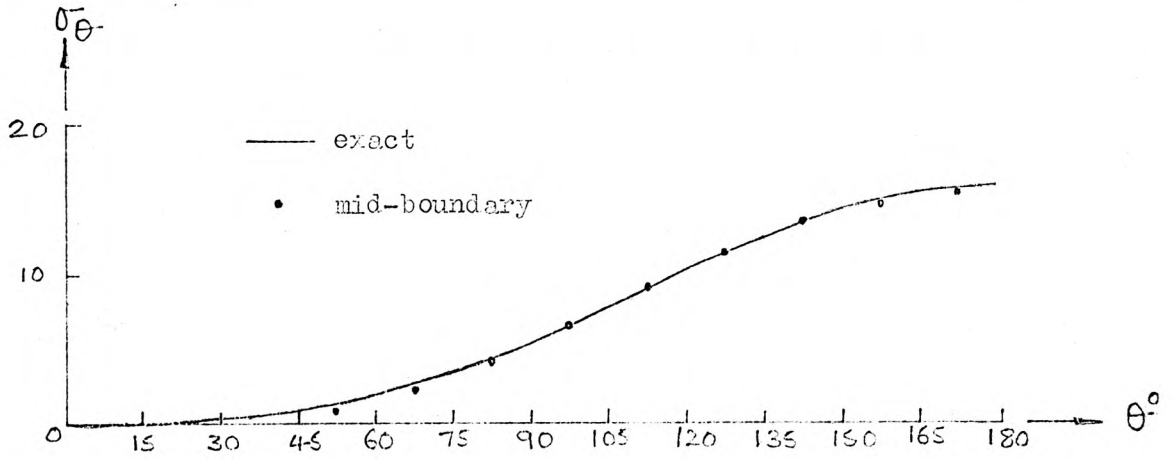

Figure 5.17 Distribution of circumferencial stress at r = 0.015 a

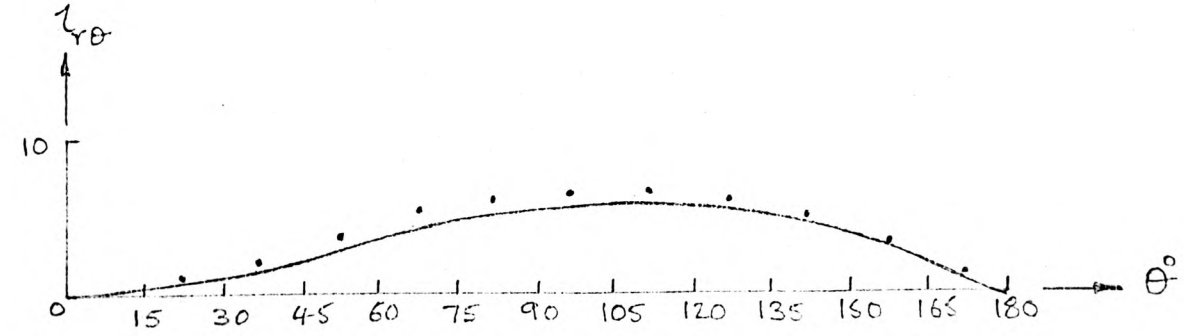

Figure 5.18 Distribution of shearing stress at r = 0.015 a

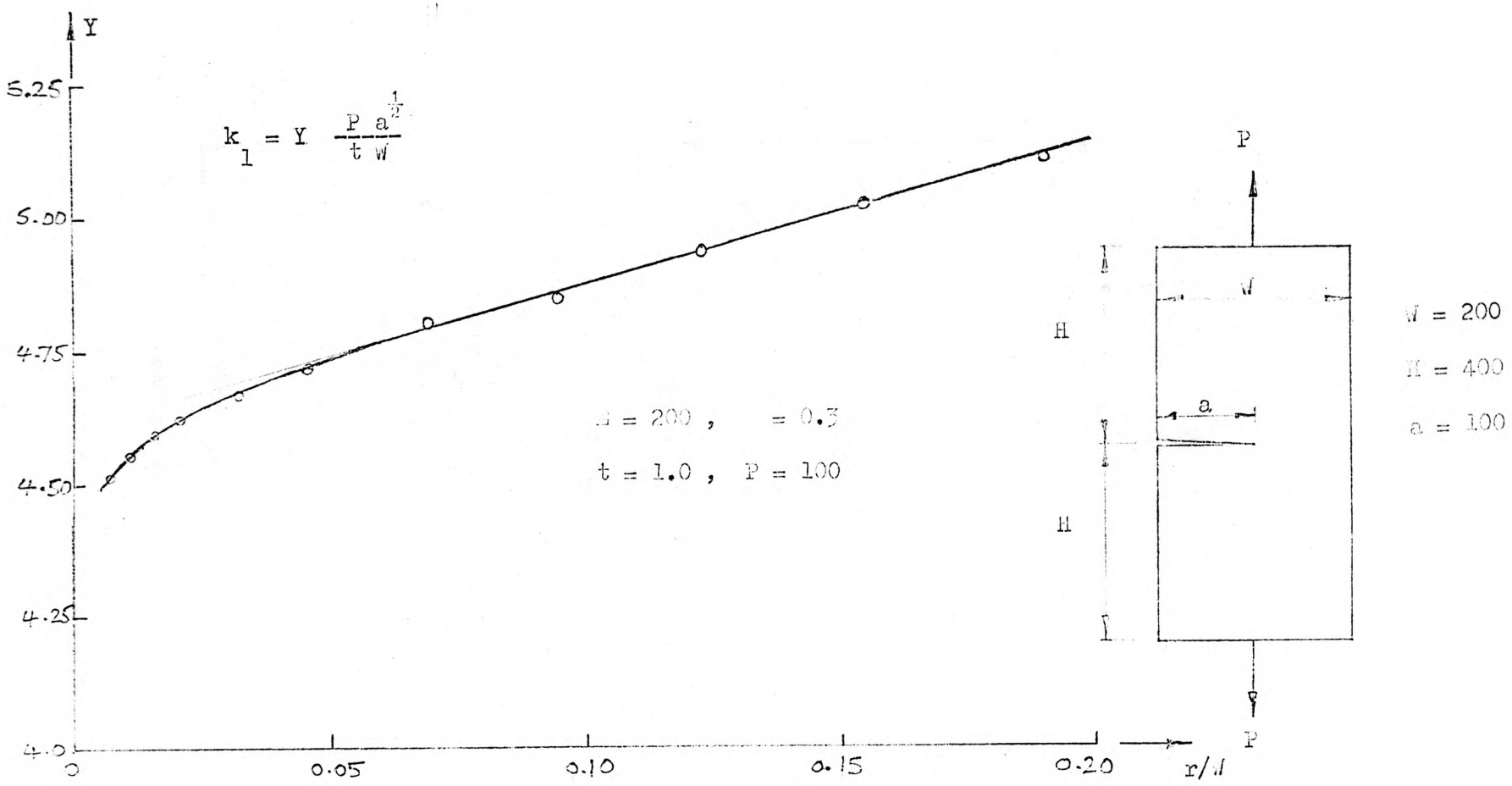

Figure 5.19 Extrapolation curve for the stress intensity factor

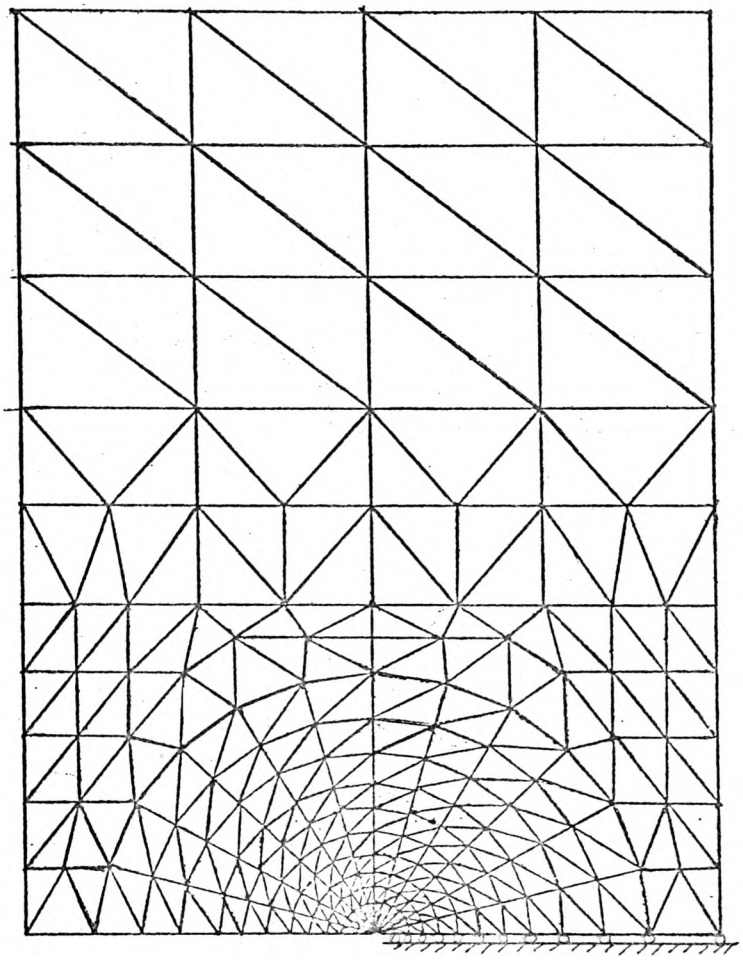

Figure 5.20 Finite element mesh for the edge cracked plate shown in figure 5.19

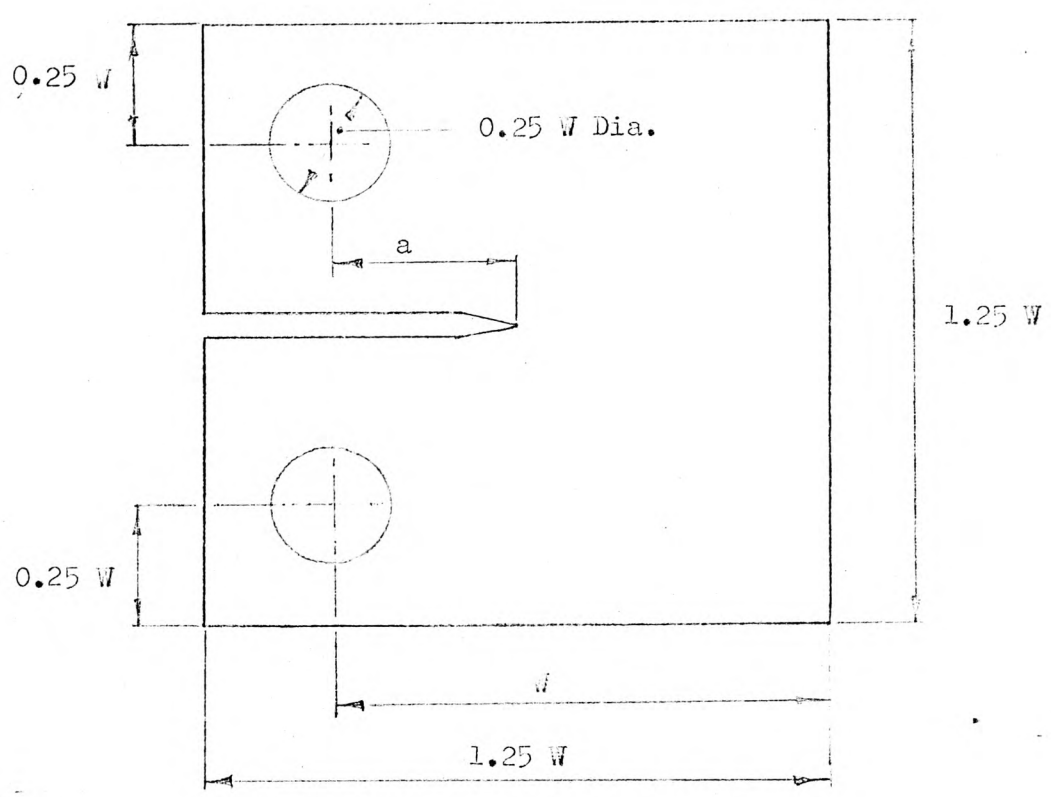

Figure 5.21 Compact tension specimen

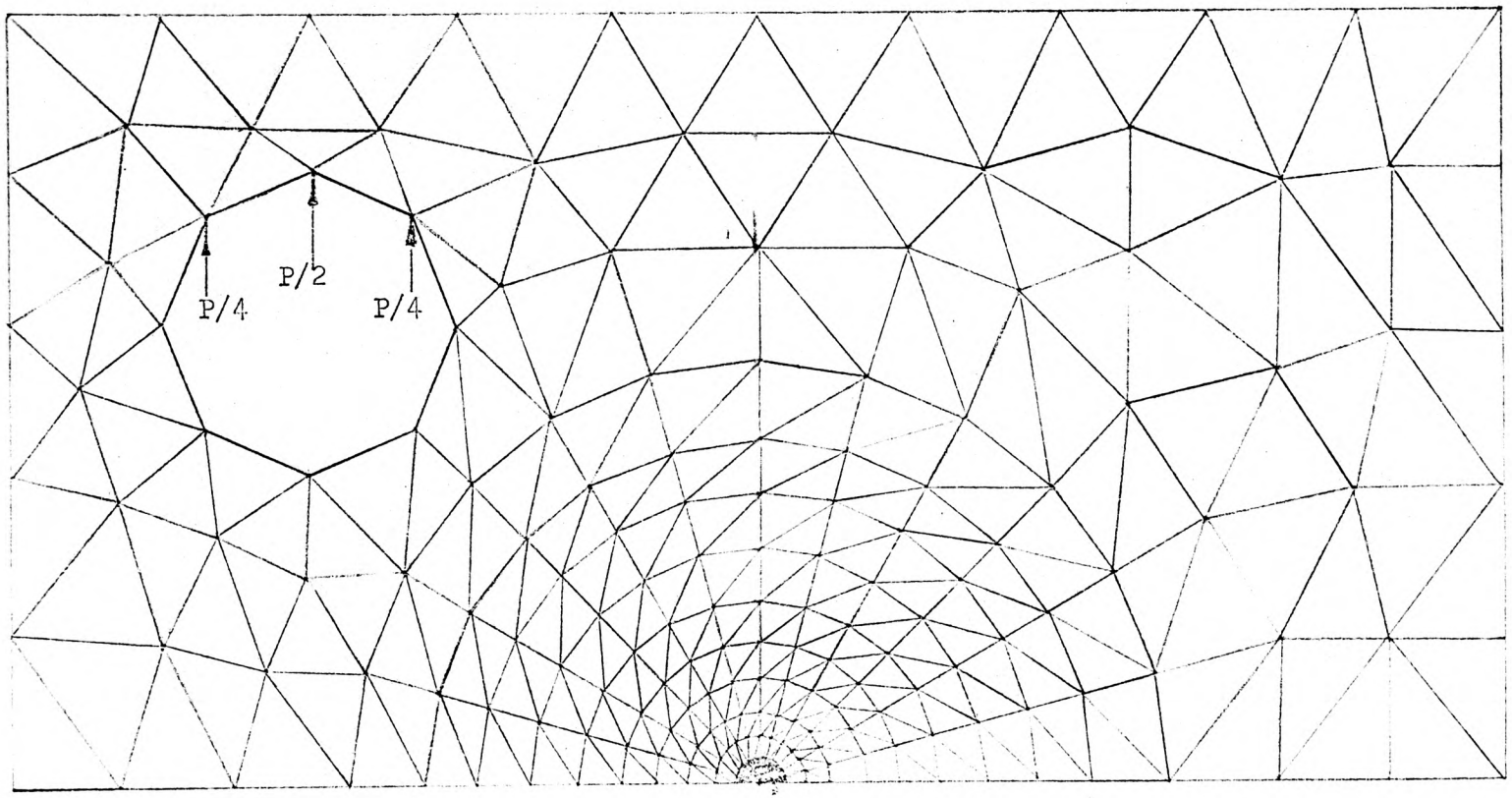

Figure 5.22 : Finite element representation for compact tension specimen

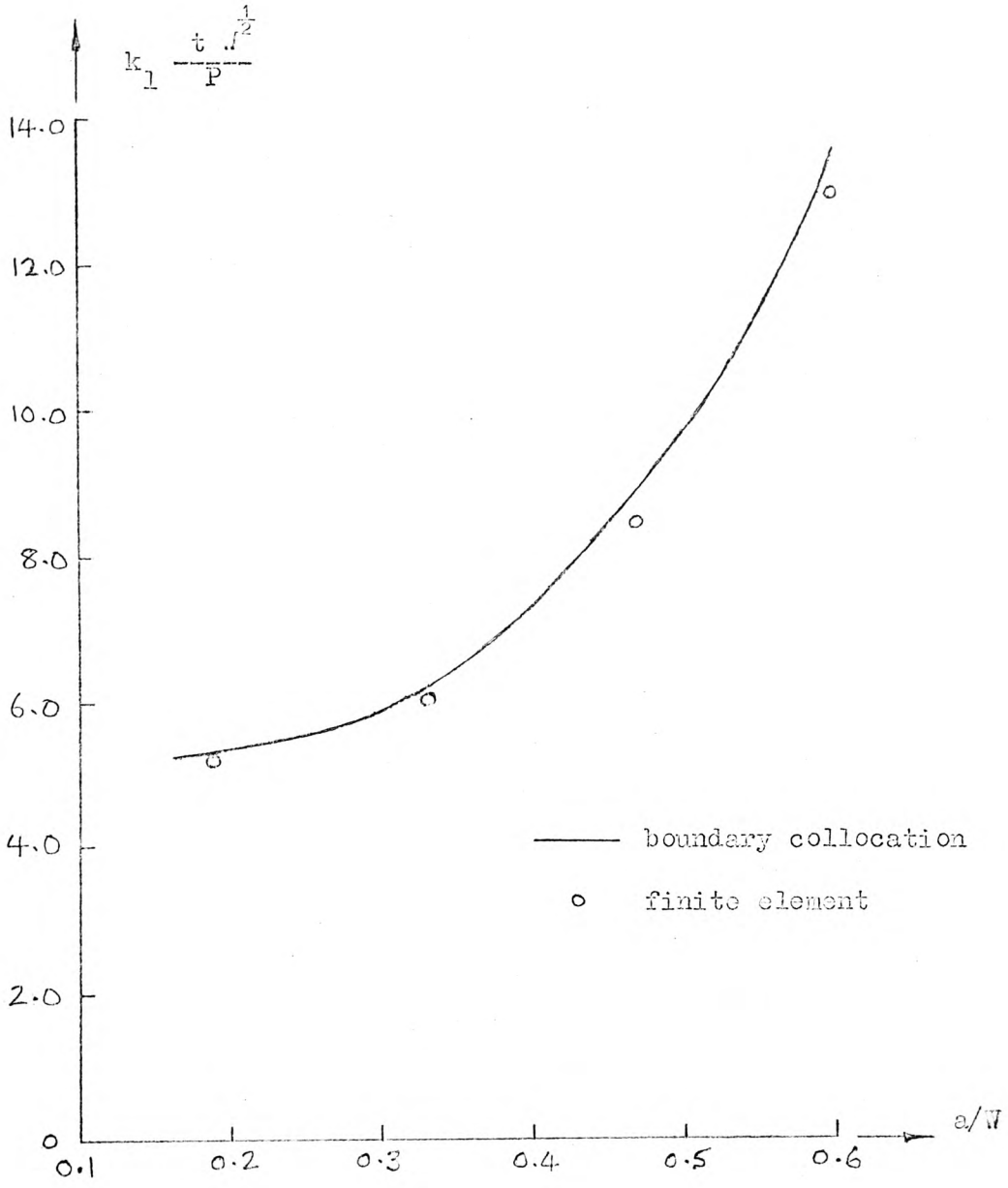

Figure 5.23 Comparison of results of boundary collocation and finite element solutions - Compact tension specimen

	Element sizes A/a^2		
	Tip elements	Inner elements $\times 10^{-6}$	Outer elements $\times 10^{-2}$
coarse mesh	1300	800	1.5
fine mesh	8	12	1.5

A = element area , a = crack length

Table 5.1 Element sizes for coarse and fine meshes

number of elements II	number of elements I	number of CST elements	R_s/a
12	24	362	1/70
12	48	338	1/40
12	72	314	1/30
12	96	290	1/16
12	120	266	1/10

Table 5.2 Size of the singular region

CHAPTER 6 APPLICATIONS TO ECCENTRICALLY LOADED SPLIT-CUBES

In a recent paper Bear and Barr[44] described two tests which may be used to evaluate the fracture toughness of both rock and fine-grained concrete. The tests were carried out on circumferentially notched round bar specimens which were subjected to two loading systems. In the first, the specimens were subjected to four-point loading as shown in figure 6.1, and in the second the specimens were loaded eccentrically as shown in figure 6.2 . More recently Barr[45] describes a new test for the evaluation of fracture toughness of concrete of ordinary mixes. The test, which is a natural development of the arrangements shown in figure 6.2 , employs concrete cubes with slits on two opposite faces as shown in figure 6.3 .

Experimental work in this area employs expressions, which originate from the work of Neuber[46] , to evaluate the fracture toughness k_{1c} from the fracture loads. The work presented in this chapter demonstrates that inconsistancy results when using these expressions. Improved results are obtained from the finite element solutions using the fracture loads obtained experimentally.

6.1 The Stress Intensity Factor for a Split Cube Under Eccentric Loading

The resulting forces due to the eccentric load shown in figure 6.4 may be resolved into two components. The first is a compressive load acting along the axis of the cube and the second is a bending moment. If the eccentricity of the load is sufficient, tensile stresses will develop in the specimen, thus providing conditions for the opening of the crack in mode 1 situation.

The stress intensity factor k_1 may be considered to be composed of two parts; a bending component and a direct compressive component, thus

$$k_1 = k_{1B} - k_{1T} \tag{6.1}$$

where k_{1B} is the component due to the bending stress field and k_{1T} is that due to the axial loading stress field. The latter component is negative because it represents forces causing crack closure.

Irwin[8] expresses the stress intensity factor in terms of the maximum stress at the root of a crack or notch by the relationship :-

$$k_1 = \lim_{\rho \to 0} \frac{1}{2} \sigma_m (\pi \rho)^{\frac{1}{2}} \tag{6.2}$$

where σ_m = maximum stress at notch root

and ρ = the radius of curvature of the notch root

The stresses at notch roots have been extensively studied by Neuber[46]. Expressions for σ_m were derived for a number of loading conditions. In these σ_m is expressed in terms of the nominal stress σ (i.e. the stress which would occur without the notch) multiplyed by a stress concentration factor S . Thus

$$k_1 = \lim_{\rho \to 0} \frac{1}{2} S \sigma (\pi \rho)^{\frac{1}{2}} \qquad (6.3)$$

Bear[47] obtained expressions for k_{1B} and k_{1T} for a circumferentially notch round bar under eccentric loading, using the expressions for S developed by Neuber. It can be shown that for the split cube in figure 6.4 ,

$$k_{1B} = \frac{3 P e}{4 d} \left[\frac{\pi a}{t^3 (0.2 t + 1.38 a)} \right]^{\frac{1}{2}}$$

and

$$k_{1T} = \frac{P}{4 d} \left[\frac{\pi a}{t (0.2 t + 0.62 a)} \right]^{\frac{1}{2}}$$

Hence

$$k_1 = \frac{P (\pi a)^{\frac{1}{2}}}{4 d} \left[\frac{3 e}{\sqrt{t^3 (0.2 t + 1.38 a)}} - \frac{1}{\sqrt{t (0.2 t + 0.62 a)}} \right] \qquad (6.4)$$

The fracture toughness is the value of k_1 from the above expression when P is taken as the load at failure.

6.2 Experimental Results

This section summarises the results of recent tests carried out by Barr and Bear[45] on split cubes loaded eccentrically. An Instron 1251 model testing machine was used, and the eccentric load (figure 6.4) was applied through two lengths of 6 mm square steel bars. The point of application of the load was taken at the inside edges of the steel bars, since as deformation took place the load was concentrated to those edges. Load - displacement curves were plotted autographically and the maximum load recorded during a test was taken as the load at fracture.

The first tests were carried out on 100 mm cubes. Three depths were investigated for four water - cement ratios. The results for these tests are summarised in table 6.1 . A number of cubes with notch depth of 25 mm did not fail by a crack propagating from the tensile zone. Almost half these cubes failed in shear in the zone adjacent to the point of application of the load. The results of these tests were omitted when obtaining the average fracture loads.

Another set of tests were carried out on 150 mm cubes of a standard mix whose details are given in table 6.2 . Again, several notch depths were considered. The tests were repeated for an identical mix to check for reproducibility. The average values of the loads at fracture obtained from these tests are also shown in table 6.2 .

The fracture toughness values are obtained by substituting for the fracture loads in equation 6.4 . Although reproducible values of fracture

loads were obtained, it was found that equation 6.4 lead to considerable variation in the fracture toughness for different notch depths.

6.3 The Finite Element Results

Finite element solutions for the split cube shown in figure 6.4 were obtained. Both 100 mm and 150 mm cubes were analysed. Plane strain conditions were assumed with E = 13.33 and ν = 0.2 . Several notch depths were considered giving a range of a/d ratios. The finite element representations were similar to those used for the problems of the previous chapter. For brevity, the details of only one of the meshes employed in the upper halves of the cubes are given. This is shown in figure 6.5 for the case of a 100 mm cube with notch depth a = 25 mm. The region within r = a/70 surrounding the tip of the notch in the tension zone was covered by elements I and II . The remainder of the body was represented by CST elements. This representation contained 373 elements and 219 nodal points giving a total of 438 degrees of freedom. In order that results of similar accuracy are obtained from all analyses, the meshes employed for the other notch depths had a total number of degrees of freedom ranging between 438 and 446 . Roller supports were employed at the nodal points along the uncracked part of the notch plane as shown in figure 6.5 . The loads at fracture obtained experimentally were applied at a distance of 6 mm from the edges of the cubes.

The results for the stress intensity factors for the 100 mm cubes obtained from the v-displacements around the tip of the notch are shown

in table 6.3 . In this , the convention for θ is as shown in figure 4.6 . It can be seen that the variation in the k_1 values for a given a/d ratio is very small. With the exception of a single value for a/d = 0.4 , i.e. at $\theta = 165^{\circ}$, the difference between the maximum and minimum estimates for k_1 for a given a/d ratio is less than 2% of the average value. The results given in table 6.3 are for P = 100 and thickness = 1.0 .
A comparison between the finite element results and those calculated from equation 6.4 is made in figure 6.6 . It can be seen that considerable difference is obtained, particularly for the smaller a/d ratios considered.

It is customary to express results for the stress intensity factors in terms of a polynomial function in crack size/width , i.e. a/d ratio. The five a/d ratios considered in the finite element analyses enabled the results to be expressed in terms of five powers of a/d , similar to those used for the compact tension specimen[42]. For the 100 mm cubes, the following expression was obtained :-

$$k_1 = \frac{P}{B\,d^{\frac{1}{2}}} \left[18.3\,(a/d)^{\frac{1}{2}} - 430.0\,(a/d)^{3/2} + 3445.2\,(a/d)^{5/2} - 11075.8\,(a/d)^{7/2} + 12966.8\,(a/d)^{9/2} \right] \qquad (6.5)$$

where P = eccentric load,

B = thickness,

d = cube size,

and a = crack size

Equation 6.5 gives values of stress intensity factors within 2% of the finite element results.

The fracture toughness values obtained from the finite element results together with those obtained using equation 6.4 are summarised in table 6.4 . Figure 6.7 shows the variation of fracture toughness with a/d ratio. It can be seen that equation 6.4 lead to considerable variation, while those obtained from the finite element analyses give relatively constant values. The results also demonstrate that considerably larger values of fracture toughness are obtained using equation 6.4 .

The results for the 150 mm cubes are summarised in table 6.5 and figures 6.8 and 6.9 . It can be seen that equation 6.4, again, give higher values of fracture toughness than those obtained by finite elements. However, although less variation is obtained in the fracture toughness, for different a/d values, than that obtained by equation 6.4 , the finite element results are not as good as those for the 100 mm cubes. The corresponding polynomial expression for the 150 mm cubes obtained from the finite element results is :-

$$k_1 = \frac{P}{B\,d^{\frac{1}{2}}} \left[30.5\,(a/d)^{1/2} - 612.0\,(a/d)^{3/2} + 4441.5\,(a/d)^{5/2} - 13404.8\,(a/d)^{7/2} + 14930.0\,(a/d)^{9/2} \right] \qquad (6.6)$$

6.4 Conclusions

The results shown in table 6.3 demonstrated that almost constant values of stress intensity factors may be obtained by the finite element method from the v-displacements at different points around the tip of the notch, using a small number (438) of degrees of freedom. The difference between the maximum and minimum estimates of k_1 for all a/d ratios was within 2% of the average value.

The results presented in this chapter generally demonstrate that, when the failure loads obtained experimentally are substituted in equation 6.4 , considerable variation in the fracture toughness, which is a material property, with the a/d ratio is obtained. The finite element analyses employing these loads, however, lead to improved results for fracture toughness. This improvement is more significant for the 100 mm cubes. Tables 6.6 and 6.7 give the difference between the maximum and minimum values for fracture toughness expressed as a percentage of the average of these values. It can be seen that, for the 100 mm cubes, the maximum difference obtained by finite elements is 10% while that obtained from equation 6.4 is 29% . If the finite element results can be trusted, an important conclusion made here is that equation 6.4 gives considerably overestimated values for fracture toughness. For example, if the results for the 150 mm cubes (table 6.7) are averaged, it can be seen that equation 6.4 gives a value which is 40% greater than the finite element estimate.

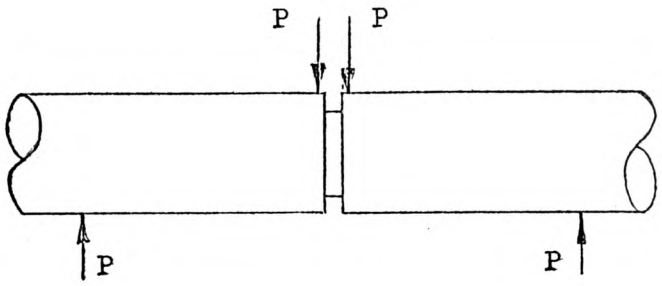

Figure 6.1 Circumferentially notched round bar subjected to four-point loading

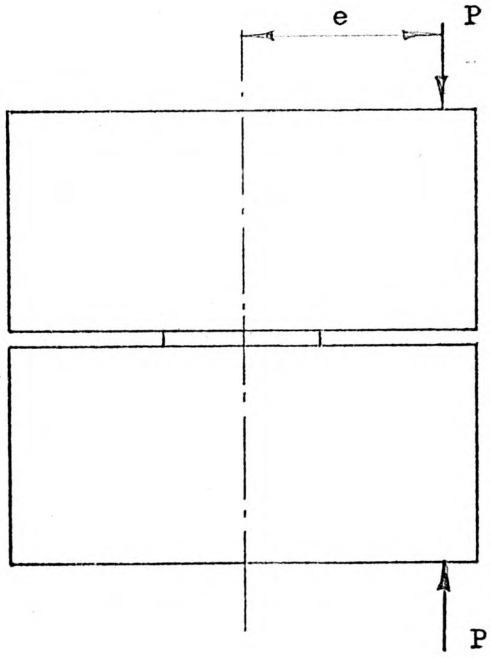

Figure 6.2 Circumferentially notched round bar subjected to eccentric longitudinal loading

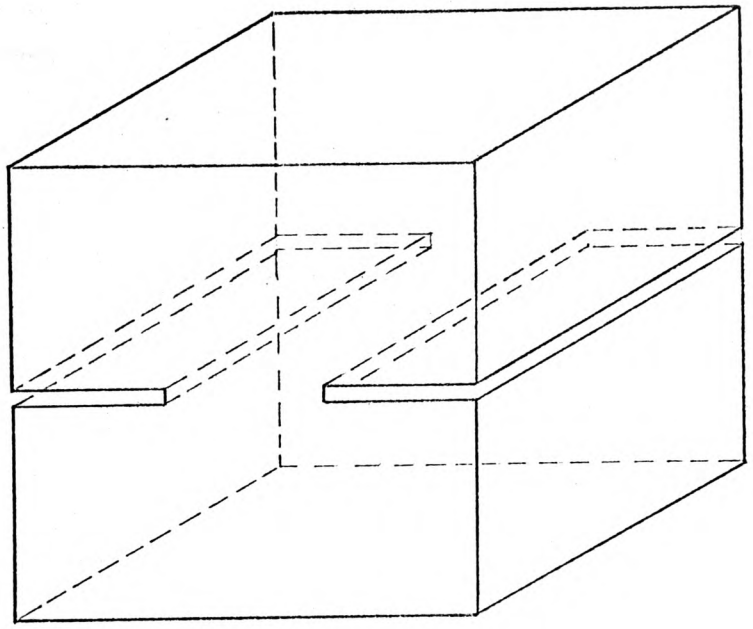

Figure 6.3 Concrete cube slit along two opposite faces

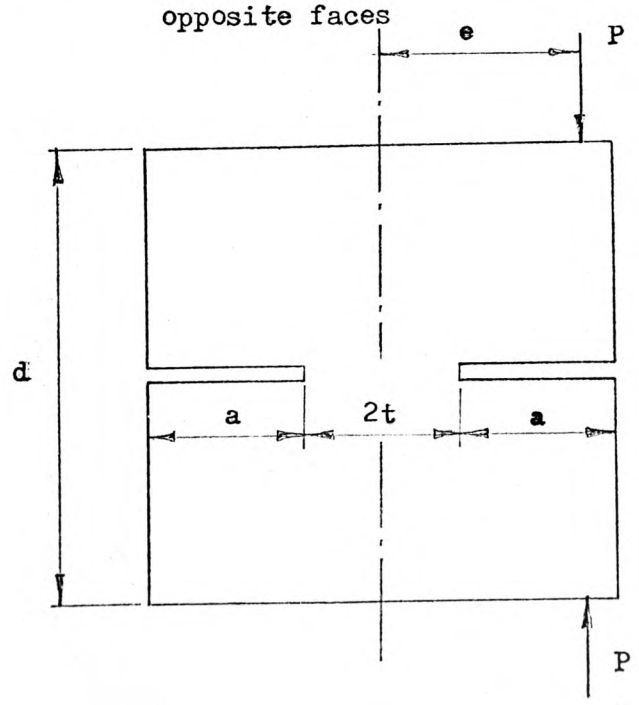

Figure 6.4 Loading arrangement

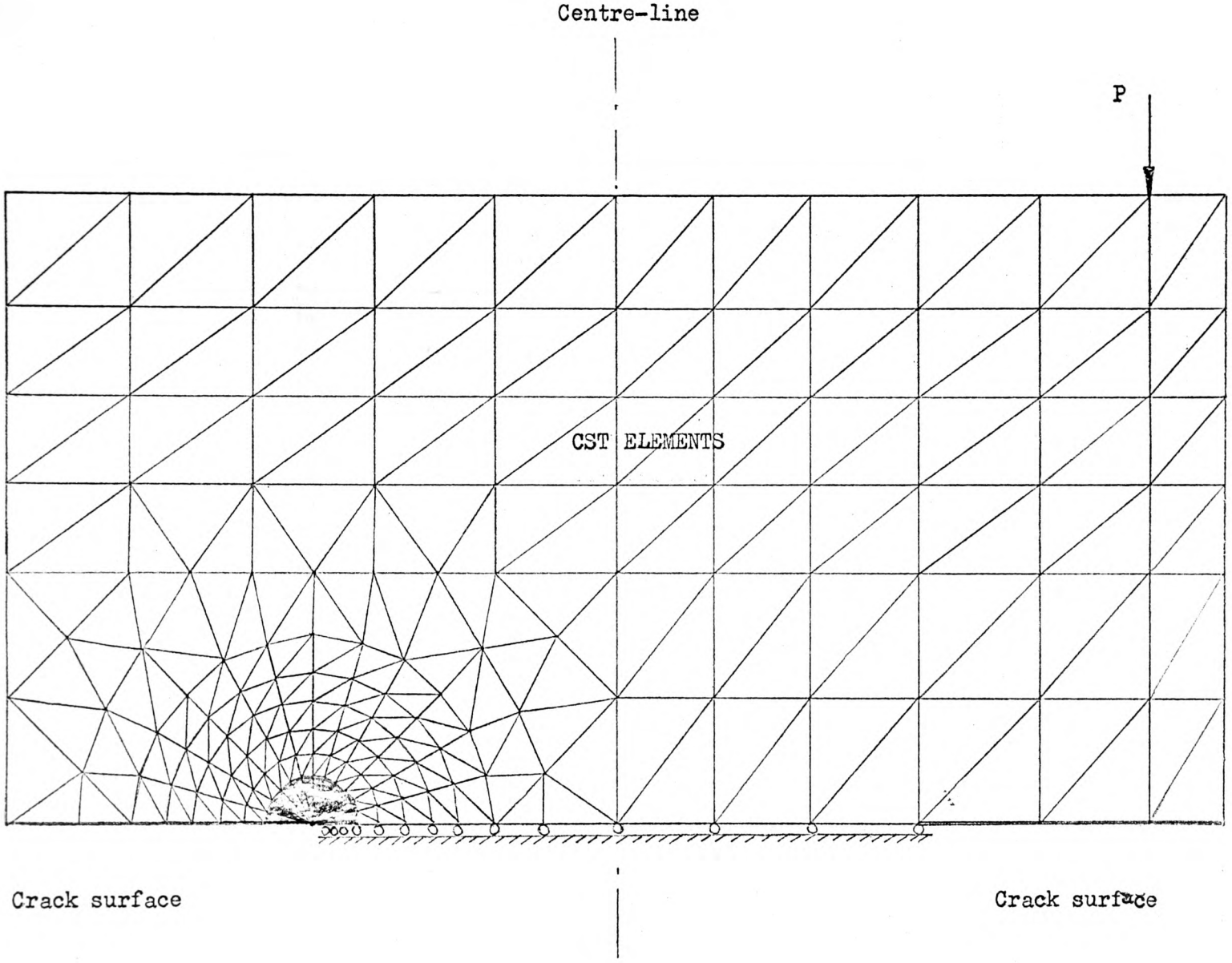

Figure 6.5 Finite element representation - split cube

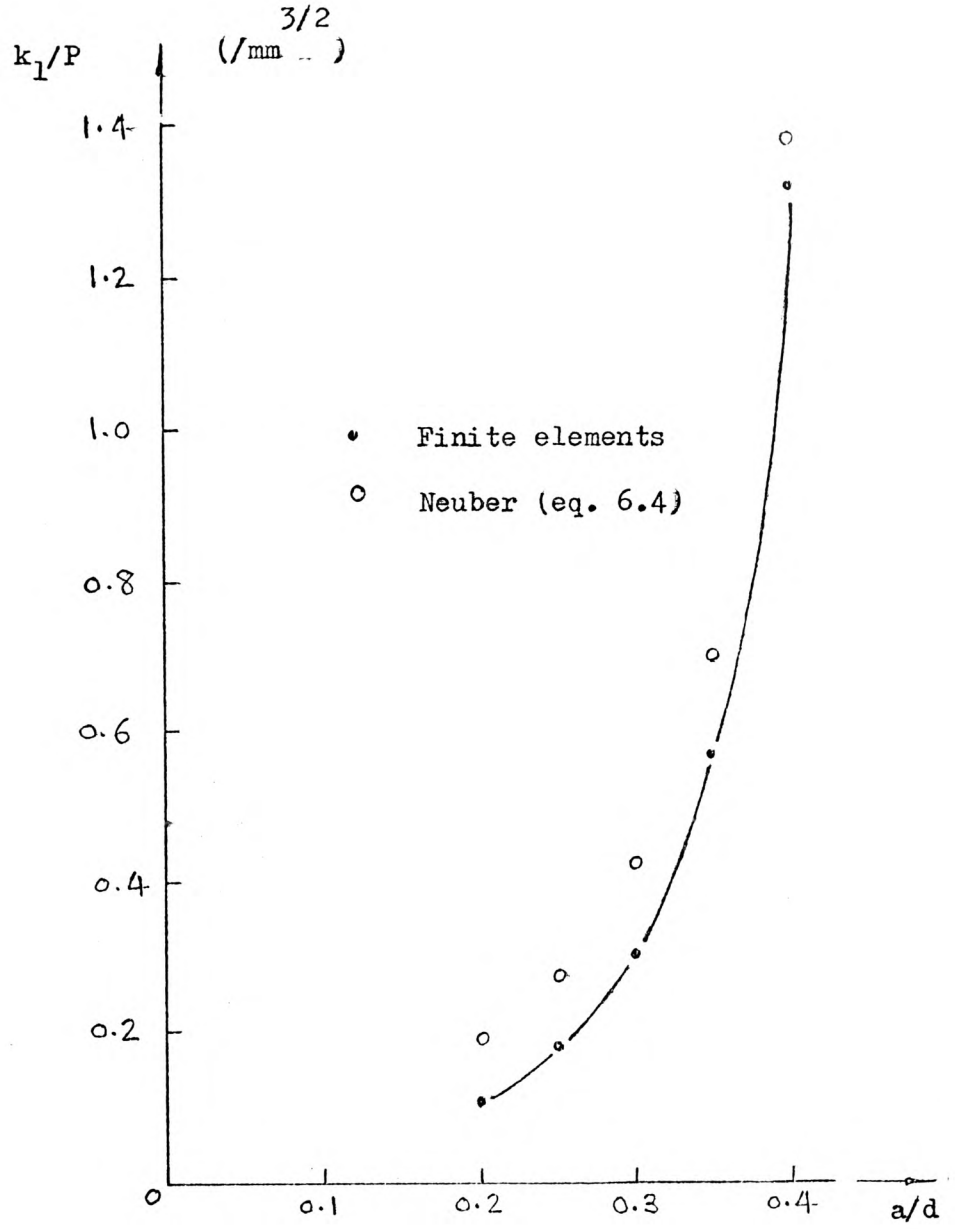

Figure 6.6 Comparison of results for the 100 mm split-cubes

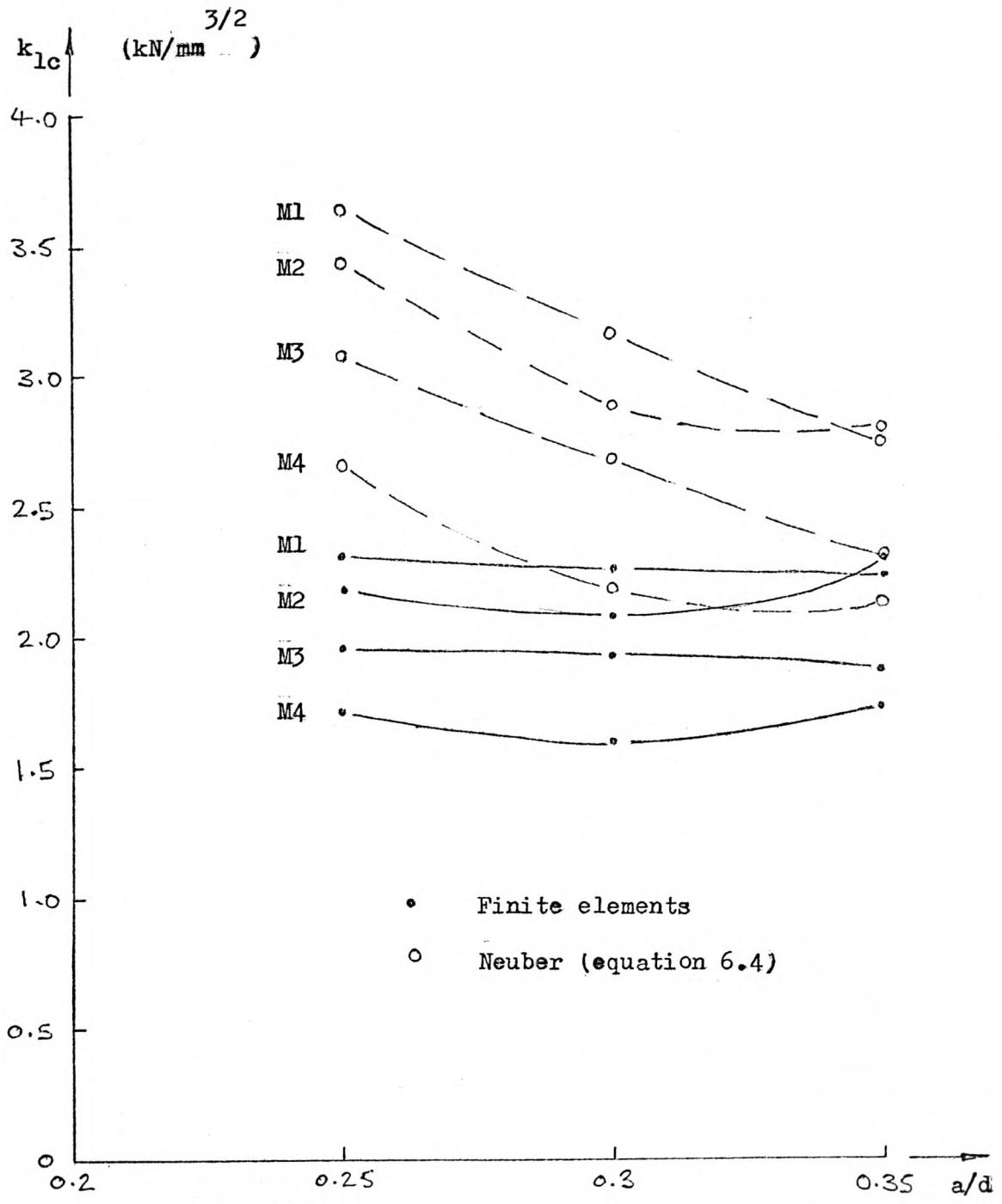

Figure 6.7 Variation of fracture toughness with notch-depth ratio for 100 mm split-cubes

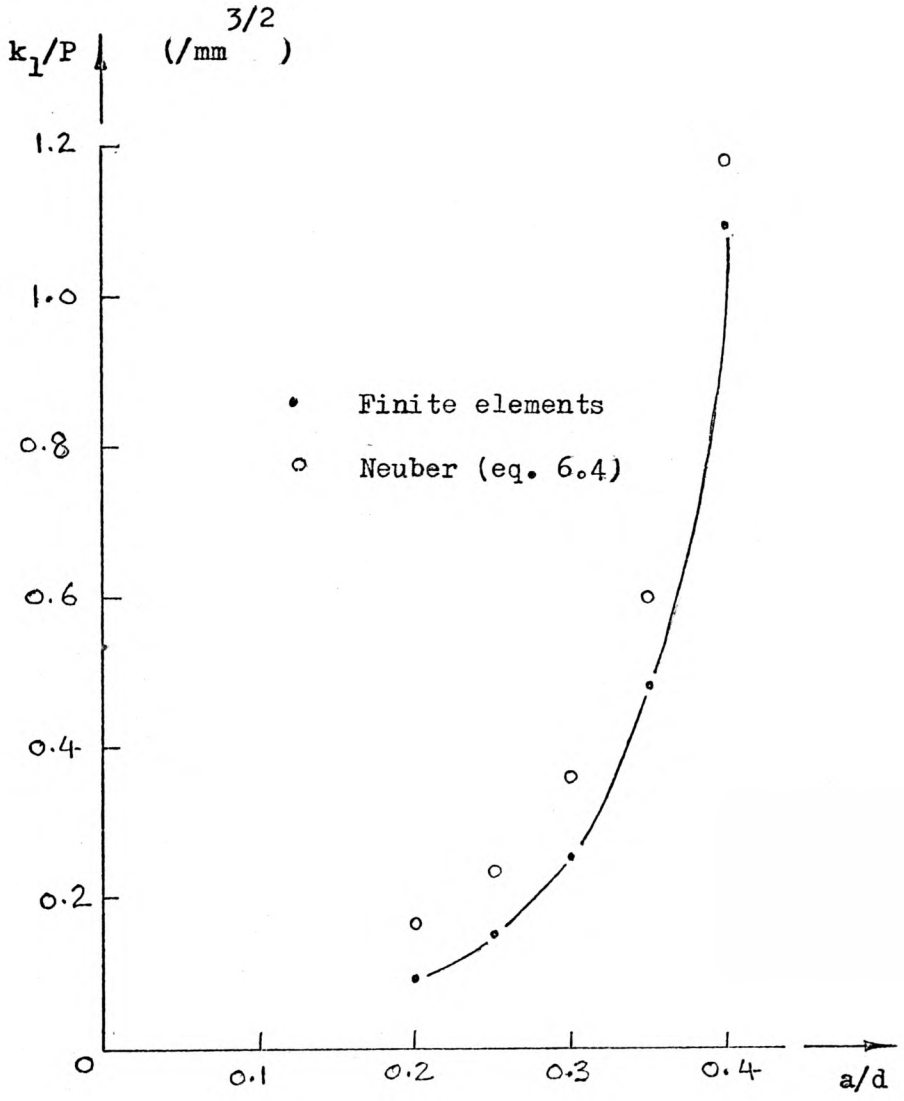

Figure 6.8 Comparison of results for the 150 mm split-cubes

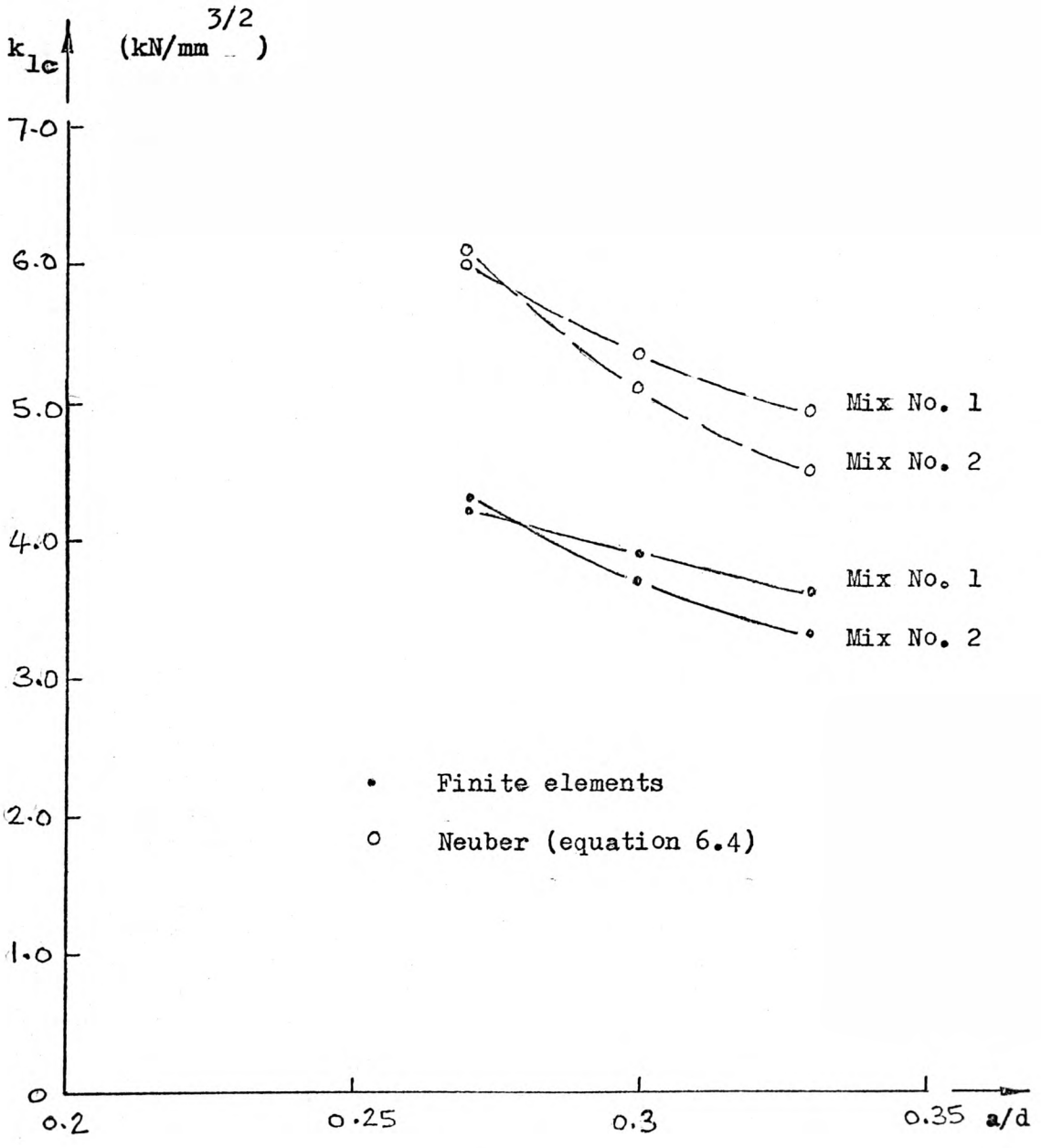

Figure 6.9 Variation of fracture toughness with notch-depth ratio for 150 mm split-cubes

Mix	W/C Ratio	Cube Strength N/mm^2	Nominal Notch Depth a (mm)		
			25	30	35
M1	0.40	62.5	13.28	7.52	3.96
M2	0.47	55.5	12.50	6.94	4.03
M3	0.53	52.5	11.23	6.45	3.30
M4	0.60	40.0	9.75	5.26	3.08

Table 6.1 Average values of loads at fracture (kN)

- 100 mm cubes

Mix NO.	W/C Ratio	Cube Strength N/mm^2	Nominal Notch Depth a (mm)		
			40	45	50
1	0.48	52.2	22.02	14.68	9.78
2	0.48	52.8	22.20	13.90	8.86

Mix Details :- Water = 12 kg Sand = 45 kg

Cement = 25 kg Aggregate = 70 kg

Table 6.2 Average values of loads at fracture (kN)

- 150 mm cubes

θ° \ a/d	0.20	0.25	0.30	0.35	0.40
0	10.38	17.10	29.26	56.16	130.68
15	10.38	17.10	29.26	56.11	130.62
30	10.39	17.11	29.27	56.09	130.58
45	10.40	17.14	29.31	56.13	130.60
60	10.44	17.19	29.38	56.22	130.64
75	10.48	17.24	29.44	56.35	130.62
90	10.52	17.30	29.55	56.53	130.57
105	10.56	17.36	29.63	56.71	130.39
120	10.58	17.39	29.61	56.86	134.00
135	10.58	17.38	29.55	56.89	129.27
150	10.53	17.28	29.34	56.66	128.03
165	10.41	17.06	28.94	56.03	120.13
Average	10.47	17.22	29.37	56.40	130.55
Max. % variation	1.9	1.9	1.3	1.5	2.0

Table 6.3 Stress intensity factors for 100 mm cubes

Mix	a/d					
	0.25		0.30		0.35	
	F.E.	Neuber	F.E.	Neuber	F.E.	Neuber
M1	2.32	3.64	2.26	3.16	2.24	2.75
M2	2.19	3.43	2.08	2.89	2.28	2.80
M3	1.97	3.08	1.94	2.69	1.87	2.29
M4	1.71	2.67	1.58	2.19	1.74	2.14

Table 6.4 Fracture toughness ($kN/mm^{3/2}$)

- 100 mm cubes

Mix No.	a/d					
	0.27		0.30		0.33	
	F.E.	Neuber	F.E.	Neuber	F.E.	Neuber
1	4.18	5.97	3.82	5.30	3.57	4.88
2	4.22	6.02	3.61	5.02	3.23	4.42

Table 6.5 Fracture toughness ($kN/mm^{3/2}$)

- 150 mm cubes

Mix	Neuber (equation 6.4)		Finite Elements	
	Average	% difference	Average	% difference
M1	3.20	28	2.28	4
M2	3.12	20	2.18	9
M3	2.69	29	1.92	5
M4	2.41	22	1.66	10

Table 6.6 Variation in fracture toughness values ($kN/mm^{3/2}$) - 100 mm cubes

Mix No.	Neuber (equation 6.4)		Finite Elements	
	Average	% difference	Average	% difference
1	5.43	20	3.88	15
2	5.22	30	3.73	26

Table 6.7 Variation in fracture toughness values ($kN/mm^{3/2}$) - 150 mm cubes

CHAPTER 7 APPLICATIONS TO MODE 2 PROBLEMS

Since the development, 25-30 years ago, of the basic fracture mechanics concepts, research in this area has been focused primarily on the opening mode 1 situation. Erdogan and Sih[48] were the first to examine a mixed mode situation in a plate containing a central inclined crack. The authors found that, under skew-symmetric plane loading of brittle materials, sliding or crack extension in its own plane does not take place, instead the crack grows in the direction perpendicular to the maximum tangential stress at the crack-tip. In spite of this fact it was shown that the fracture event could still be related to a critical value of the stress intensity factor.

Barr et al[34] used photoelastic techniques to predict fracture path for mixed mode problems using perspex and araldite materials. In addition to confirming the findings of Erdogan and Sih[48], the authors supported their results by a finite element solution, employing CST elements and an energy approach.

Although mixed mode problems have received some attention, very little information is available about the sliding mode 2 of fracture. The authors of reference 34 showed that a doubly slanted edge specimen could be produced for mode 2 testing. Rouhi[49] demonstrated this and carried out a number of photoelastic tests on perspex CR39 specimens. He found that the photoelastic pattern of the vertical crack-tips indicated that a dominating mode 2 deformation existed at the vicinity of the crack-tips. Fracture tests were performed[49] and k_{2c} values were obtained.

Chisholm et al[50] presented a boundary collocation solution for determining the mode 2 stress intensity factor for a pair of edge cracks in a finite isotropic plate. The solution was based on a stress function due to Williams[20]. The authors developed a compact shear specimen of Hysol epoxy resin which was loaded in a photoelastic experiment to study the isochromatic fringe patterns resulting from the crack-tip stress distribution. As in reference 49, the tests verified that a pure mode 2 stress distribution existed in the neighbourhood of the crack-tips. Although the basic geometry of the test specimens of Chisholm et al was the same as those of Rouhi, the latters specimen were more easily produced and tested.

In this chapter solutions for mode 2 problems using the finite elements developed in the present work together with CST elements are obtained. The results are compared to those of references 49 and 50.

7.1 Rectangular Specimen under a Uniformly Distributed Load

Rouhi[49] carried out a photoelastic study of cone cracks by testing rectangular CR39 specimens supported on a rigid base and loaded via a steel block simulating a uniformly distributed load. Two vertical cracks were inserted into the specimen's edge such that the loading block was just covering the distance between them. The specimen geometry and loading arrangement are shown in figure 7.1 . The author found that the crack-tip fringe pattern were identical to those obtained by Chisholm et al[50] for a compact shear specimen, thus ensuring that pure mode 2 state of stress existed. The photoelastic results were used to evaluate the shear stress distribution in the vicinity of the tip of the cracks.

The maximum in-plane shear stress may be written as :-

$$\tau_m = \left[\frac{(\sigma_y - \sigma_x)^2}{2} + \tau_{xy}^2 \right]^{\frac{1}{2}} \qquad (7.1)$$

By substituting for σ_x , σ_y and τ_{xy} from the Westergaard equations 2.1 and 2.2 , τ_m may be expressed in terms of k_1 and k_2 as follows :-

$$\tau_m = \frac{1}{2\,(2\pi r)^{\frac{1}{2}}} \left[(k_1 \sin\theta + 2\,k_2 \cos\theta)^2 + (k_2 \cos\theta)^2 \right]^{\frac{1}{2}} \qquad (7.2)$$

For the case of pure mode 2 evaluation, $\theta = 0$ and the above expression reduces to :-

$$k_2 = \tau_m (2\pi r)^{\frac{1}{2}} \qquad (7.3)$$

The photoelastic data and fringe patterns were used to evaluate maximum shear stress values at points at small distances ahead of the crack. A plot of k_2 against r could then be made by the use of equation 7.3 . Crack-tip stress intensity factors were then obtained by extrapolation to $r = 0$.

Due to the difficulty in measuring τ_m values at fracture using photoelasticity, k_{2c} values can not be found accurately from equation 7.3 . To alleviate this problem the use of an alternative expression for k_2 is made. This is :-

$$k_2 = k \tau (\pi a)^{\frac{1}{2}} \qquad (7.4)$$

where τ is the nominal shear stress acting on the crack-line and k is the stress intensity coefficient. Thus if the nominal shear stress τ could be measured, then k can be obtained by equating equations 7.3 and 7.4 . On substitution of the result for the nominal shear stress τ at fracture in equation 7.4, the resulting stress intensity factor should be k_{2c} , i.e. the critical mode 2 stress intensity factor. Such an evaluation of the nominal shear stress is possible using a simple analytical solution[10] , which is briefly discussed in the following section.

7.1.1 Concentrated Load at a Point of a Straight Boundary

Consider a concentrated vertical force P acting on a horisontal straight boundary of an infinitely large plate as shown in figure 7.2 . If the distribution of the load across the thickness of the plate is uniform, then a basic solution for this problem is that given in reference 10, which assumes a simple radial distribution.

Any element C at a distance r from the point of application of the load is subjected to simple compression in the radial direction. In terms of polar co-ordinates, the stresses are :-

$$\sigma_r = \frac{-2P\cos\theta}{\pi r} \quad , \quad \sigma_\theta = \tau_{r\theta} = 0 \tag{7.5}$$

Taking a circle of any diameter d with centre on the x-axis and tangent to the y-axis at O , we have, for any point C on the circle, $d\cos\theta = r$. Hence from equations 7.5 we have :-

$$\sigma_r = \frac{-P}{\pi d} \tag{7.6}$$

which means that the stress is the same at all points on the circle, except the point O, the point of application of the load.

Taking a horizontal plane mn at a distance W from the straight boundary, the normal and shearing stress components on this plane at any

point M are calculated from the compression in the radial direction. Thus,

$$\sigma_x = \sigma_r \cos^2\theta = \frac{-2P}{\pi W} \cos^4\theta \qquad (7.7)$$

$$\sigma_y = \sigma_r \sin^2\theta = \frac{-2P}{\pi W} \sin^2\theta \cos^2\theta \qquad (7.8)$$

$$\tau_{xy} = \sigma_r \sin\theta \cos\theta = \frac{-2P}{\pi W} \sin\theta \cos^3\theta \qquad (7.9)$$

The nominal shear stress τ appearing in equation 7.4 is evaluated from equation 7.9 . The above solution could be extended to the case of the uniformly distributed load considered in the next section by the principle of superposition.

7.1.2 The Finite Element Results

Plain strain finite element solutions for a rectangular specimen with two edge cracks subjected to uniform compression were obtained. The dimensions of the specimen and load configuration are shown in figure 7.3 . These were the same as those considered by Rouhi[49] in his photoelastic tests. Several crack depths were considered giving a range of a/W ratios. Due to symmetry about the centreline, only one half of the plate was analysed. For brevity, the details of only one of the meshes employed in the left hand side halves of the plates is given. This is shown in figure 7.4 for the case where a/W = 0.375 . The region within $r = \frac{a}{60}$ surrounding the tip of the crack was covered by elements I and II, the remainder of the plate being represented by CST elements. This representation contained 589 elements and 337 nodal points giving a total of 674 degrees of freedom. In order that results of similar accuracy are obtained from all analyses, the meshes employed for the other crack depths had a total number of degrees of freedom approximately the same as that for the mesh shown in figure 7.4 .

Mode 2 stress intensity factors were computed from the finite element results by averaging the values near the crack-tip, obtained from the u-displacements. The nominal shear stress along the line containing the crack was calculated using equation 7.9 . This enabled a direct comparison to be made between the finite element results and those obtained photoelastically by Rouhi. In the finite element solution the uniformly distributed load was simulated by seven equivalent point loads as shown in figure 7.3 . The shear stress along the section containing the crack due to the action of these loads were calculated at a number of points

as shown in figure 7.5 . The average values of the shear stresses per unit thickness along section AA were calculated for P = 1.0 . The results are presented in table 7.1 , where the average shear stress for specimens of up to 40 mm in depth can be obtained.

A comparison between the finite element results and those obtained in reference 49 are shown in figure 7.6 . The finite element results show that increasing the value of poisson's ratio from 0.2 to 0.38 leads to approximately 4% increase in the values of the stress intensity coefficient k . For ν = 0.38 and for the range of a/W ratios considered, the finite element results may be expressed by the following equation :-

$$k_2 = 0.81 \tau (\pi a)^{\frac{1}{2}} \qquad (7.10)$$

If τ can be expressed as P/at, where t is the thickness of the specimen, then equation 7.10 may be written as :-

$$k_2 = 1.44 \frac{P}{t a^{\frac{1}{2}}} \qquad (7.11)$$

7.2 The Compact Shear Specimen of Chisholm et al

Chisholm et al[50] developed a compact shear specimen of Hysol epoxy resin which was pin loaded in shear in a photoelastic experiment. The specimen contained two edge cracks, making it similar to that used in reference 49. A schematic diagram of the test specimen is shown in figure 7.7 . By evaluating the maximum shear stress at points near the crack-tip and along the line of the crack, it was possible to obtain mode 2 stress intensity factors using equation 7.3 . It was found[50], when evaluating the maximum shear stress, that lines drawn to the extrema of the isochromatics were mostly within 0.5^{o} of the direction of the crack. For this angle of deviation, the authors state that k_2 values were approximately 60 times larger than those of k_1 , thus verifying that a state of essentially pure shear existed at the crack-tips.

Finite element solutions were obtained for this problem under plain strain conditions. The dimensions of the specimen, which were approximately the same as those of reference 50 , are shown in figure 7.8 . Again, several crack depths were considered giving a range of a/W ratios. Because of symmetry about the centreline only one half of the plate was considered. The pin loads were simulated by point loads as shown in figure 7.8 . The finite element meshes were similar to those used in the previous section and had a total number of degrees of freedom ranging between 674 and 680 .

The boundary collocation solution obtained in reference 50 was expressed by the following equation :-

$$k_2 = \frac{P W^{\frac{1}{2}}}{t h} \left(\frac{a}{W}\right)^{\frac{1}{2}} = \sigma a^{\frac{1}{2}} \qquad (7.12)$$

where $\sigma = P/th$ and t is the thickness of the specimen. Equation 7.12 is valid to within 2% for $0.3 < a/W < 0.7$.

Figure 7.9 gives a comparison between the results of reference 50 and the finite element results.

7.3 Conclusions

The finite element programme developed in chapter 5 was used to obtain stress intensity factors for mode 2 problems. For the rectangular edge-cracked specimen under uniform compression, and for the range of a/W ratios considered, the finite element analysis give an estimate for the stress intensity coefficient of approximately 0.81 , see figure 7.6 . The photoelastic results of reference 49 give an estimate for this coefficient of approximately 0.9 . The difference between the results may be attributed to the following factors. In reference 49, when calculating the nominal shear atress, the uniformly distributed load was simulated by five equivalent point loads, whereas in the finite element analysis, seven point loads, i.e. four on half the plate, were used. The test pieces of reference 49 were approximately 5 mm thick, this may not have been thick enough to develop the plain strain conditions assumed in the finite element solution. Furthermore, the results show that the influence of increasing the value of poisson's ratio from 0.2 to 0.38 appear to be quite significant, and hence part of the difference may be attributed to the choice of this value for the material tested.

Figure 7.9 give the results for the compact shear specimen of Chisholm et al[50]. Here the difference between the results is considered to be largely due to the different boundary conditions imposed along the centreline of the specimen. In the finite element solution the centreline was restrained against movement in the horizontal direction, whereas a linear stress distribution along this line was assumed in reference 50. Some of the points raised above may also be partly responsible for the

difference in the results. Taking account of these points, it may be c considered that reasonable agreement was obtained between the finite element results and those obtained by experiments.

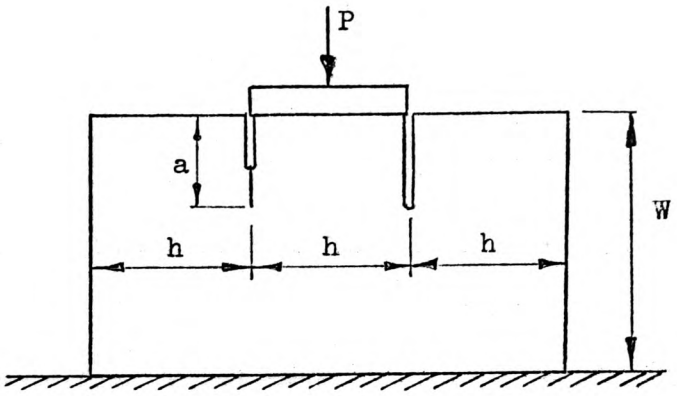

Figure 7.1 Rectangular shear specimen - reference 49

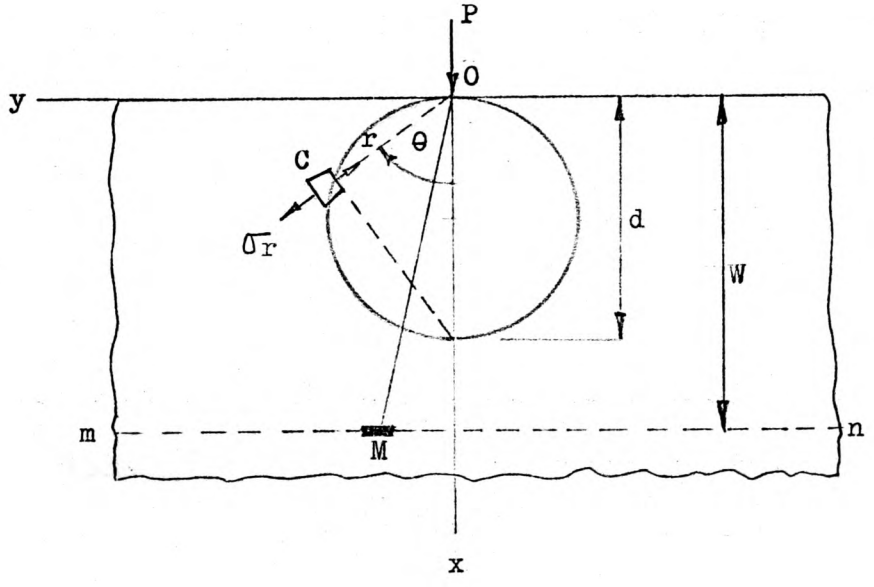

Figure 7.2 Concentrated load at a point of a straight boundary - reference 10

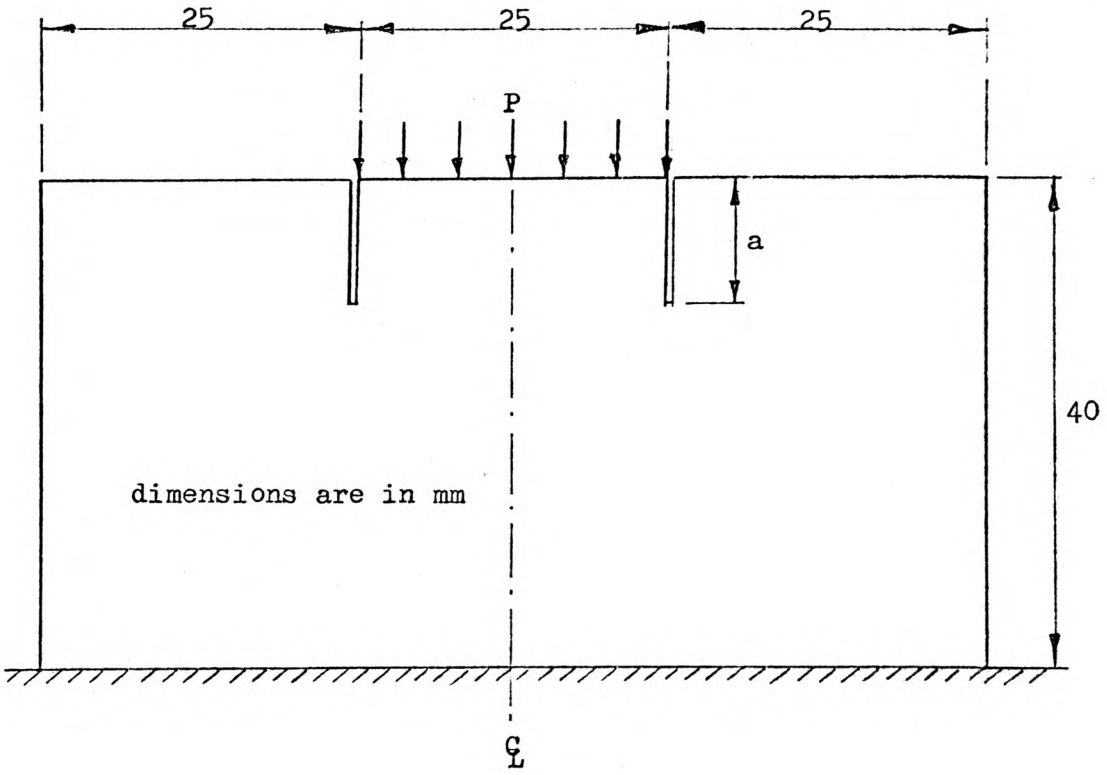

Figure 7.3 Shear specimen used in the finite element solution

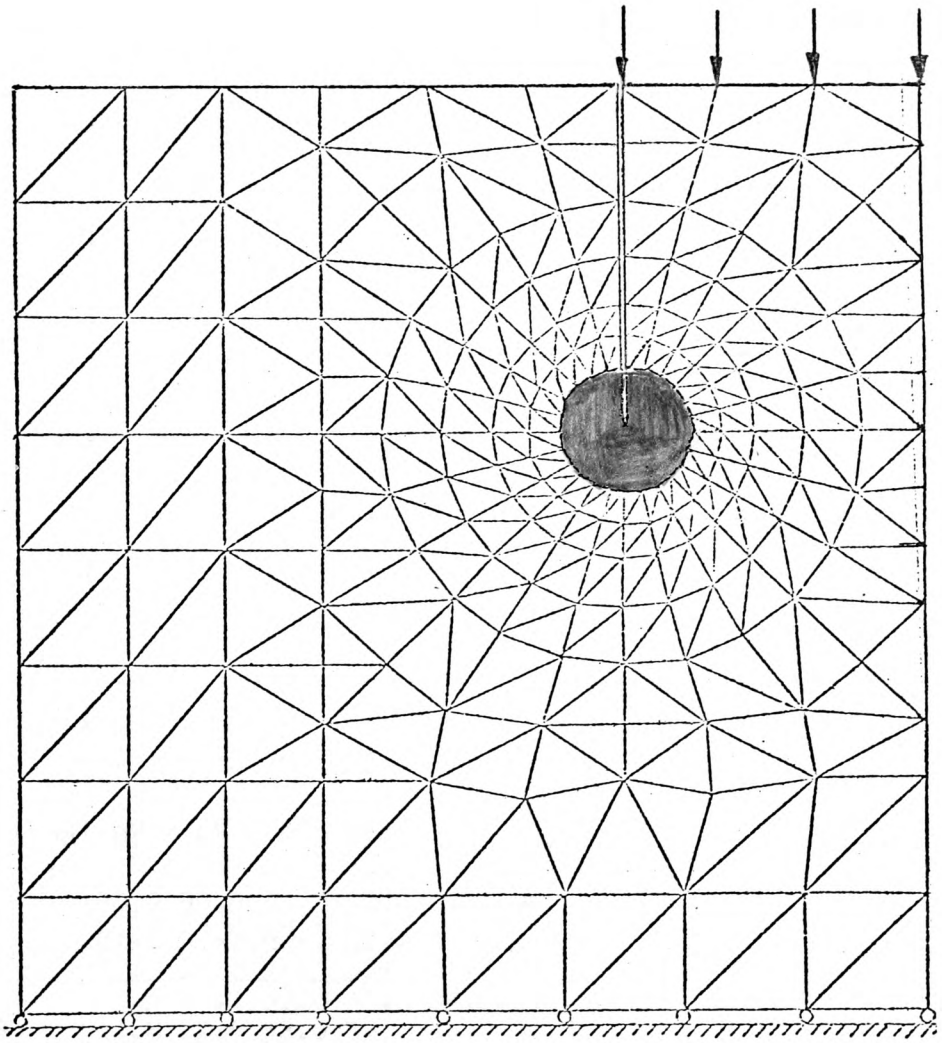

The shaded region contained 24 elements II, 48 elements I and 190 CST elements.

Figure 7.4 Finite element mesh for the shear specimen shown in figure 7.3

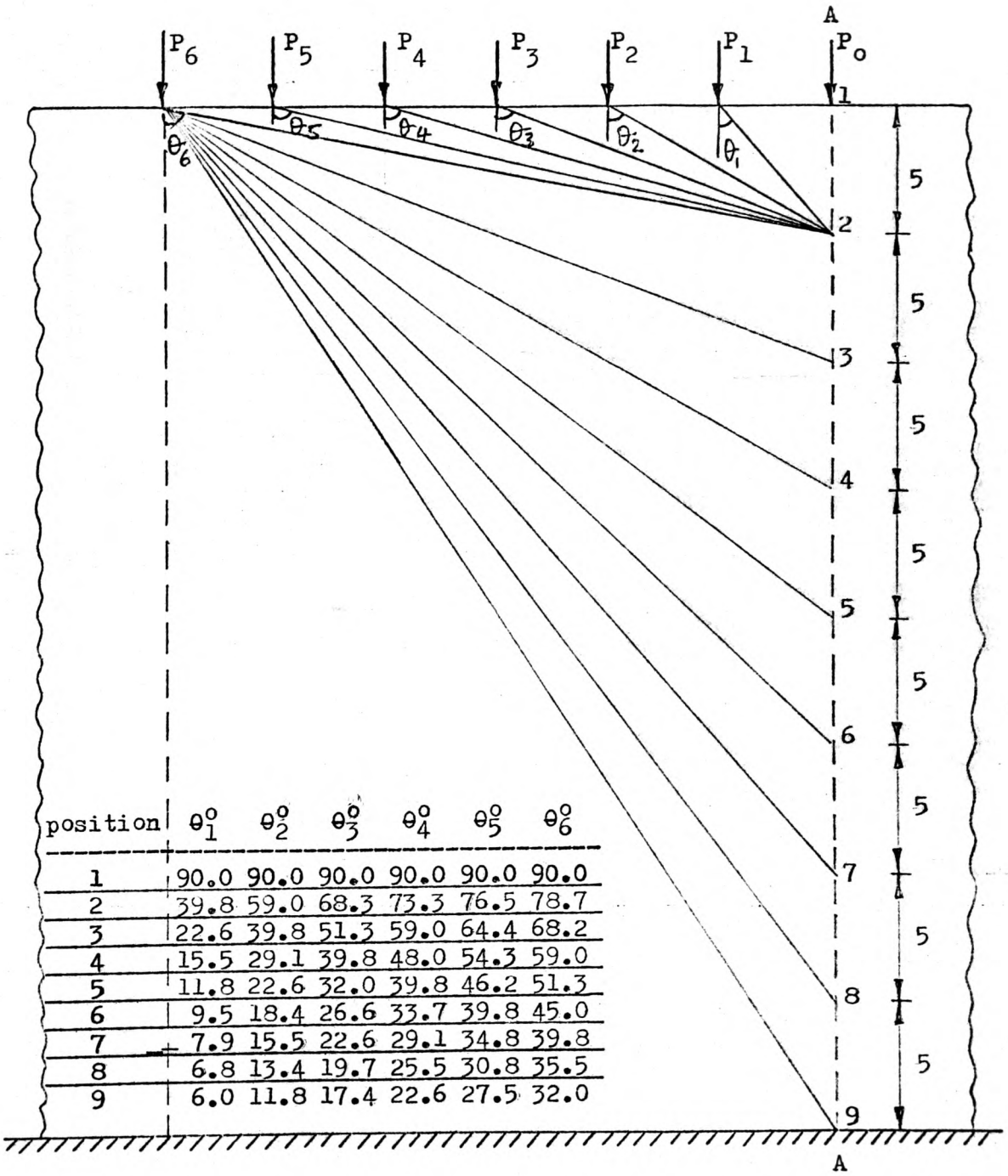

position	θ_1^o	θ_2^o	θ_3^o	θ_4^o	θ_5^o	θ_6^o
1	90.0	90.0	90.0	90.0	90.0	90.0
2	39.8	59.0	68.3	73.3	76.5	78.7
3	22.6	39.8	51.3	59.0	64.4	68.2
4	15.5	29.1	39.8	48.0	54.3	59.0
5	11.8	22.6	32.0	39.8	46.2	51.3
6	9.5	18.4	26.6	33.7	39.8	45.0
7	7.9	15.5	22.6	29.1	34.8	39.8
8	6.8	13.4	19.7	25.5	30.8	35.5
9	6.0	11.8	17.4	22.6	27.5	32.0

Figure 7.5 Load distribution for calculating average shear stress along crack-line (reference 10)

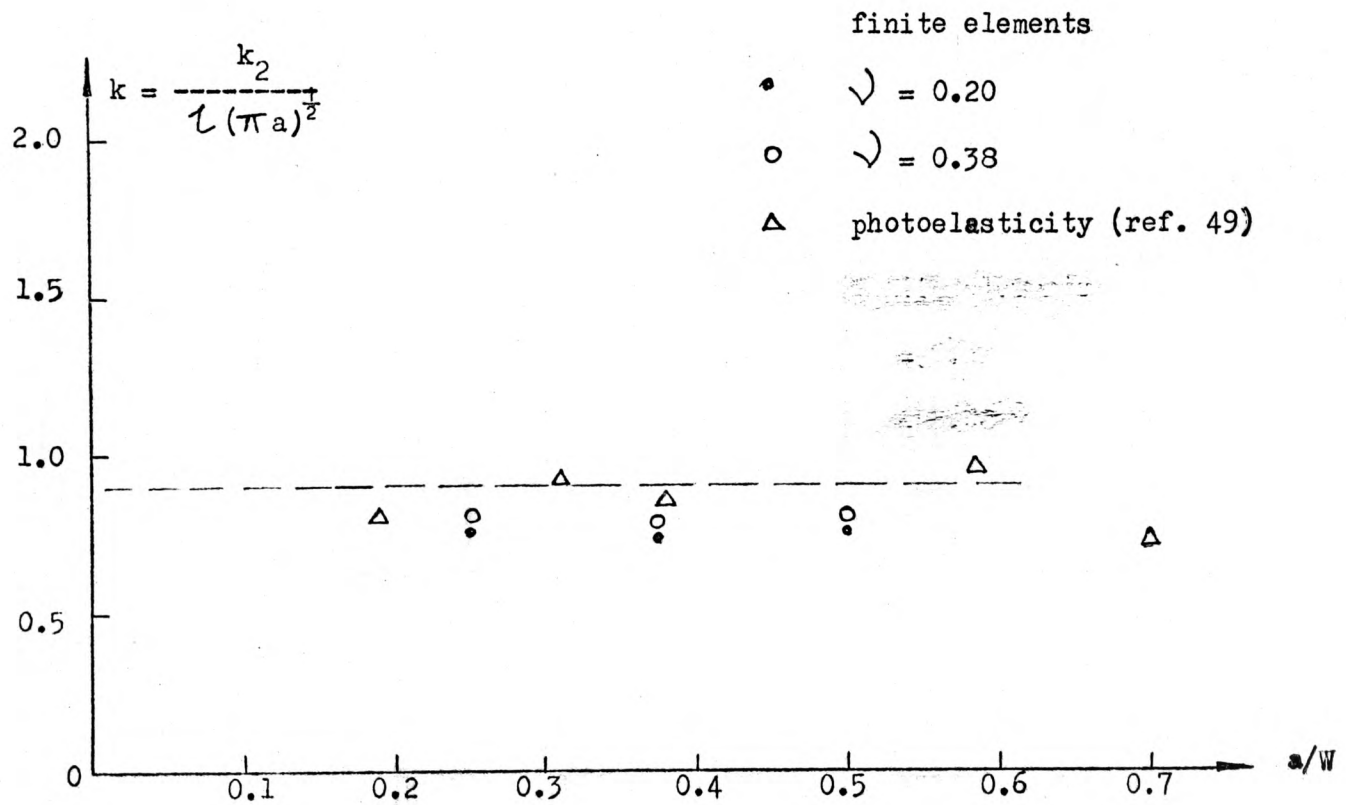

Figure 7.6 Comparison between the finite element results and the photoelastic results of reference 49 .

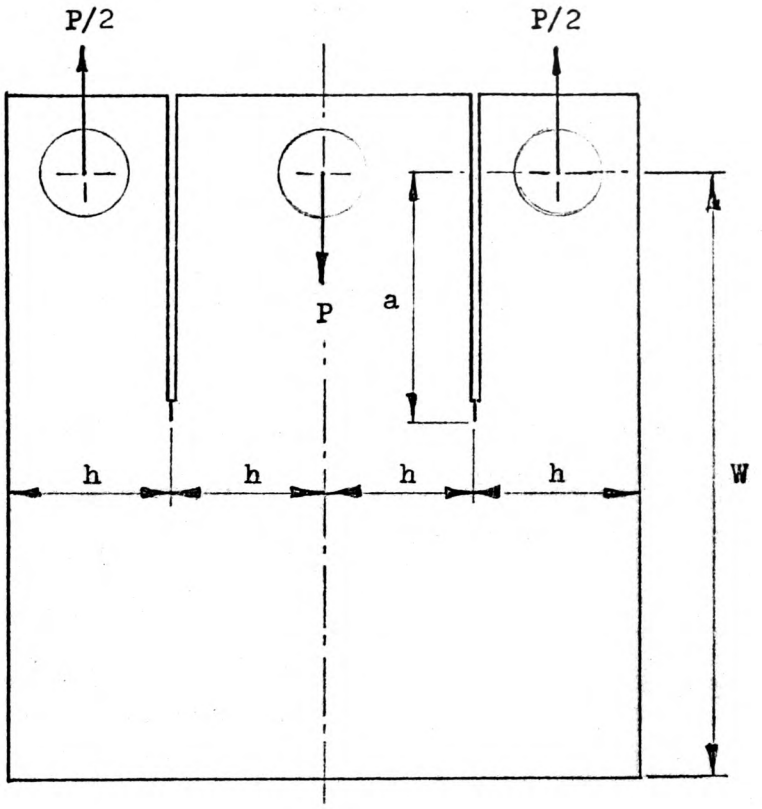

Figure 7.7 The compact shear specimen of Chisholm et al[50]

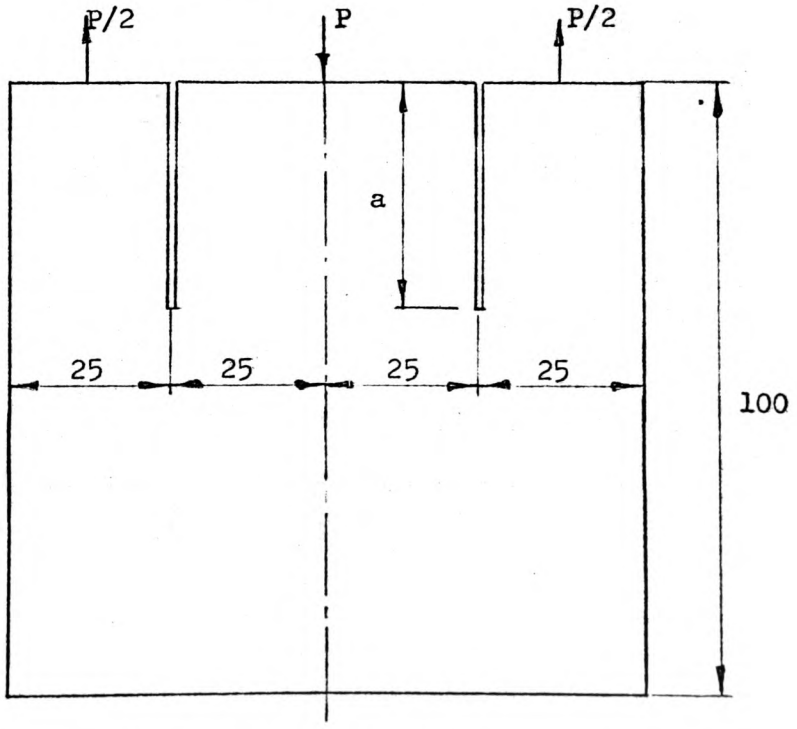

dimensions are in mm

Figure 7.8 Compact shear specimen used in the finite element analysis

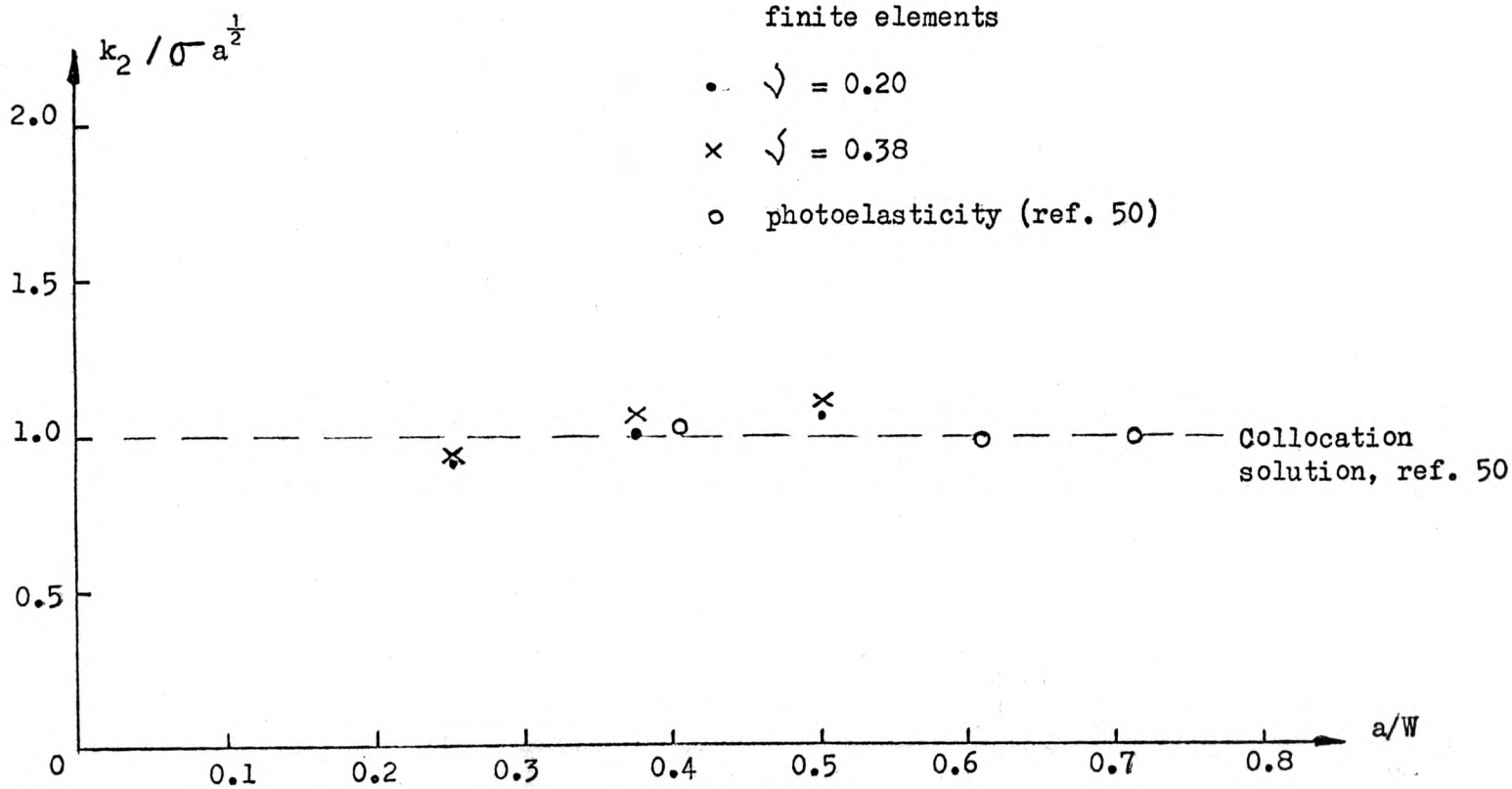

Figure 7.9 Results for the compact shear specimen

depth W (mm)	section	shear stress τ_{xy} x10^{-4} (N/mm^2)							
		P_1	P_2	P_3	P_4	P_5	P_6	total	total ave.
0	1	0	0	0	0	0	0	0	0
5	2	61.59	24.78	10.09	5.04	2.63	0.79	104.9	52.5
10	3	32.10	30.79	20.20	12.39	8.55	2.52	106.5	70.5
15	4	16.93	22.95	20.53	15.74	11.45	4.13	91.7	75.8
20	5	10.15	16.05	17.15	15.40	12.71	5.05	76.5	75.9
25	6	6.70	11.46	13.58	13.56	12.32	10.61	68.2	74.7
30	7	4.73	8.47	10.70	11.47	11.18	5.13	51.7	71.4
35	8	3.51	6.46	8.52	9.59	9.84	4.75	42.6	67.8
40	9	2.71	5.08	6.88	8.02	8.55	4.29	35.0	64.1

Table 7.1 Average shear stress at various depths along section AA of figure 7.5

CHAPTER 8 CONCLUSIONS AND FUTURE WORK

In the two dimensional analysis of cracked structures by the finite element method, the use of conventional elements in the vicinity of the crack-tip requires a large number of elements in order that reasonable accuracy is obtained. This is due to the steep gradients of the strains near the crack-tip. For simple geometries and loading conditions, as many as 2000 degrees of freedom are necessary. The resulting large number of simultaneous equations to be solved leads to large computer storage and solution time requirements. In order to avoid the need for a highly refined element representation near the crack-tip, more efficient finite elements are needed. Two such elements, namely I and II, were developed in chapter 4. These elements were based on displacement functions closely represent the character of the strains near the crack-tip.

The first element, I, is 'tapezoidal' in shape with two straight and two curved boundaries. Two degrees of freedom, namely u and v, are allowed at each node giving a total number of degrees of freedom of eight for the element. The size of the resulting element stiffness matrix is therefore (8 x 8) . This element was based on displacement functions, equations 4.24 and 4.25 , derived from simple strain functions, equations 4.15 , embedding the singularities associated with the crack-tip region, by integrating the strain - displacement equations. The resulting displacement functions contain terms associated with the rigid body modes.

The second element, II, is 'triangular' in shape with two straight boundaries, meeting at the tip of the crack, and the other circular. This element was based on simple assumed displacement functions, equations 4.35 and 4.36 . The size of the stiffness matrix for this element is (4 x 4) .

Both elements were derived in terms of polar co-ordinates. A close look at the strain functions for the two elements, i.e. equations 4.26 - 4.28 and 4.37 - 4.39 , will indicate that the strains on the two elements vary in an identical manner with respect to r and θ . Although the displacements for the two elements are continuous only at the nodal points, it is argued that, excepting the rigid body terms, as the radius of the tip elements decrease indefinitely, continuity at the interface will be approached in the limit.

An assessment of the effectiveness of these elements was made by analysing two problems for which 'exact' solutions are available. In the two examples solved, a semi-infinite crack in an infinite plane was analysed by considering a finite circular region centred at the crack-tip. Both mode 1 and mode 2 situations were studied. Using as few as 312 degrees of freedom, accuracies for displacements and stresses within 1.5% and 3% , respectively, were generally obtained for points near the crack-tip. In general the accuracy of the results were the same whether mode 1 or mode 2 conditions were considered. The inclusion of the rigid body terms in the displacement functions may be partly responsible for the generally high degree of accuracy obtained.

The above work established the validity of the new elements in the singular domain in a cracked structure. In a real situation, the singular region is confined to a small area of the cracked plate surrounding the crack-tip. More conventional elements are required for the remaining major part of the plate. Such an element is the constant strain triangular (CST) elements of reference 4 . A new finite element programme, based on that of Coughlan[41] , was written. This programme employs elements I and II together

with CST elements. The validity of this programme was established by analysing a plate with a single edge crack previously considered in reference 19 .

Several problems, of the type used in fracture toughness testing, were analysed in chapter 5 . The initial results demonstrated that, when used with CST elements, elements II alone were not capable of assuming a small size of the order of the size of the singular region of the crack-tip. Significant improvement in the results were obtained when elements II, surrounding the tip of the crack, were supplemented by a ring of elements I. Using a small number of degrees of freedom, e.g. 450 , values of stress intensity factors accurate to within 3% were obtained by simple averaging near the crack-tip. In this way the need for an extrapolation process was obviated. A study of the results in the vicinity of the crack-tip gave an estimate of the size of the singular region which was approximately half that suggested by Kobayashi et al[11] .

The results for the split concrete cubes presented in chapter 6 demonstrated that, using 438 degrees of freedom, almost constant values of stress intensity factors were obtained from the v-displacements at different points around the tip of the notch. Table 6.3 shows that the difference between the maximum and minimum estimates of k_1 for all the a/d ratios considered was within 2% of the average value. Using these results, expressions for the stress intensity factors as functions of a/d were obtained for both 100 mm and 150 mm cubes. These are given in equations 6.5 and 6.6 , respectively, and are accurate to within 2% of the finite element results.

Fracture toughness values were determined using the fracture loads obtained experimentally[45]. It was shown that the use of an equation based on the work of Neuber[46], i.e. equation 6.4 , lead to considerable variation in the fracture toughness with the a/d ratio. The finite element analyses employing the fracture loads gave improved results, particularly for the 100 mm cubes. If the finite element results can be trusted, an important conclusion made here is that equation 6.4 gives considerably overestimated values of fracture toughness, as shown in figures 6.7 and 6.9 . The improvement was not so significant in the case of the 150 mm cubes. As fewer tests employing 150 mm cubes were performed[45], it is suggested that a desirable future investigation is a further testing programme employing 150 mm cubes. The results of such tests may consolidate those for the 100 mm cubes, and hence would establish more confidence in the use of the expressions developed in the present work, i.e. equations 6.5 and 6.6 . In the experimental arrangement, irrespective of the size of the cube being tested, the load was always placed at 6 mm from the edge. This resulted in the load having different eccentricities from the centreline of the cube. An interesting future investigation is the study of the influence of this eccentricity on the values of fracture toughness.

In chapter 7 , doubly edge-cracked rectangular specimens were analysed under mode 2 conditions. Taking account of the points made in section 7.3, it is considered that the finite element results, using 674 degrees of freedom, were in reasonable agreement with the photoelastic test results of references 49 and 50. The finite element results were used to obtain an expression for the stress intensity factor k_2 , for the uniformly

loaded specimen of reference 49, in terms of the load, thickness and crack size. It may be argued that a more refined element representation is necessary for this type of problem. To investigate this possibility, convergence studies are required. Because of the limitations on the computer storage allocation it is not possible to carry out this study at present. However this is left as a part of a future programme of study into cone cracks and possible fracture path prediction using an energy approach outlined in reference 34 . This approach entails the calculation of the strain energy for a series of crack extensions in different directions. The fracture path being the direction resulting in a maximum value of the strain energy release.

The results presented in this thesis demonstrated that CST elements can be effectively combined with elements I and II, developed here, for the analysis of cracked structures. Other elements, such as isoparametric elements, may prove to be even more effective and this is considered as an interesting area of future application. On the development side, a future area of study is to look into the possibility of devising new finite elements for the region away from the singular domain using the approach used in chapter 4 .

APPENDIX

Computation Methods and Computer Programmes

The available methods for the solution of the large number of linear algebraic equations, resulting from a finite element analysis, can be divided into either direct or iterative approaches. In the direct approach a solution is assured after the completion of a number of arithmetical operations. The iterative approach involves a guess for the solution and subsequent improvement by a series of iterations until the desired accuracy is achieved. The programmes used in the present investigation employ the direct method of solution.

Gaussian elimination procedure represents the most economical direct method for dealing with the system of matrices encountered. This procedure, for a fully populated matrix in which all the terms are stored and operated upon, may be illustrated in the following two ways.

1. Let the system of equations whose solution is required be represented by the matrix equation

$$K_{nn} \; \delta_n = P_n \qquad (1)$$

where K_{nn} is the structure stiffness matrix of order (n x n), δ_n is the vector of nodal displacements and P_n is the load vector. The size of the matrix K_{nn} can be reduced by one if we partition K_{nn} in the following way

$$\begin{bmatrix} K_{ii} & K_{ij} \\ K_{ji} & K_{jj} \end{bmatrix} \begin{bmatrix} \delta_i \\ \delta_j \end{bmatrix} = \begin{bmatrix} P_i \\ P_j \end{bmatrix} \qquad (2)$$

where K_{ii} is a matrix of order $(n - 1)$ and K_{jj} is the diagonal element corresponding to the nodal displacement whose elimination is required. The above system of equations can be treated as two sets and δ_j can be eliminated, so that equation 2 becomes

$$K_{n-1,n-1} \quad \delta_{n-1} = P_{n-1} \qquad (3)$$

where $$K_{n-1,n-1} = K_{ii} - K_{ij} \; K_{jj}^{-1} \; K_{ji}$$

and $$P_{n-1} = P_i - K_{ij} \; K_{jj}^{-1} \; P_j$$

This forward elimination procedure can be repeated by partitioning K_{n-1} in the same way until it is reduced to a (1 x 1) matrix where a solution for the last displacement is obtained by direct division. Back substitution may then be made to solve for the remaining displacements.

2. A second way of illustrating the Gaussian elimination method as applied to the matrix equation 1 is obtained by writing it as

$$\begin{bmatrix} a_{11} & a_{12} & a_{13} & \cdots\cdots & a_{1n} \\ a_{21} & a_{22} & a_{23} & \cdots\cdots & a_{2n} \\ a_{31} & a_{32} & a_{33} & \cdots\cdots & a_{3n} \\ \cdot & \cdot & \cdot & & \cdot \\ \cdot & \cdot & \cdot & & \cdot \\ \cdot & \cdot & \cdot & & \cdot \\ \cdot & \cdot & \cdot & & \cdot \\ \cdot & \cdot & \cdot & & \cdot \\ a_{n1} & a_{n2} & a_{n3} & \cdots\cdots & a_{nn} \end{bmatrix} \begin{bmatrix} S_1 \\ S_2 \\ S_3 \\ \cdot \\ \cdot \\ \cdot \\ \cdot \\ \cdot \\ S_n \end{bmatrix} = \begin{bmatrix} P_1 \\ P_2 \\ P_3 \\ \cdot \\ \cdot \\ \cdot \\ \cdot \\ \cdot \\ P_n \end{bmatrix} \qquad (4)$$

where the a's represent the terms of the matrix K_{nn} . Element a_{21} is reduced to zero, changing the values of the elements of the second row, by multiplying the second row by a_{11}/a_{21} and subtracting the first row from it. A series of such operations are carried out to reduce all the non-zero terms in the first column, below a_{11} , to zero. Further operations can be carried out to reduce the terms of the second column, below element a_{22} , and so on until we end with an upper triangular matrix of which the last row has only one unknown. This procedure is called 'triangulization' . At the same time, the same operations are performed on the load vector P_i . It is then possible to obtain values for the last unknown and the remaining solution for the displacements by back-substitution.

The above procedures represent the simples direct methods in which all the terms of the structure stiffness matrix are stored and operated

upon. Structural stiffness matrices are , however, not fully populated and are commonly strongly banded about the leading diagonal. Also, the symmetry of the matrices allows the computations to be confined to the upper half band only.

The finite element results presented in this thesis were obtained from two programmes, both coded in FORTRAN IV . As details of the basic versions are given in the literature[4,51] , only a general description and an outline of the modifications needed to be made on each programme are given. Both programmes take advantage of the proprties listed above and store only one half band. Since the arithmetical operations are confined to the terms within the half band, economy on the working storage and computer operations is made.

The first programme was originally developed at university college, Cardiff, and was used by the author in his M.Sc. studies[52]. Full description of the programme is given in reference 51. The programme consists of a main routine and two sub-routines. The purpose of the main routine is to read in the data for the problem under consideration, allocate the necessary spaces, set up the boundary conditions and the load vectors and calculate a number of control coefficients, which are incorporated to make the function of the sub-routines as general as possible. The function of the first sub-routine is to calculate the element stiffness matrix. The second, which assembles the overall stiffness matrix and solves the equations at the same time, constitutes the most important part of the programme. All the results presented in chapter 4 were obtained using this programme. As, in its published form, the programme can deal with imposed loads only, modifications

were made so that displacements as well as loads could be imposed at the structure under consideration. This was done using a method outlined in reference 4, and required a few statements to be incorporated in the main routine and in the second subroutine. Other modifications were made so that stiffness matrices for elements of differing sizes could be computed and assembled in any one run. Additional subroutines were also written for calculating stresses and 'exact' solutions. This programme was run on an ICL 1904 S / 128 K words system available at the South Glamorgan Institute of Higher Education.

The second programme, which originates from that given in reference 4, was developed by Coughlan[41]. The programme consists basically of three routines whose functions are broadly the same as those for the first programme. An added advantage in the use of this programmeis that, for any given problem, the finite element mesh can be subdivided into a number of partitions, thus making it capable of handling problems requiring a large number of elements. This programme, which uses CST elements, was modified so that elements I and II could be incorporated. Additional routines for automatic generation of the finite element meshes and for calculating stresses near the crack-tip were also written. All the results presented in this thesis, with the exception of those given in chapter 4, were obtained using this programme on a DEC 20/50/448 K words system housed at the Polytechnic of Wales.

Single precision calculations were performed throughout the work reported herein.

REFERENCES

1. Turner, M.L, Clough R.W., Martin, H.C. and Topp, L.J.
   Stiffness and deflection analysis of complex structures, Journal of Aeronautical Sci., 23, 1956, pp. 805 - 824 .

2. Zienkiewicz, O.C. and Cheung, Y.K.
   The finite element for analysis of elastic isotropic and orthotropic slabs, Proc. Inst. Civ. Engrs., 28,1964, pp. 471 - 488 .

3. Melosh, R.J.
   Journal Aeronautical Sci., vol. 28, No. 1, 1961, p.34 .

4. Zienkiewicz, O.C.
   The finite element method in engineering science, McGraw-hill, London, 1971.

5. Bogner, F.K., Fox, R.L. and Schmitt, L.A.
   A cylindrical shell discrete element, A.I.A.A. Journal, vol. 5, No. 4, April 1967, pp. 745 - 750 .

6. Cantin, G. and Clough, R.W.
   A curved cylindrical shell finite element, A.I.A.A. Journal, vol. 6, No. 6, June 1968, pp. 1057 - 1062 .

7. Ashwell, D.G., Sabir, A.B. and Roberts, T.M.
   Further studies in the application of curved finite elements to circular arches, Int. J. Mech. Sci., Pergamon Press, 1971, vol. 13, pp. 507 - 517 .

8. Irwin, G. R.

Fracture mechanics - structural mechanics, Pergamon Press, New York, N.Y., 1960, pp. 557 - 592 .

9. Paris, P.C. and Sih, G.C.

Stress analysis of cracks, A.S.T.M., S.T.P., 381, 30, 1965.

10. Timoshenko, S.P. and Goodier, J.N.

Theory of elasticity, third edition, 1970, McGraw-Hill, Kogakusha Ltd.

11. Kobayashi, A.S., Maiden, D.E., Simon, B.J. and Iida, S.

Application of finite element analysis method to two - dimensional problems in fracture mechanics, A.S.M.E. Winter annual meeting, 1969, 69-WA/PVP-12 .

12. Irwin, G.R.

Analysis of stresses and strains near the end of a crack traversing a plate, Transactions Am. Soc. Mech. Engrs., Journal of Applied Mechanics, 1957.

13. Chan, S.K., Tuba, I.S. and Wilson, W.K.

On the finite element method in linear fracture mechanics, 2nd National Fracture Mechanics Symposium, Lehigh University, 17 - 19 June 1968.

14. Watwood, V.L.

The finite element method for prediction of crack behaviour, Nuclear Eng. and Design, 1969, 11, pp. 323 - 332.

15. Dixon, J.R. and Strannigan, J.S.
Determination of energy release rates and stress intensity factors by the finite element method, Journal of strain analysis, vol. 7, No. 2, 1972.

16. Kendall, D.P. and Hussain, M.A.
A new fracture - toughness test method for thick-walled cylinder material, presented at 1971 S.E.S.A. Spring Meeting held in Salt Lake City, Utah on May 18 - 21, Experimental Mechanics, pp. 184 - 189, April 1972.

17. Byskov, E.
The calculation of stress intensity factors using the finite element method with cracked elements, Int. J. Fracture Mechanics, 6, pp. 159 - 167, 1970.

18. Muskhelishvili, N.
Some basic problems of the mathematical theory of elasticity, P. Noordhoff, Groningen, Neth., 1963.

19. Wilson, W.K.
Some crack tip finite elements for olane elasticity, Proceedings of the 1971 National Symposium on fracture Mechanics, Part 1, A.S.T.M., S.T.P. 513, American Soc. for Testing and Materials, 1972, pp. 90 - 105.

20. Williams, M.L.
On the stress distribution at the base of a stationary crack, J. of Applied Mechanics, vol. 24, No. 1, March 1957, pp. 109 - 114.

21. Tracey, D.M.
Finite elements for determination of crack-tip elastic stress intensity factors, Engrg. Fracture Mechanics, vol. 3, pp. 255 - 266, 1971.

22. Henshell, R.D. and Shaw, K.G.
Crack-tip elements are unnecessary, Int. J. for Num. Meth. in Engrg., vol. 9, pp. 495 - 509, 1975.

23. Barsoum, R.S.
On the use of isoparametric finite elements in linear fracture mechanics, Int. J. for Num. Meth. in Engrg., vol. 10, No. 1, pp. 25 - 37, 1976.

24. Barsoum, R.S.
A degenerate solid element for linear fracture analysis of plate bending and general shells, Int. J. for Num. Meth. in Engrg., vol. 10, No. 3, pp. 551 - 564, 1976.

25. Owen, D.R.J., Nayak, G.C., Kfouri, A.P. and Griffiths, J.R.
Stresses in a partly yielded notched bar - an assessment of three alternative programmes, Int. J. for Num. Meth. in Engrg., vol. 6, pp. 63 - 73, 1973.

26. Birch, J.M., Wilshire, B., Owen, D.J.R. and Shantaram, D.
The influence of stress distribution on the deformation and fracture behaviour of ceramic materials under compression creep conditions, J. of Material Science, 11, pp. 1817 - 1825, 1976.

27. Barsoum, R.S.

Triangular quarter point elements as elastic and perfectly plastic crack-tip elements, Int. J. for Num. Meth. in Engrg., vol. 11, No. 1, pp. 85 - 98, 1977.

28. Bleackley, M.H. and Luxmoore, A.R.

An investigation of numerical errors in finite element elastic-plastic crack extension models, 1st. Int. Symposium on numerical methods in fracture mechanics, Univ. coll. Swansea, 1978, edited by Owen, D.R.J. and Luxmoore, A.R.

29. Hibbitt, H.D.

Some properties of singular isoparametric elements, Int. J. for Num. Meth. in Engrg., vol.11, No. 1, pp. 180 - 184, 1977.

30. Gallagher, R.H.

A review of finite element techniques in fracture mechanics, 1st. Int. Symposium on numerical methods in fracture mechanics, Univ. Coll. Swansea, 1978, edited by Owen, D.R.J. and Luxmoore, A.R.

31. Lynn, P. and Ingraffea, A.R.

Transition elements to be used with quarter point crack-tip elements, Int. J. for Num. Meth. in Engrg. vol.11 .

32. Pian, T.H.H., Tong, P. and Luk, C.

Elastic crack analysis by a finite element hybrid method, Proc. 3rd. Air Force Conf. on Matrix Methods in Struct. Mech., Dayton, Ohio, 1971.

33. Murakami, Y.

A simple procedure for the accurate determination of stress intensity factors by finite element method, Engrg. Fracture Mech., vol. 8, No. 4, pp. 643 - 656, 1976.

34. Barr, B.I.G., Evans, W.T., Watkins, J. and Rouhi, M.R.

Fracture path prediction using numerical and experimental techniques, 1st. Int. Symposium on Numerical Methods in Fracture Mechanics, Univ. Coll. Swansea, 1978, edited by Owen, D.R.J. and Luxmoore, A.R.

35. Grifith, A.A.

The phenomena of rupture and flow in solids, Transactions, Royal Soc., London, vol. 221, 1920.

36. Rice, J.R.

A path-independent integral and the approximate analysis of strain concentration by notches and cracks, Transactions, A.S.M.E., Journal of Applied Mechanics, vol. 35, pp. 379 - 386, 1968.

37. Mowbray, D.F.

A note on the finite element method in linear fracture mechanics, Engrg. Fracture Mech., vol. 2, pp. 173 - 176, 1970.

38. Owen, D.R.J. and Griffiths, J.R.

Stress intensity factors for cracks in a plate containing a hole and in a spinning disc, Int. J. of Fracture, vol. 9, No. 4, Dec. 1973.

39. Parks, D.M.

A stiffness derivative finite element technique for determination of elastic crack-tip stress intensity factors, Int. J. Fracture, vol. 10, No. 4, pp. 487 - 502, 1974.

40. Hellen, T.K.
On the method of virtual crack extensions, Int. J. for Num. Meth. in Engrg., vol. 9, No. 1, pp. 187 - 208, 1975.

41. Coughlan, J.
Crack propogation in isotropic materials, Ph.D. thesis, C.N.A.A., London, 1973.

42. Brown, W.F. and Srawley, J.E.
Plain strain crack toughness testing of high strength metallic materials, A.S.T.M. Special Technical Publication, No. 410, 1966.

43. Gross, B., Srawley, J.E. and Brown, W.F.
Stress intensity factors for a single-edge-notch tension specimen by boundary collocation of a stress function, Technical Note D-2395, August 1964.

44. Bear, T.J. and Barr, B.I.G.
International Journal of fracture, 13, pp. 92 - 96, 1977.

45. Barr, B. I. G. and Bear, T.J.
The use of the split-cube test to evaluate the fracture toughness of concrete, Report, Department of Civil Engineering and Building, The Polytechnic of Wales, February 1978.

46. Neuber, H.
Theory of notch stresses : Principles for exact calculation of strength with reference to structural form and material, U.S. Atomic Energy Commission, Office of Technical Information, 1958.

47. Bear, T.J.

New fracture toughness tests for rock and concrete with particular reference to rock structure design, Ph.D. thesis submitted to C.N.A.A., London, August 1976.

48. Erdogan, F. and Sih, G.C.

On the crack extension in plates under plane loading and transverse shear, Transactions of the A.S.M.E., Journal of Basic Engineering, 85, pp. 519 - 527, 1963.

49. Rouhi, M.R.

The application of photoelasticity to plain strain fracture problems, M.Phil. thesis submitted to the C.N.A.A., London, 1977.

50. Chisholm, D.B. and Jones, D.L.

An analytical and experimental stress analysis of a practical mode II fracture test specimen, Experimental Mechanics, pp. 7 - 13, Jan. 1977.

51. Sabir, A.B.

The nodal solution routine for the large number of linear simultaneous equations in the finite element analysis of plates and shells, in Finite Elements for Thin Shells and Curved Members, edited by Ashwell, D.G. and Gallagher, R.H., published by Wiley, 1976.

52. Sabir, B.B.

The behaviour of light gauge steel hypars, M.Sc. thesis submitted to the university of Wales, October, 1971.